Halvor R. Fergestad

Optimization Of Photonic Crystal Ring Resonators For Label-Free Biosensing Purposes

Master's thesis

NTNU
**Norwegian University of
Science and Technology**

Problem Description

Integrated photonics involves the design and fabrication of on-chip optical components. Optical components can be dielectric waveguides, couplers, resonators, and modulators

This Master's thesis concerns slab photonic crystals with two-dimensional periodicity as a sensing device for biomedical sensing. The photonic crystal sensing devices are in this work configured as ring resonators. The thesis work involves both simulation and fabrication work.

Photonic crystal ring resonator (PCRR) design is optimized in simulation software such as MIT Photonic Bands (MPB) and MIT electromagnetic equation propagation (Meep). MPB is a frequency domain solver (FDS) software, and Meep is a finite-difference time-domain (FDTD) software. Comprehensive and time demanding simulations are performed on Fram. Fram is a shared resource for scientific computing, hosted by the University in Tromsø. The purpose of simulating the devices is to better understand and optimize key figures of merit, and investigate the possibility of using PCRR for label-free biosensing.

Fabrication and characterization of PCRRs is performed at NTNU NanoLab. They are produced in silicon that has a silicon-on-insulator configuration. Instruments such as plasma enhanced chemical vapor deposition (PECVD), electron beam lithography (EBL), inductively coupled plasma-reactive ion etching (ICP-RIE), scanning electron microscope (SEM) are used in fabrication and characterization. Transmission measurements are performed with a tunable laser. The transmission measurements take place in a laser lab at the ELEKTRO-building at NTNU. The purpose with the experimental part of the thesis is to optimize fabrication processes intended for photonic crystal ring resonators, and to validate simulation results.

Abstract

Photonic crystals (PC) are materials with sub-wavelength permittivity variations. They exhibit interesting optical properties in terms of dispersion characteristics and light confinement. Their optical properties are interesting for photonic integrated circuits.

This thesis work investigates photonic crystal ring resonators (PCRR) in triangular air-hole PC slab for label-free biosensing. The thesis work contains simulations, fabrication, and characterization of PCRRs.

Simulation is performed in software such as MIT Photonic Bands (MPB) for frequency domain solved (FDS) dispersion relations, and MIT electromagnetic equation propagation (Meep) for transmission and mode simulations. PCRR configuration is optimized to produce high quality-factor (Q-factor) mode simulated PCRRs.

Optical devices such as strip waveguides and line defects in PC support light coupling to PCRRs. Strip waveguides and line defects are therefor simulated as stand alone structures. triangular air-hole PC, strip waveguide, and line defect are simulated with MPB in both two and three dimensions. Guided modes in strip waveguide and line defect are found to match the band-gap of triangular air-hole PC. Transmission simulations are performed in two and three dimensions. Three dimensional simulations are run on Fram, a super computer. Two-dimensional transmission spectra exhibit sharp resonances in the band-gap. The resonances are fewer and less sharp for three-dimensional simulations. Mode simulations coincides with transmission simulations. Highest achieved Q-factor for two-dimensional simulations is 5.7×10^8. For three-dimensional simulations the highest achieved Q-factor is 59871.

Fabrication of PC structures is performed using plasma enhanced chemical vapor deposition (PECVD) for thin film growth, electron beam lithography (EBL) and mask less aligner (MLA) for exposure, and inductively coupled plasma-reactive ion etching (ICP-RIE) for etching. Both crystalline-Silicon (c-Si) and amorphous-Silicon (a-Si) devices are fabricated. a-Si devices are fabricated with light coupling variations in form of inverted tapers.

Characterization of fabricated devices is performed by tunable laser measurements in a drop-filter transmission configuration. c-Si devices exhibited better transmission performance than a-Si devices. The highest measured Q-factor value for fabricated devices was 25739.

Preface

This thesis is submitted in partial fulfillment of the requirements for the degree of Master of Science in Electronics at the Department of Electronics (IE) at the Norwegian University of Science and Technology (NTNU).

The Master's thesis is a continuation of a specialization report from Fall of 2018 [14]. The specialization report includes simulation work on photonic crystal ring resonators (PCRR). The theory chapter in this thesis builds on the work done in the specialization report. The experimental procedure is influenced by previous work at IE [27][26][25]. The fabrication recipes explained in the experimental procedure belong to Jens Høvik and parts of Figure 1.1 are generously provided by Nina Arnfinnsdottir, Jon Olav Grepstad, and Ingrid Øvreeide.

Acknowledgements

Numerous people deserve acknowledgement for helping me through my thesis work.

I thank my supervisor, Prof. Astrid Aksnes who has always been available for logistical and scientific help. Without her determination Fram would most likely not been at my disposal.

My co-supervisor Mukesh Yadav has patiently helped me with fabrication issues, transmission testing, and offered advise regarding thesis content. Mukesh Yadav's help was instrumental in fabricating inverted tapers.

I thank Jens Høvik for helping me with simulation challenges, generously offering fabrication recipes, and licensing me for the fabrication instruments. He also enlightened me in times of development and transmission measurement challenges.

My Father, Dag Fergestad deserves acknowledgement for the boring but much needed work of proof reading my thesis. The Research Council of Norway is acknowledged for the support to the Norwegian Micro- and Nano-Fabrication Facility, NorFab.

Table of Contents

List of Tables

List of Figures

Abbreviations

a-Si	=	amorphous-Silicon
BSE	=	Back Scattered Electron
c-Si	=	crystalline-Silicon
CCD	=	Charge Coupled Device
CMOS	=	Complementary Metal-Oxide-Semiconductor
CVD	=	Chemical Vapor Deposition
DFT	=	Discrete Fourier Transform
EBL	=	Electron Beam Lithography
ERI	=	Effective Refractive Index
FA	=	Fourier Analysis
FDS	=	Frequency-Domain Solver
FDTD	=	Finite Difference Time Domain
FT	=	Fourier Transform
FWHM	=	Full Width Half Maximum
GDS	=	Graphic Database System
IBZ	=	Irreducible Brillouin Zone
IC	=	Integrated Circuit
ICP-RIE	=	Inductively Coupled Plasma-Reactive Ion Etching
IPA	=	Isopropanol
LF	=	Low Frequency
LOC	=	Lab-On-a-Chip
LOD	=	Limit Of Detection
LPCVD	=	Low Pressure Chemical Vapor Deposition
ME	=	Maxwell's Equations
Meep	=	MIT electromagnetic equation propagation
MLA	=	Mask Less Aligner
MPB	=	MIT Photonic Bands
PC	=	Photonic Crystal
PCRR	=	Photonic Crystal Ring Resonator
PECVD	=	Plasma Enhanced Chemical Vapor Deposition
PR	=	Photoresist
Q-factor	=	Quality-factor
RF	=	Radio Frequency
SE	=	Secondary Electron
SEM	=	Scanning Electron Microscope
SOI	=	Silicon On Insulator
TE	=	Transverse Electric
TIR	=	Total Internal Reflection
TM	=	Transverse Magnetic

1.   Introduction

This thesis concerns optimization of photonic crystal ring resonators as a sensing device for biomedical purposes. The ring resonators are simulated and fabricated by state of the art simulation tools and instruments, respectively. The thesis work is supervised by Prof. Astrid Aksnes and is part of the interdisciplinary project Lab-On-a-Chip (LOC). The introduction consists of five sections.

1. Project description for Lab-On-a-Chip (LOC).

2. Introduction to photonic crystals (PC).

3. Thesis focus.

4. Fabrication and characterization.

5. Structure of thesis.

Sections one and three are included as an effort to express the thesis' relevance and relation to its host project, LOC. Sections two and four are introduction to PC, simulations, and fabrications and are intended to motivate the theory presented in Chapters 2 and 3. The last section summarizes the structure of the thesis.

1.1 Lab-On-a-Chip

Lab-On-a-Chip (LOC) is an interdisciplinary project involving experts in biofunctionalization, microfluidics, and photonics. Project participants come from NTNU, St. Olavs University Hospital, and SINTEF. The project started in 2014 and is run under the "National Centre for Digital Life" initiative. The goal of the project is to develop a generic label-free biophotonic sensor platform capable of performing highly sensitive and selective multiplexed quantitative diagnostic tests.
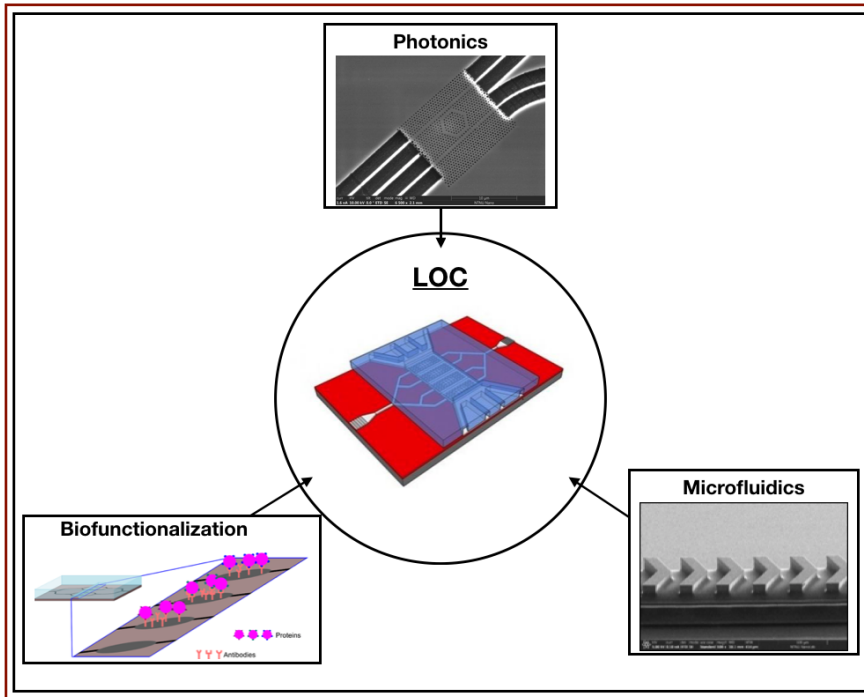
Figure 1.1: Illustration of a proposed Lab-On-a-Chip inside the circle. Boxes outside the circle illustrates the disciplines participating in the project. Project members with a photonics background create the sensing surface and guiding of light. Members with a microfluidics background functionalize the channels leading the sample to the sensor surface. Members with a biofunctionalization background create the biolayer that the sensor is coated with to absorb the desired biomarkers. Biofunctionalization, LOC, and microfluidics figures courtesy of Nina Arnfinnsdottir, Jon Olav Grepstad, and Ingrid Øvreeide, respectively.

The sensor surface can be modified to detect different biomarkers and can also detect different biomarkers simultaneously at various locations on the chip, known as multiplexing. By utilizing PC as sensing elements the limit of detection (LOD) can be targeted to a range as low as ng/ml - pg/ml. The low LOD is due to the intrinsic properties of PC. A low LOD allows for earlier detection and/or smaller sample volumes. Early and reliable detection of diseases is desirable to increase the chance of a successful treatment that po-

tentially can be less invasive, less time-consuming, and more cost efficient. Samples that the LOC is intended to analyze are blood, saliva, and urine. The sample is guided to the PC through microfluidic channels. At the PC sites the sample interacts with a biolayer which the PC is coated with. Specific contents in the sample referred to as biomarkers binds to the biolayer. The biomarker interacts with an evanescent electromagnetic field originating from a light source. A light source must be located externally due to material limitations. The post biomarker-interacted evanescent field is detected by an externally located light detector. The sensor itself is built on the silicon-on-insulator (SOI) platform. SOI is a material stack consisting of a silicon wafer, a thin-film layer of silica (SiO_2), and a thin-film layer of silicon, listed from the bottom and upwards. The layer of silica acts as an insulator for the top layer of silicon, thus the name SOI. SOI is utilized because of its compatibility to CMOS fabrication processes. The external source is a tunable diode laser with a center wavelength of 1.55 μm and tunable wavelength range from 1480-1640 nm. Many interesting biomarkers have distinct characterizations in the infra-red regime. Silicon also exhibits transparency in the infra-red regime. Inexpensive lasers and fibers have been produced for 1.55 μm wavelengths since 1.55 μm wavelengths is extensively used for telecommunication purposes. PCs would be extremely small and unfeasible to fabricate with today's fabrication technology for visible wavelength ranges.

1.2 Introduction To Photonic Crystals

Photonic crystals are structures with spatially-dependent permittivity. The spatial dependence is on the order of a wavelength, and is carefully engineered to fulfill given design requirements. PCs offer excellent light confinement. A high degree of light confinement allows light to be slowed down, guided through sharp bends [38], trapped or delayed at desired locations. High light confinement at a desired location implies that the light is interacting considerably with the material in question at the given location. A high degree of interaction is detectable when investigating an output spectra. High light confinement substantiates extremely narrow spectral resonances, which is vital for achieving low LOD.

PCs were introduced in 1987 with the paper "Inhibited Spontaneous Emission in Solid-State Physics and Electronics" by E. Yablonovitch [68]. The paper introduced the scientific community to structures with a forbidden frequency band-gap. The immediate proposed application was to align the forbidden band-gap with the electronic band edge of various devices to deny spontaneous emission [68]. In later years, structures like the Yablonovite, the woodpile crystal, and spheres in a diamond lattice have been fabricated and proven to exhibit a complete photonic band-gap [58][45][47]. Figure 1.2 illustrates the three-dimensional structures Yablonovite, the woodpile crystal, and spheres in a diamond lattice.
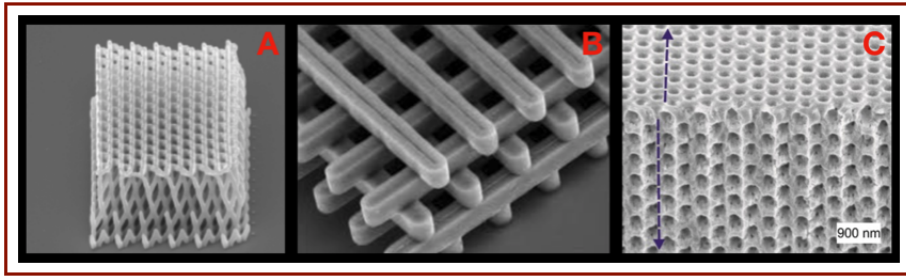
Figure 1.2: Pictures of an inverse Yablonovite (A), woodpile structure (B), and inverse spheres in a diamond lattice structure (C) all taken with a scanning electron microscope (reprinted from [59]).

The fabrication of three-dimensional photonic structures is generally more difficult than for two-dimensional photonic structures. Photonic crystals are, as mentioned above permittivity differences on the order of a wavelength. When considering the infra-red bandwidth centered around 1550 nm the fabrication methods need to offer excellent resolution far beyond one micron resolution. Therefore, well developed complementary metal-oxide-semiconductor (CMOS) fabrication processes are attractive to use when fabricating photonic crystals. CMOS processes are generally two-dimensional processes constraining the photonic crystals involved in LOC to two-dimensional photonic crystals. Two-dimensional photonic crystals rely on total internal reflection (TIR) along the third axis [55][31]. Physically, photonic crystals experience a periodically reinforced TIR. TIR at a single interface does not confine light nearly as well as a photonic crystal. The third spatial dimension when considering two-dimensional photonic crystals is often a great source of loss. Photonic crystal loss is covered in Chapter 2. Besides being a well developed research field photonic crystals have been commercialized in fiber applications and LED (light emitting diode) applications [66][67][50].

1.3 Thesis Focus

This thesis investigates photonic crystal ring resonators (PCRR) as a sensing device for LOC applications. The intention is to optimize PCRR. Ring resonators can be used as delay structures, filters, and pump medium for light [70][56][10]. In this thesis PCRR will be optimized with respect to measuring the concentration of a biomarker by measuring the shift in resonance frequency. The idea is that an evanescent field originating from an external light source is guided to the PCRR by a waveguide. The PCRR is coated with a biolayer. A second waveguide exiting the PCRR is connected to the external detector. The output frequency shifts depending on the presence of biomarkers. Presence of any biomarker changes the effective refractive index (see Chapter 2), causing the resonance frequency to shift. The thesis does not involve any PCRR and biolayer interaction. Instead, geometric configuration of photonic crystal holes are optimized to produce a clear as possible resonance frequency. PCRRs in this thesis are investigated and evaluated separately from any other aspect of the LOC project.
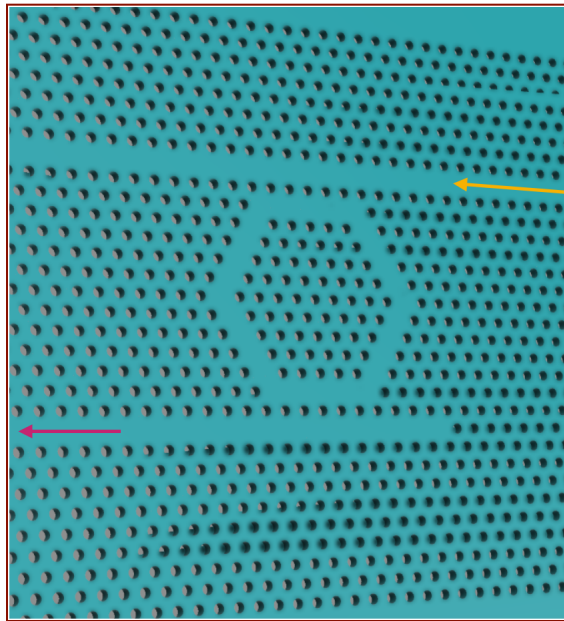
Figure 1.3: Three-dimensional illustration of the top silicon layer of a PCRR. Input and output waveguides are marked with a yellow and pink arrows, respectively.

Figure 1.3 is a three-dimensional illustration of the top silicon layer of a PCRR with input and output waveguide marked with a yellow and pink arrow, respectively. A PCRR can be optimized in several different ways. Below is a list of optimization parameters, all considered to be geometrical optimization parameters:

1. The distance from the ring resonator to waveguide.

2. Shifting the periodicity length (lattice constant) in certain areas.

3. The air-hole radius (not specific to PCRR).

4. Geometric configurations at ring resonator corners.

5. Geometric configurations of ring resonator line defects.

6. Ring resonator radius.

7. Thickness of the photonic crystal layer (not specific to PCRR).

Different ways of optimizing a PCRR geometrically are illustrated in Figure 1.4.
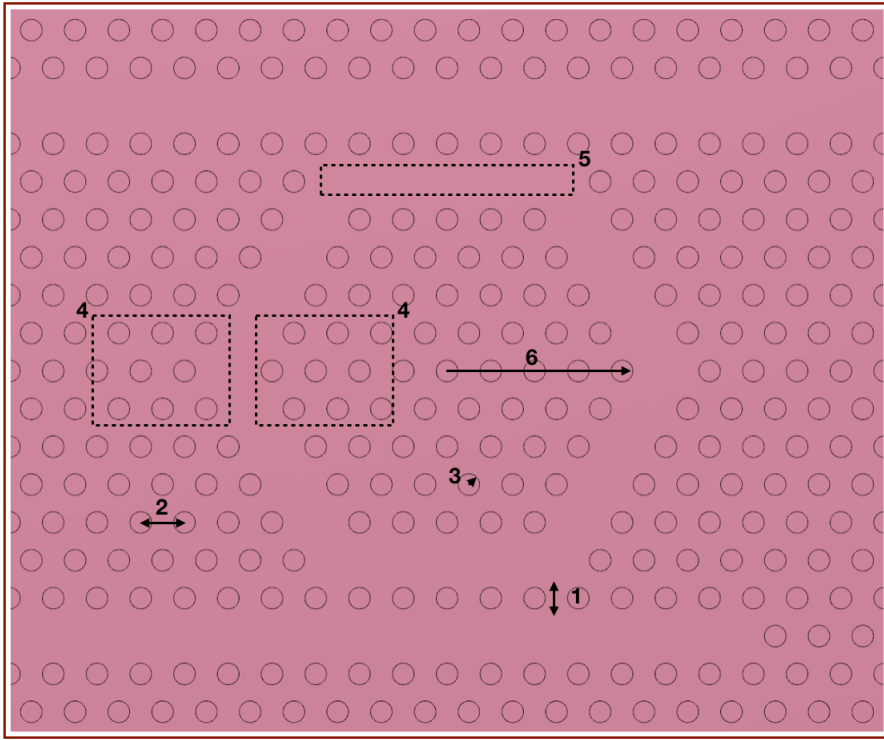
Figure 1.4: Overview of areas of interest for optimization. **1** refers to the separation distance between ring-resonator and waveguide. **2** refers to the lattice constant. **3** refers to the air-hole radius. **4** refers to the ring resonator corners. **5** refers to the ring resonator line defects. **6** refers to the ring resonator radius.

The different ways of optimizing a PCRR listed above, except for thickness of photonic crystal layer, are illustrated in Figure 1.4. The distance from ring resonator to waveguide is usually given in number of air-hole rows. Geometric configuration of ring resonator line defects can come in various shapes and forms. Smaller holes can be introduced to the ring resonator line defects, or the ring resonator line defects may be given more space in certain areas by shifting the holes closest to the ring resonator.

The boundary area between the photonic crystal (PC) and the slab waveguide can be optimized geometrically. There are also ways of optimizing PCRR from a material perspective. Both crystalline silicon (c-Si) and amorphous silicon (a-Si) can be utilized for the top silicon layer. a-Si and c-Si have different dB/m merits which affect the PCRR performance. a-Si is cheaper while c-Si allows for under-etching, another geometrical optimization choice. Using an external source and detector introduces insertion loss to and from the device, respectively. Input coupling of light is therefor an optimization issue in it of itself.

In this thesis the geometrical configurations; geometric configurations at ring resonator corners, and geometric configurations of ring resonator line defects will be investigated for optimization purposes. The geometrical configurations will be tested for both a-Si and c-Si

devices. Input coupling of light is also addressed.

1.4   Simulation, Fabrication, and Characterization

Simulations are done in MIT Photonic Bands (MPB) and MIT electromagnetic equation propagation (Meep). MPB is used to produce band diagrams for the photonic crystals. Band diagrams are graphical representations of frequency as a function of wave vector k. Band diagrams for intrinsic photonic crystals and photonic crystals with defects are produced with MPB.

Meep is a finite difference time domain (FDTD) software. FDTD is a way of solving a set of problems, in this case equations. Meep solves Maxwell's equations (ME) in time domain for a user defined computational cell. Meep is an effective software when solving an electromagnetic field interacting with a user defined structure due to its FDTD algorithm. Meep simulations can be quite time and resource consuming depending on variables such as dimensions, resolution, source bandwidth, and computational cell size. Most three-dimensional simulations are therefore run on Fram. Fram is a shared super computer for research computing hosted by the university in Tromsø.

The fabrication steps to produce photonic crystals are developed through CMOS-technology. One of the advantages of using silicon as material is the well developed fabrication methods that exist. Silicon wafers come predeposited with either silicon dioxide (SiO2, silica) or silica and crystalline-Silicon (c-Si). The wafers are cut into reasonable sized dies and undergo treatments such as Plasma Enhanced Chemical Vapor Deposition (PECVD), Electron Beam Lithography (EBL), and Inductively Coupled Plasma-Reactive Ion Etch (ICP-RIE) to acquire the end results. All of these fabrication steps are available through NTNU NanoLab. Characterization is done both at NTNU NanoLab and in a laser-lab setup by Prof. Astrid Aksnes group. NTNU NanoLab facilitates a SEM, offering satisfactory images for PC resolution requirements. Transmission measurements are performed in the laser-lab. A diode laser with center frequency of 1550 nm is coupled to the fabricated photonic crystal sensor. An output fiber is attached to a detector which permits recording of transmission spectras.

1.5   Structure Of Thesis

The required theory to understand photonic crystal physics, its limitations, and the design decisions that are made is presented in Chapter 2. The majority of Chapter 2 is reproduced from the specialization report and is included for completeness [14]. Chapter 3 is intended as an introduction to understand the simulation tools and fabrication instruments that have been applied. Both the mathematical models which the simulation tools are built on and the physics behind the fabrication instruments are fields of extensive research, and to some extent still not fully understood. Chapter 3 only covers what the author finds sufficient for understanding the tools and software, their limitations, and their usage to fabricate PCRRs. Chapter 4 is devoted to the experimental procedure, explaining everything from how the simulations are set up to how the fabrication is performed. After reading Chapter 4 the reader should be provided a framework to reproduce the accomplished results, or at

least that is the intention. Results are presented in Chapter 5, where the presentation is structured into sections; simulation, fabrication and characterization. A conclusion of the thesis is given in Chapter 6.

2.   Theory

The purpose of this chapter is to give a thorough explanation of the required theory needed to understand photonic crystals and the design decisions that are made. The prior knowledge expected to understand the following theory is: introductory electromagnetism, frequency analysis, calculus, and linear algebra. Especially recommended sources for broad photonics understanding are "Photonics" by Yariv and Yeh [69] and "Fundamentals of Photonics" by Saleh and Teich [55]. For more specific photonic crystal knowledge recommendation is made to "Photonic Crystals: Molding the Flow of Light" by John D. Joannopoulos et al. [31]. For in-depth explanations of symmetry theory R. Newnham's "Properties of Material" is recommended [49]. The theory chapter is divided into the following subsections:

1. Maxwell's Equations.

2. Material Considerations.

3. One-Dimensional Photonic Crystal And Matrix Formalism.

4. Energy Confinement In Photonic Crystals.

5. Effective Refractive Index And Coupling.

6. Symmetry Theory.

7. Defects In Photonic Crystals.

8. Frequency Analysis and the Fourier Transform.

9. Q-Factor.

10. Loss.

Some of the subsections feed in to each other. The subsections should therefore be read in the order they have been written.

2.1 Maxwell's Equations

Andre-Marie Ampere discovered Ampere's law in 1823 stating that there is an attraction or repulsion between two current-carrying wires [21]. In 1831 Michael Faraday discovered the underlying principles of electromagnetic induction, and established the concept of electromagnetic waves [23]. John Maxwell summarized these principles, together with Gauss' law, in what is known as Maxwell's equations (ME) in 1864 [44]. ME are stated below 2.1-2.4. They are the most important building stones for PC and describe light-matter interaction exquisitely.

$$\nabla \times \mathbf{D} = \rho \tag{2.1}$$

$$\nabla \cdot \mathbf{B} = 0 \tag{2.2}$$

$$\nabla \times \mathbf{E} = -\frac{\partial \mathbf{B}}{\partial t} \tag{2.3}$$

$$\nabla \times \mathbf{H} = \mathbf{J} + \frac{\partial \mathbf{D}}{\partial t} \tag{2.4}$$

With these equations John Maxwell was able to predict the speed of light and show that light is, in fact, electromagnetic waves [44]. To understand photonic crystals, a thorough understanding of ME is required. If possible, it is convenient to reduce the number of different parameters. $\mathbf{D}$ and $\mathbf{B}$ are considered electric- and magnetic flux densities, respectively [11]. $\mathbf{E}$ and $\mathbf{H}$ are considered electric- and magnetic field intensities [11]. ρ is charge density and $\mathbf{J}$ is current density. Fortunately there are some relating factors between the fields and fluxes. The relating factors are expressed in Equations 2.5 and 2.6.

$$\mathbf{D} = \epsilon_0 \mathbf{E} + \mathbf{P} \tag{2.5}$$

$$\mathbf{H} = \frac{\mathbf{B}}{\mu_0} - \mathbf{M} \tag{2.6}$$

The new quantities, $\mathbf{P}$ and $\mathbf{M}$, in Equations 2.5 and 2.6 are the overall polarization and magnetization of the material that the fields and fluxes are acting on, respectively. ϵ_0 and μ_0 are the vacuum permittivity and permeability, respectively. Equations 2.5 and 2.6 do not offer any simplification without applying material knowledge.

2.2 Material Considerations

In the following theory only the electrical properties will be explored. The magnetic equivalents generally have a similar reasoning, and the reader is referred to [8][69][55] for detailed explanation.

The electric flux $\mathbf{D}$, in equation 2.5, is the sum of contributions from an external electric field, $\mathbf{E}$, and the macroscopic polarization, $\mathbf{P}$, of an arbitrary material. The external applied field can be related to the polarization through the materials susceptibility.

$$\mathbf{P} = \epsilon_0 \chi \mathbf{E} \qquad (2.7)$$

χ, in Equation 2.7, is the electrical susceptibility. χ is a dimensionless property that describes how the polarization of a material behaves when under an applied external field [8]. The complexity of the relation between an applied electric field and the polarization of the material depends on the applied electric field and the material in question. How high is the intensity of the applied field? How complicated is the material? How precisely is the material described? In general the relation can be written as a Taylor expansion [8]:

$$P_i = \epsilon_0 (\chi_{ij} E_j + \chi_{ijk} E_j E_k + \chi_{ijkl} E_j E_k E_l + .. + \chi_{ij..n} E_j .. E_n) \qquad (2.8)$$

Equation 2.8 is written in tensor form [49]. The subscripts, *i, j, k, l,* and *n* denotes dimensions of the system described by Equation 2.8. Each subscript has a magnitude of three since they are representing fields propagating in real space; $i = 1, 2, 3,$. As an example, $\chi_{ijk} E_j E_k$ describes two fields interacting in a medium. The medium they are interacting in is described by χ_{ijk}, which is a 3×3×3 matrix. The general trend of Equation 2.8 is a decreasing χ for increasing order of nonlinearity [49][8]. Nonlinearity is in this case the number of terms in the Taylor expansion. The second term on the right hand side of Equation 2.8, $\chi_{ijk} E_j E_k$, represents first order nonlinearity and is referred to as second order processes. To counteract the decreasing trend of χ the applied field must be increasingly intense. This trade-off is basically the linearity of the system. Silicon exhibits large third order linearity (i.e. large χ_{ijkl} coefficients) [8][4][35]. The sources used in the LOC-project are not strong enough to excite the third order linearity in silicon too any considerable degree. The PCRRs are therefor modelled to behave in the linear regime, reducing Equation 2.8 to Equation 2.9[8].

$$P_i = \epsilon_0 \chi_{ij} E_j \qquad (2.9)$$

Subsequently Equation 2.5 is reduced to Equation 2.10.

$$\mathbf{D} = \epsilon_0 (\mathbf{E} + \chi \mathbf{E}) \qquad (2.10)$$

By applying the relation between the linear susceptibility, χ, and the relative permittivity ϵ_r as stated in Equation 2.11, one obtains a simple relation between the electric flux **D** and the applied electric field **E**. The relation is given in Equation 2.12.

$$\chi = \epsilon_r - 1 \qquad (2.11)$$

$$\mathbf{D} = \epsilon_0 \epsilon_r \mathbf{E} \qquad (2.12)$$

The same simple relation between the magnetic flux **B** and the magnetic field **H** is, without explanation given in Equation 2.13.

$$\mathbf{B} = \mu_0 \mu_r \mathbf{H} \qquad (2.13)$$

It is worth mentioning that the reason for the simple relation in Equation 2.13 is based on the assumption of paramagnetic and diamagnetic material [49]. The relations of Equation 2.12 and 2.13 are known as constitutive relations [11].

The only assumption so far is the assumption of a linear medium, or a linear regime.

The intention with the photonic devices is to initiate a displacement field within the structure that is confined by chosen design parameters. Further, the assumption of no charge- or current sources within the photonic device (PD) is made. This implies that ionization of atoms constituting the PD is inhibited or neglected. By Coulomb attraction/repulsion of electrons and protons, ionization requires higher intensity than what is required to access the nonlinear regime. The source and medium are already assumed to be linear. The intrinsic PD can therefore not embody charge- or current sources. The only origin left for charge- or current sources are defects. Defects are assumed to contribute with a negligible amount. The assumptions made so far manifests themselves in ME in the following way.

$$\nabla \times \mathbf{E} = 0 \tag{2.14}$$

$$\nabla \cdot \mathbf{H} = 0 \tag{2.15}$$

$$\nabla \times \mathbf{E} = -\mu \frac{\partial \mathbf{H}}{\partial t} \tag{2.16}$$

$$\nabla \times \mathbf{H} = \epsilon \frac{\partial \mathbf{E}}{\partial t} \tag{2.17}$$

In Equations 2.16 and 2.17, $\epsilon = \epsilon_0 \epsilon_r$ and $\mu = \mu_0 \mu_r$. Any terms in Equation 2.14-2.17 representing charges or current densities are removed due to our assumption above.

The next step in understanding photonic crystals is convincing the reader that electromagnetism manifests itself in waves. In the process of deducing the wave equation further material assumptions must be made. Mathematical curl operations are needed to deduce the differential wave equation [3].

$$\nabla \times (\nabla \times \mathbf{A}) = \nabla(\nabla \cdot \mathbf{A}) - \nabla^2 \mathbf{A} \tag{2.18}$$

Applying Equation 2.18 to Equation 2.16 and 2.17, starting with Maxwell-Ampère's Equation (2.17) results in a differential equation for the $\mathbf{H}$-field. The derivation for the differential equation for the $\mathbf{H}$-field follows. Derivation for $\mathbf{E}$-field is similar, only starting with Equation 2.16 instead of Equation 2.17, and offers no further insight.

$$\nabla \times \nabla \times \mathbf{H} = \epsilon \frac{\partial(\nabla \times \mathbf{E})}{\partial t} \tag{2.19}$$

$$\nabla^2 \mathbf{H} = \mu \epsilon \frac{\partial^2 \mathbf{H}}{\partial t^2} \tag{2.20}$$

Some explanation is required to understand the evolution on the left hand side from Equation 2.19 to Equation 2.20. The left hand side of Equation 2.19 has been substituted by the right hand side of Equation 2.18. The term representing the gradient of a divergence, $\nabla(\nabla \cdot \mathbf{A})$, is set to zero. For this term to be nonzero there would have to be a magnetic monopole within the regarded system [22]. Magnetic monopoles have for a long time been empirical non-existing. In 2009 a magnetic monopole was observed

within condensed matter physics [13]. Magnetic monopoles have not been observed in silicon nor in air. Therefore no monopoles are assumed and justified in Equation 2.20. The right hand side evolution from Equation 2.19 and Equation 2.20 is just a substitution of Maxwell-Ampere's Equation 2.17 into the right hand side of Equation 2.19. A second order differential equation that relates the spatial and temporal derivatives of a variable is known as a wave Equation [29]. The general solution to Equation 2.20, solved in one dimension, is of the form.

$$\mathbf{H}(\mathbf{r}, t) = f(t - \mathbf{r}\sqrt{\mu\epsilon}) + f(t + \mathbf{r}\sqrt{\mu\epsilon}) \tag{2.21}$$

The two terms in Equation 2.21 indicate two entities travelling in opposite direction under time evolution. Equation 2.20 can also be solved under time-harmonic assumptions since ME of the form 2.14-2.17 are linear [11]. The time-harmonic solution is given in Equation 2.22. The solution is separated in time and space. When evaluating the physical field only the real value of the complex solution is valid.

$$\mathbf{H}(\mathbf{r}, t) = \mathbf{H}(\mathbf{r})e^{-i\omega t} \tag{2.22}$$

The solution separates the spatial and temporal components. The wave equation would be as in Equation 2.23 if the assumption of time-harmonic solution had been made before deducing the wave equation.

$$\nabla \times (\frac{1}{\epsilon}\nabla \times \mathbf{H}) = (\frac{\omega}{c})^2\mathbf{H} \tag{2.23}$$

Equation 2.23 is closely related to what is referred to as the **master equation** in "Photonic Crystals: Molding the Flow of Light" [31]. Equation 2.23 is presented in frequency form. The frequency representation is fundamental for simulation software presented in Chapter 3 as frequency domain solvers (FDS). The time domain representation seen in Equation 2.19 is on the other hand similarly important for simulation software based on finite difference time domain (FDTD) algorithms, also extensively covered in Chapter 3. The master equation is vital in establishing the dispersion relation for various photonic crystal structures. The dispersion relation is explained in Section 2.6 and produced in Subsection 5.2.1 as band diagrams.

So far linearity, charge- and current source free, magnetic monopole free assumptions have been made. Further restraints on the working domain would further simplify important relations.

$$D_i = \epsilon_{ij}E_j \tag{2.24}$$

Equation 2.24 is the tensor formalism of the relation between the electric flux and the electric field in Equation 2.12. The tensor formalism reveals the dimensionality of the permittivity tensor. Equivalently, the same relation can be described in matrix formalism as in Equation 2.25.

$$\begin{bmatrix} D_x \\ D_y \\ D_z \end{bmatrix} = \begin{bmatrix} \epsilon_{11} & \epsilon_{12} & \epsilon_{13} \\ \epsilon_{21} & \epsilon_{22} & \epsilon_{23} \\ \epsilon_{31} & \epsilon_{32} & \epsilon_{33} \end{bmatrix} \begin{bmatrix} E_x \\ E_y \\ E_z \end{bmatrix} \tag{2.25}$$

Sub-notations x, y, and z in Equation 2.25 denote an orthogonal coordinate-system representing a spatial domain. Thus the spatial dependence of the permittivity becomes apparent. We can generalize the permittivity matrix in the following way.

$$\begin{bmatrix} a & f & e \\ f & b & d \\ e & d & c \end{bmatrix} \tag{2.26}$$

Entries a, b, and c represent the permittivity along the orthogonal set of axes a, b, and c. If they are equal, meaning $a = b = c$, the material is isotropic [49]. Entries d, e, and f are off-diagonal entries and represent losses in the material or dispersion. Amorphous Silicon is by symmetry operations isotropic in nature [49]. The amorphous silicon is further assumed to be lossless and dispersionless. This is a nonphysical assumption implying that an external electric field instantaneously sets up a displacement field within the photonic device, violating Kramers-Kronig relation [55]. The assumption simplifies to a justifiable extent considering the results obtained.

$$\begin{bmatrix} \epsilon_{Si} & 0 & 0 \\ 0 & \epsilon_{Si} & 0 \\ 0 & 0 & \epsilon_{Si} \end{bmatrix} \tag{2.27}$$

Matrix 2.27 can be presented as in Equation 2.28.

$$\epsilon_{Si}\mathbf{I} \tag{2.28}$$

In Equation 2.28 $\mathbf{I}$ is the identity matrix. Equation 2.28 illustrates well how the permittivity is independent of direction, or stated differently the material is isotropic.
The material constraints are established and how they physically manifest themselves is explained. Constraints made to the material is the requirement of a linear, isotropic, source-free, lossless and dispersionless material.

2.3 One-Dimensional Photonic Crystal and Matrix Formalism

Spatial variance in permittivity is important for photonic crystals (PC). A change in permittivity indicates a change in medium. To evaluate electromagnetic waves propagating in changing permittivity, boundary conditions become important. Figure 2.1 illustrates the boundary conditions well.
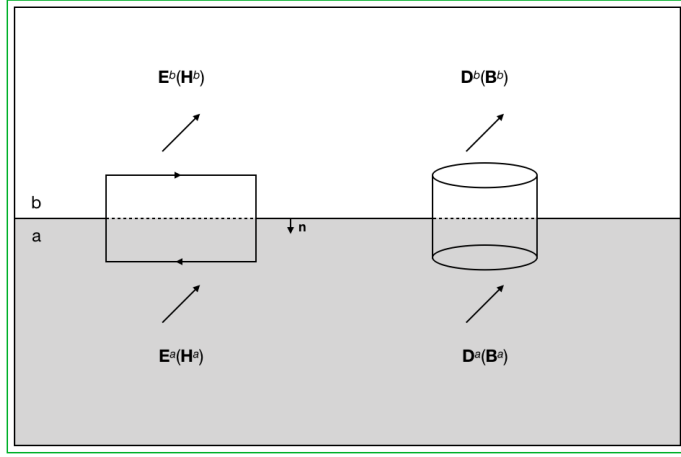
Figure 2.1: Depiction of how the tangential components of fields and normal components of fluxes behave at a boundary. Tangential components of **E**- and **H**-fields and normal components of **D**- and **B**-fluxes must be continuous across a boundary. In agreement with equations 2.29-2.32.

Figure 2.1 illustrates two different materials, a and b, with different permittivity. The rectangular box to the left illustrates that the tangential components of the **E**- and **H**-field must be continuous across the boundary. Tangential, meaning parallel to the boundary. The cylindrical box to the right illustrates that the normal components of the **D**- and **B**-fluxes must be continuous across the boundary. The normal component is present in the figure as $\boldsymbol{n}$. The requirement of continuous components across the boundary comes from the need for conservation of momentum. An other way to think about this is; to prove conservation of momentum we need to use Gauss's electric Equation 2.1 and magnetic Equation 2.2. When considering Gauss's equations over a small but finite area the boundary conditions become apparent. The following equations explain the boundary conditions, illustrated by Figure 2.1.

$$\mathbf{n} \times (\mathbf{E^a} - \mathbf{E^b}) = 0 \tag{2.29}$$

$$\mathbf{n} \times (\mathbf{H^a} - \mathbf{H^b}) = \mathbf{J}_s \tag{2.30}$$

$$\mathbf{n} \cdot (\mathbf{B^a} - \mathbf{B^b}) = 0 \tag{2.31}$$

$$\mathbf{n} \cdot (\mathbf{D^a} - \mathbf{D^b}) = \rho_s \tag{2.32}$$

s is denoting the boundary surface in Equations 2.29-2.32. Since we already are assuming no currents or free charges, the right hand side of Equations 2.30 and 2.32 are set to zero.
In the following only monochromatic waves of various polarization at a boundary are considered. The polarization states are TE/s-polarized and TM/p-polarized waves [55]. Any

other form of polarization can be decomposed into these two polarization states, and only offer complications without any further insight.
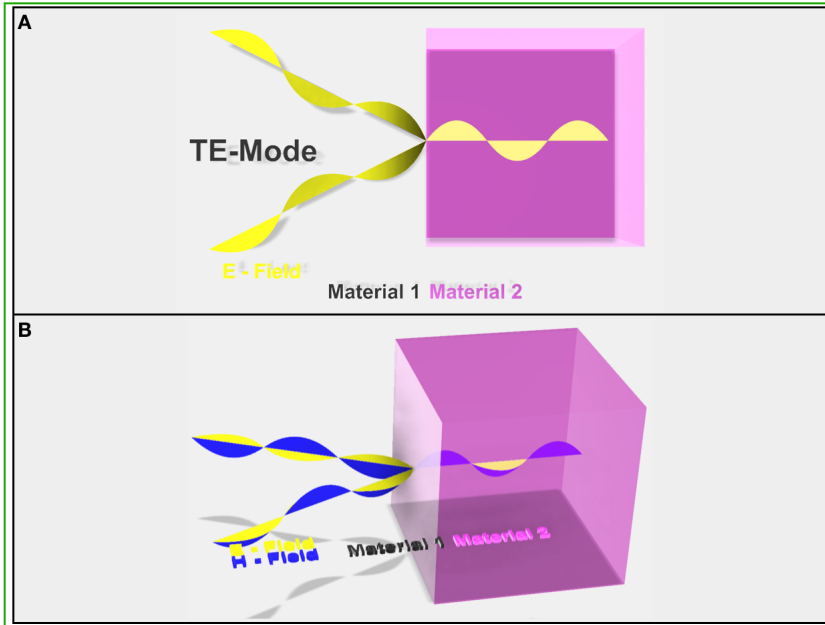
Figure 2.2: Figure A illustrates a TE polarized wave interacting with two different materials (Materials 1 and 2). Materials 1 and 2 are distinguished by having different refractive indices. E-field amplitude and wavelength is illustrated in yellow. Figure B also illustrates a TE-polarized wave interacting with materials 1 and 2, but here the H-field is added. H-field is illustrated in blue. E-field components are interacting in the plane of changing refractive index (same plane as the text). H-field is interacting in the plane perpendicular to that of the E-field, with its field components along the axis of constant refractive index.

Figure 2.2 A illustrates a TE-polarized wave interacting with two different materials. Figure 2.2 B also illustrates a TE-polarized wave interacting across a boundary between two different materials. The yellow and blue waves are E-field and H-field, respectively. A TE-polarized wave is defined as a wave with its field components interacting in the plane of changing refractive index. TM-polarization is subsequently defined as a wave with its field components interacting in a plane parallel to the boundary surface. Interchanging the E- and H-field in Figure 2.2 results in a TM-polarized wave. With the situations illustrated in Figure 2.2, Fresnel's equations (FE) can be presented. The reader is referred to "Photonics" by A. Yariv and P. Yeh for the derivation of FE [69].

$$r_{te} = \frac{n_1 \cos \theta_i - n_2 \cos \theta_t}{n_1 \cos \theta_i + n_2 \cos \theta_t} \qquad (2.33)$$

$$t_{te} = \frac{2n_1 \cos \theta_i}{n_1 \cos \theta_i + n_2 \cos \theta_t} \qquad (2.34)$$

$$r_{tm} = \frac{n_2 \cos\theta_i - n_1 \cos\theta_t}{n_2 \cos\theta_i + n_1 \cos\theta_t} \tag{2.35}$$

$$t_{tm} = \frac{2n_1 \cos\theta_i}{n_2 \cos\theta_i + n_1 \cos\theta_t} \tag{2.36}$$

Equations 2.33-2.36 are known as Fresnel's equations (FE) for reflectance and transmittance [69]. FE depend on the angle of incidence, θ_i, angle of transmittance, θ_t, and the refractive indice on both sides of the boundary, n_1 and n_2. The refractive index, n_1, n_2 is related to the permittivity and the permeability of the respective medium, as in Equation 2.37.

$$n = \sqrt{\mu_r \epsilon_r} \tag{2.37}$$

Under the current assumptions, see Section 2.2, and with only para- and dia-magnetized material, n becomes a real-valued parameter only varying with ϵ_r. Since the permittivity is generally frequency dependent the refractive index also generally becomes frequency dependent. The zero-valued off diagonal components of Matrix 2.27 also implies a non-dispersive system. The refractive index, in Equation 2.37, is assumed to be constant across all frequencies. An assumption that does not resemble the natural behavior of the refractive index. For the scope of this paper the refractive index is assumed to be constant across the band-width of any source. Which is a valid assumption whenever the absorption spectra of the material in question is constant. The absorption spectra for silicon in the 1550 nm region is flat and low [60].

A one-dimensional photonic crystal is illustrated in Figure 2.3.
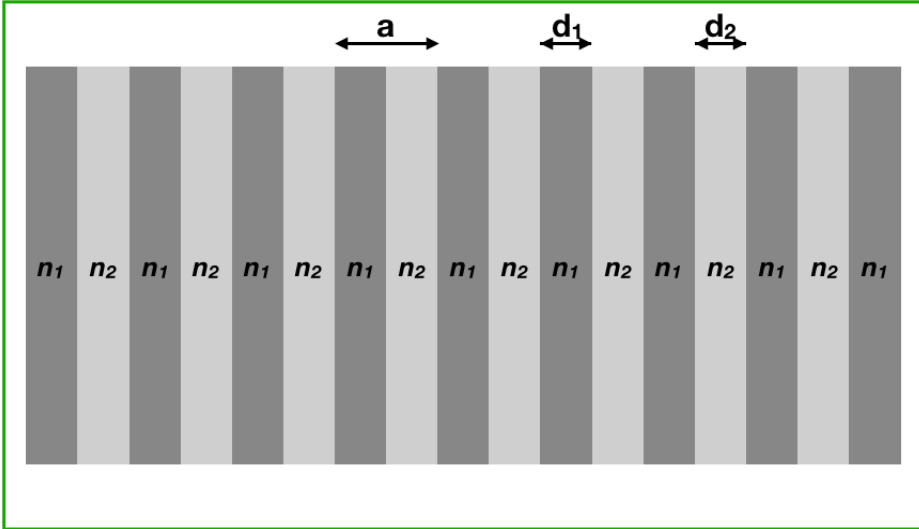
Figure 2.3: A stacked material with alternating refractive index n_1 and n_2. a marks the periodicity and lattice constant of the structure, d_1 and d_2 indicates the distribution of the two materials.

A one-dimensional photonic crystal is a structure that contains variation of permittivity only along one spatial axis. The variations are on the order of the incoming fields wavelength [31]. A photonic crystal clearly resembles a distributed Bragg reflector (DBR), only the DBR is intended to reflect certain wavelengths whereas the photonic crystal has a broader purpose [55]. When evaluating a one-dimensional photonic crystal one must evaluate the fields at each boundary constituting the photonic crystal. Figure 2.4 illustrates how the evaluation can be structured in what is known as a M-matrix [69]. The input fields, denoted $U^{(-)}$ in Figure 2.4, are multiplied with the M-matrix to determine the output fields, denoted $U^{(+)}$. U is a potential field, and is used to represent either an **E**- or **H**-field. M-matrices can be multiplied together to produce the overall transmittance and reflectance of the one-dimensional photonic crystal, similar to what is done in Equation 2.39.
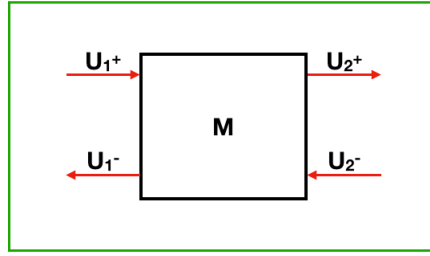
Figure 2.4: Illustration of a linear system represented by a M-matrix relating the output potential fields to the input potential fields. The potential field U is representing either an **E**- or **H**-field.

An overall system matrix representation, M, is given in Equation 2.39.

$$M = \begin{bmatrix} M_{xx} & M_{xy} \\ M_{yx} & M_{yy} \end{bmatrix} \tag{2.38}$$

$$\begin{bmatrix} E_x^o \\ E_y^o \end{bmatrix} = \begin{bmatrix} M_n \end{bmatrix} \begin{bmatrix} prop_n \end{bmatrix} ... \begin{bmatrix} prop_1 \end{bmatrix} \begin{bmatrix} M_1 \end{bmatrix} \begin{bmatrix} E_x^i \\ E_y^i \end{bmatrix} \tag{2.39}$$

The physical interpretation of the M-matrix entries is not straight forward, but they contain the reflection and transmission coefficient described in Equations 2.33-2.36. See reference [69] for further explanation. A propagation matrix describes an electromagnetic wave's behaviour between the boundaries. Matrix 2.40 is an example of an electromagnetic wave propagating over a distance d.

$$prop = \begin{bmatrix} e^{-i\omega d} & 0 \\ 0 & e^{-i\omega d} \end{bmatrix} \tag{2.40}$$

The off-diagonal components of the $prop$-matrix in Matrix 2.40 corresponds to propagation in a lossless and dispersionless medium.
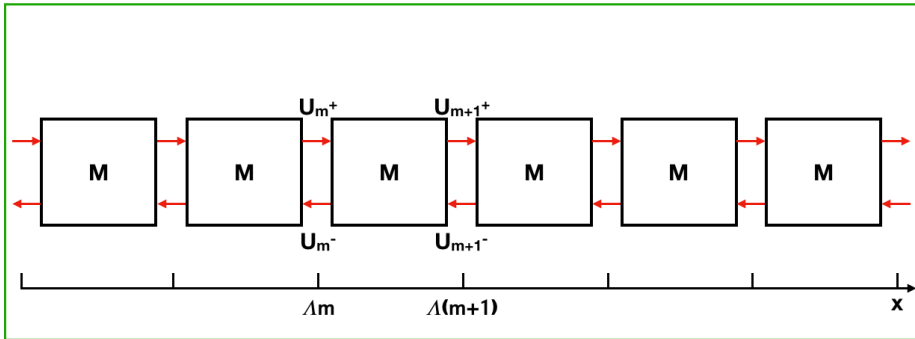
Figure 2.5: The x-axis is showing the periodicity Λ and the matrices above depict schematically equation 2.39. The propagation matrices must be added where the red-arrows are. **E**- and **H**-fields are represented by the potential function U here [55].

A system as the one illustrated in Figure 2.5 results in a frequency dependent transmission plot similar to that of Figure 2.6. The transmission plots change depending on the polarization state of the incoming field. The change in transmission comes from the differences in FE.
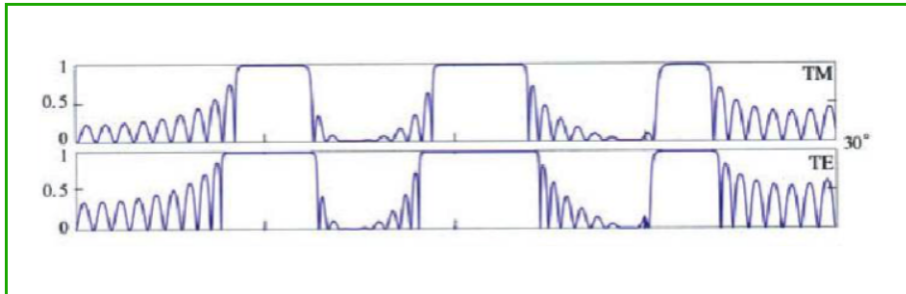
Figure 2.6: Transmission plot for an unknown one-dimensional crystal. The angle of incidence is $30°$. The horizontal axis is normalized frequency. The transmission is dependent on polarization, as expected from Fresnel equations [55].

2.4 Energy Confinement in Photonic Crystals

Within the one-dimensional PC there is propagation of forward- and backward-propagating waves. Certain frequencies result in constructive interference and other frequencies in destructive interference of the forward and backward propagating waves. Standing waves appear when the backward- and forward-propagating waves constructively interfere. Standing waves occur at the band-edge of photonic crystals, see Figure 2.11 in Section 2.6. A standing wave at the upper band edge is a standing wave that concentrates within the high index material. Similarly, a standing wave at the lower band edge is a standing wave that concentrates within the low index material [31]. The location of the different standing

waves and the relation to frequency is explained by the electromagnetic variational theory. For the derivation of the electromagnetic variational theory the reader is referred to "Photonic Crystals: Molding the flow of light" by J. D. Joannopoulos et al. [31]. The Energy functionals starting from the variational theory, lead to the expression in Equation 2.42.

$$U_f(\mathbf{H}) = \frac{(\nabla \times \mathbf{E}, \nabla \times \mathbf{E})}{(\mathbf{E}, \epsilon(\mathbf{r})\mathbf{E})} \tag{2.41}$$

$$U_f(\mathbf{H}) = \frac{\int d^3\mathbf{r}|\nabla \times \mathbf{E}(\mathbf{r})|^2}{\int d^3\mathbf{r}\epsilon(\mathbf{r})|\mathbf{E}(\mathbf{r})|^2} \tag{2.42}$$

From Equation 2.42 it becomes apparent that to minimize the energy functional the energy needs to be concentrated to areas of high permittivity, maximizing $\epsilon(\mathbf{r})$.
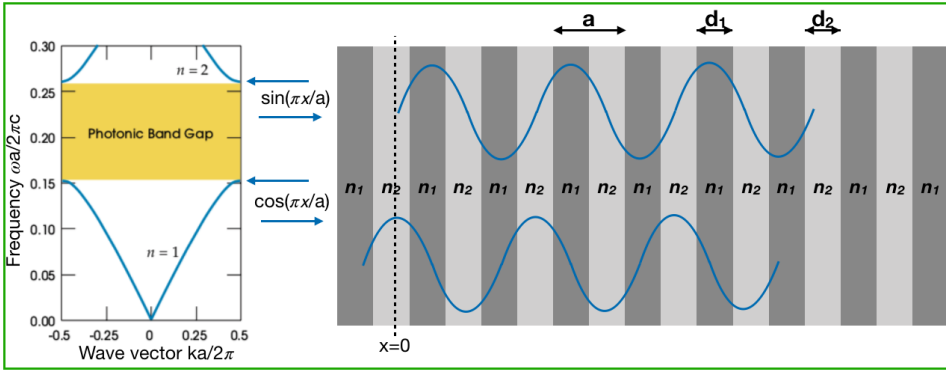
Figure 2.7: Illustration of how degenerate modes concentrate differently within a one-dimensional PC and how it results in a band-gap in frequency.

Figure 2.7 illustrates how degenerate modes both being standing waves, concentrate in a one-dimensional PC. The state with low frequency is concentrated in the high index material, $\mathbf{n_2}$ being the high index material. The two solutions to the degenerate mode results in a band-gap in frequency. The higher the contrast is between the two materials the larger the resulting band-gap becomes [31].

When proceeding to the two-dimensional PC, the second dimension adds some complexity to the structure. The best way to describe the more complex two-dimensional structure is through symmetry theory.

2.5 Effective Refractive Index and Coupling

Effective Refractive Index (ERI) is a natural extension from energy confinement, and instrumental for understanding coupling between guided modes in waveguides and defects in PC. From Figure 2.7 Section 2.4 it is clear that not all the energy is confined in either $\mathbf{n_1}$ or $\mathbf{n_2}$ but rather a distribution of the two.
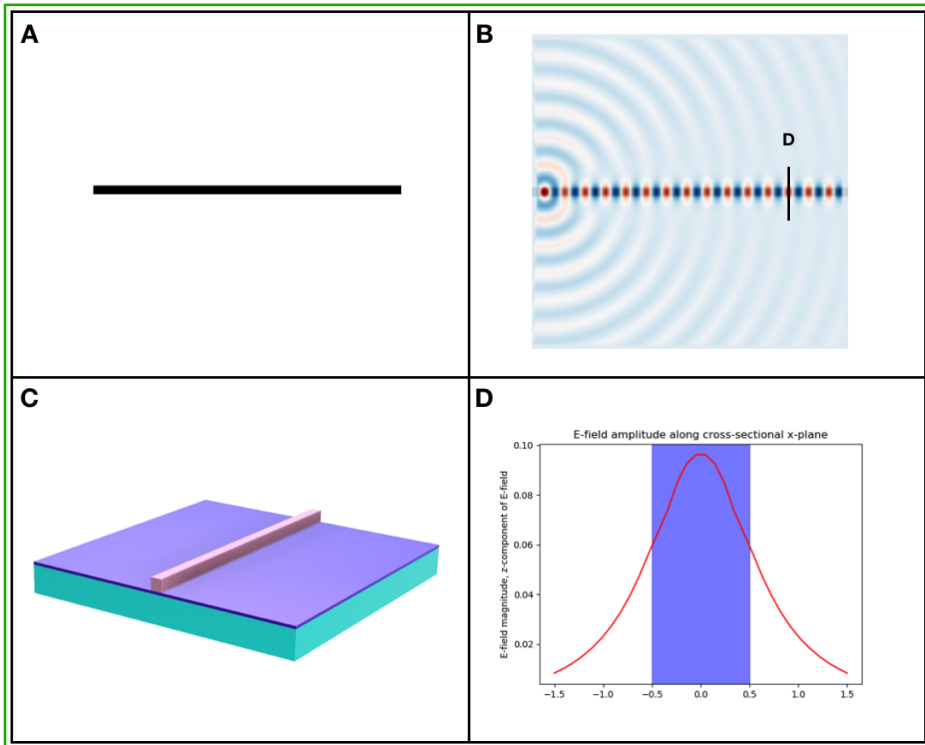
Figure 2.8: Figure **A** is a two-dimensional illustration of a slab waveguide. Figure **B** is a time domain simulation over the strip waveguide in Figure **A**. The source of the simulation is located to the left, almost at the end of the strip waveguide. Confinement of light to the strip waveguide becomes evident as the light propagates from left to right. Figure **C** is a three-dimensional illustration of the same strip waveguide. Figure **D** is a cross-sectional plot of the E-field along the x-plane. The blue shaded area resembles the width of the strip waveguide. The cross-sectional marker **D** in Figure **B** is the position along the strip waveguide where Figure **D** is located.

Figure 2.8 A is a top view of a waveguide, B illustrates the z-component of an E-field propagating within and along the waveguide in A. C is a three dimensional view of the waveguide, illustrating the permittivity difference in the cladding (permittivity of 5) and permittivity of waveguide (permittivity of 12). The Permittivity in this case is arbitrary, although the contrast in permittivity is not arbitrary. A higher contrast in permittivity results in an E-field more confined to the waveguide. Stated as a statistical explanation, the variance of the cross-sectional magnitude is smaller for a higher permittivity contrast. D is a mapping of the E-field z-components magnitude across the cross-section of the waveguide. Position **D** in Figure B marks where the cross-sectional view in figure D is located along the waveguide. The shaded blue area illustrates the horizontal span of the waveguide. The fundamental mode is exponential decaying or the wave is evanescent outside the blue shaded region. Inside the blue shaded region the fundamental mode propagates as a standing wave. The interaction across the borders between the blue and white regions are governed by conservation of momentum and the boundary conditions (see Equations

2.29-2.32). The underlying material of where the mode's cross-sectional position is varying. The cross-sectional change in refractive index gives rise to the ERI. ERI being defined as the distributed refractive index where the energy distribution dictates the distribution of the refractive index. A consequence of ERI is coupling between modes in near proximity, both spatially and in terms of frequency. Near proximity in frequency can be understood as; a mode existing in a high refractive index area cannot couple to a nearby identical high index area and become a higher mode with a higher frequency (valid for linear medium). How near the spatial proximity must be to facilitate coupling depends on the refractive index contrast, the higher the contrast the smaller the proximity must be. The nearby high index area needs to locate within the exponential decaying area of the mode. Figure 2.9 illustrates coupling between two parallel waveguides.
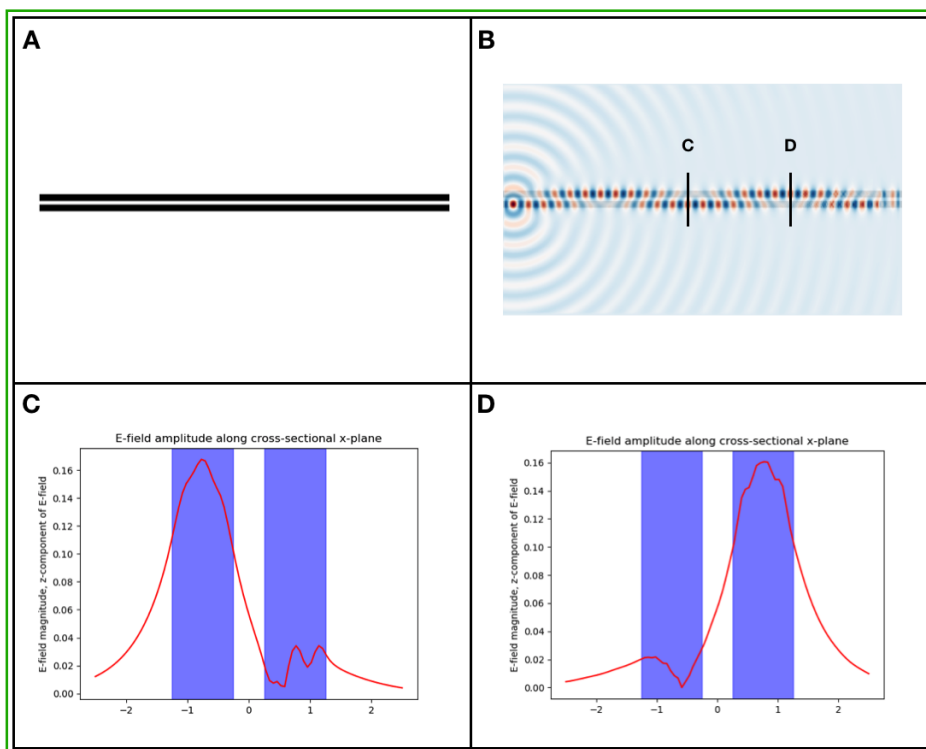
Figure 2.9: Figure **A** is a two-dimensional illustration of two parallel slab waveguides. Figure **B** is a simulation over the two parallel strip waveguides in Figure **A**. The source of the simulation is located to the left, almost at the end of the bottom strip waveguide. Confinement of light to, and the alternation of light between the two strip waveguides becomes evident as the light propagates from left to right. Figure **C** and **D** are cross-sectional plots of the E-field along the x-plane at two different locations. Their locations are marked in Figure **B** as marker **C** and **D**. The blue shaded areas in Figure **C** and **D** resemble the strip waveguide widths. From Figure **B**, **C**, and **D** it is evident that light couples back and forth between the two strip waveguides as light propagates from left to right.

Figure 2.9 A is a top view of two parallel waveguides, B illustrates the z-component of an E-field propagating within and along the waveguides in A. Figure C and D are both mappings of the E-field z-components magnitude across the cross-section of the waveguides. Positions C and D mark where the cross-sectional views in Figures C and D are located along the waveguides, respectively. From figures B, C, and D it is clear that the E-field magnitude couples back and forth between the two waveguides as the E-field propagates down the length of the waveguides. The evanescent fields in Figures C and D have a sufficient magnitude to facilitate coupling.

2.6 Symmetry Theory

Symmetry and group theory are effective tools when complex structures have an underlying much simpler symmetry that can describe the structure without loss of information [49]. Most two dimensional photonic structures are inherently symmetric. Non-symmetric photonic crystals would be extremely complex to describe or characterize. The two-dimensional photonic crystals presented in this thesis have a six-fold rotational symmetry. A six-fold rotational symmetry can be described by the following matrix.

$$C_6 = \begin{bmatrix} \frac{1}{2} & -\frac{\sqrt{3}}{2} & 0 \\ \frac{\sqrt{3}}{2} & \frac{1}{2} & 0 \\ 0 & 0 & 1 \end{bmatrix} \tag{2.43}$$

Some assumptions have been made for the six-fold symmetry matrix to be valid. The matrix entries in Equation 2.43 are given in a Cartesian coordinate system where entry 11 (top-left corner) represents the x-axis, entry 22 (center) represents the y-axis, and entry 33 (bottom-right corner) represents the z-axis. The z-axis is chosen as the third dimension, meaning permittivity variations in two-dimensional photonic crystals are exclusively manifested in the xy-plane. When applying a six-fold symmetry rotation to a system, the rotation in this context is applied around the z-axis. This is also the reason why entry 33 remains unchanged, or has a value of unity.

The two-dimensional photonic crystals presented in this thesis are based on the symmetry shown in Figure 2.10
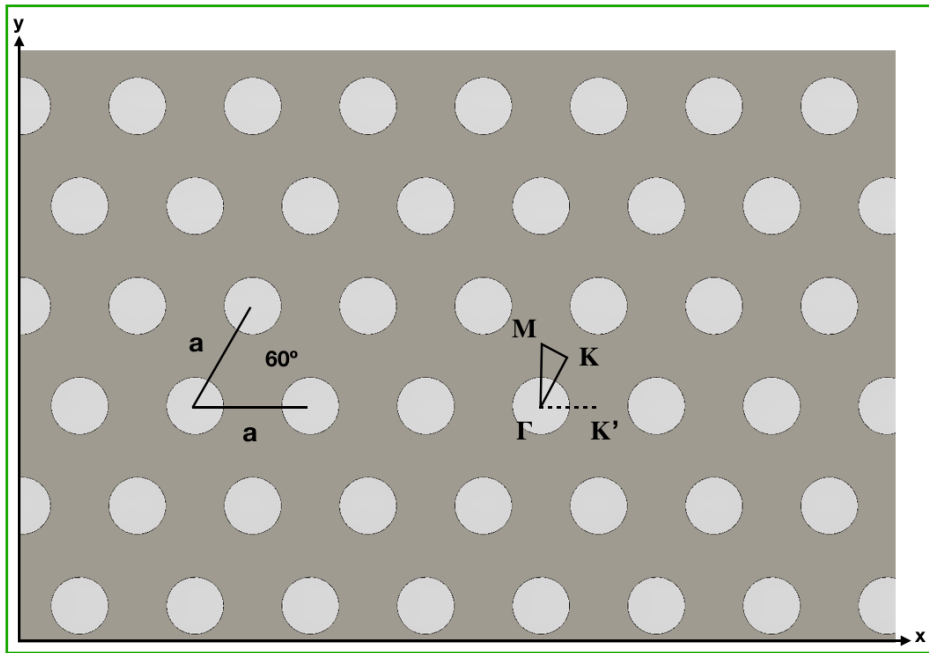
Figure 2.10: a is the lattice constant. The lattice constant is the smallest translational symmetry. **60°** illustrates the degeneracy in rotating 60 degrees, also known as six-fold symmetry. **x** and **y** mark a reference coordinate system allowing to see the change in refractive index along both axes, hence a two-dimensional PC. Points **Γ**, **M**, and **K** mark the corners of the irreducible Brillouin zone. **K'** mark the edge of the primitive unit cell in the positive x-direction.

In theory, the PC is assumed to extend to infinity in the xy-plane. If the rotational Equation 2.43 is applied to the PC, the same symmetry would be observed before and after the rotation, assuming the PC extends to infinity or has a six-fold symmetric boundary.
Another symmetry operation essential to understand photonic crystals is the translation symmetry operation. A translation symmetry operation can be described by a vector such as the general one in Equation 2.44.

$$T_{xyz} = \begin{bmatrix} T_x \\ T_y \\ T_z \end{bmatrix} \tag{2.44}$$

In the context of two-dimensional photonic crystals only translations in the xy-plane can be applied, and consequently only the entries one and two of the translation vector can be non-zero. The smallest translation symmetry in the hexagonal photonic crystal, creating an identical observed symmetry after each operation, is a translation of distance Λ along the six-fold axis, see green marker in Figure 2.10. The translation distance Λ is also the lattice constant. The points located a translation distance Λ apart are called lattice points.
The symmetry operations can now be applied to the two-dimensional hexagonal PC. The

intention behind applying these symmetry operations to the PC, is to find the smallest possible area containing all of the spatial information the PC has to offer.

Starting with the translation operation along the six-fold axes, the Wigner-Seitz cell is defined as all the points in space that are closer to a reference lattice point than any other lattice point [49]. Related to Figure 2.10 the Wigner-Seitz cell extends half the lattice constant (black line denoted a) in the positive x-direction. The area of consideration can be reduced beyond the Wigner-Seitz cell without loosing any information. By inverting the six-fold axis the first Brillouin zone is obtained, illustrated as the hexagonal structure in Figure 2.11. The first Brillouin zone is the reciprocal space equivalent to the Wigner-Seitz cell. By applying six-fold rotational symmetry to the first Brillouin zone the area of consideration is reduced to a triangular area twelve times smaller than the the first Brillouin zone. This new area is called the irreducible Brillouin zone, and contains just as much spatial information as any other zone or cell mentioned above. The irreducible Brillouin zone is illustrated as the blue shaded triangle inside the first Brillouin zone in Figure 2.11. The contour of the irreducible Brillouin zone are lines of high symmetry, and where most maximums and minimums of propagating states in a photonic crystal appear [31]. The lines of high symmetry are the lines plotted along the horizontal axis in a band diagram, see Figure 2.11 and the triangle in Figure 2.10.
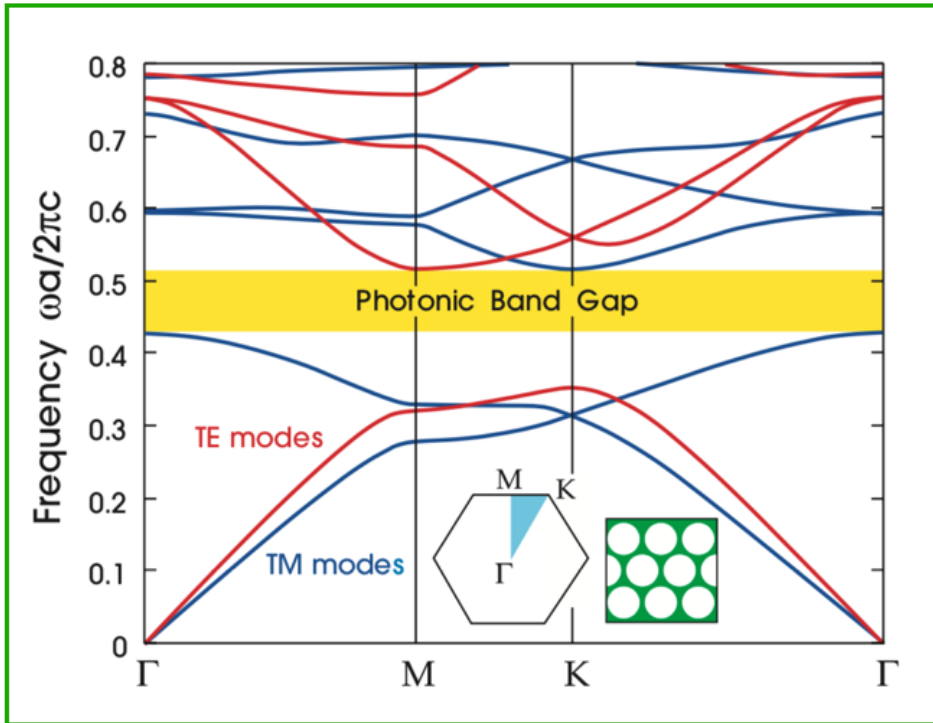
Figure 2.11: The yellow area is illustrating a complete photonic band-gap (for all polarizations). The white hexagonal structure centered in the bottom of the figure is the first Brillouin zone, and the blue triangle inside of it is the irreducible Brillouin zone. The horizontal axis is tracing the lines of high symmetry and the vertical axis is normalized frequency. The frequency is normalized with respect to the lattice constant a and speed of light, c (reprinted from [31]).

The lines in the band diagram 2.11 are propagating states within the irreducible Brillouin zone, and thus the propagating states within the photonic crystal structure. The frequency axis in Figure 2.11 is normalized by the lattice constant and the speed of light. For some frequencies there are no propagating states anywhere in the irreducible Brillouin zone. The frequency band with no propagating states, constitute what is called a photonic band-gap. The photonic band-gap is illustrated in Figure 2.11 as the yellow shaded area. Photonic band-gaps are equivalent to the regions in Figure 2.2 corresponding to zero transmission. Only evanescent waves can exist within a photonic band-gap [55]. By introducing point- and line defects propagating states become allowed within the photonic band-gap. The propagating states within the photonic band-gap are forced to propagate within the defects, and only decay evanescently outside the defects.
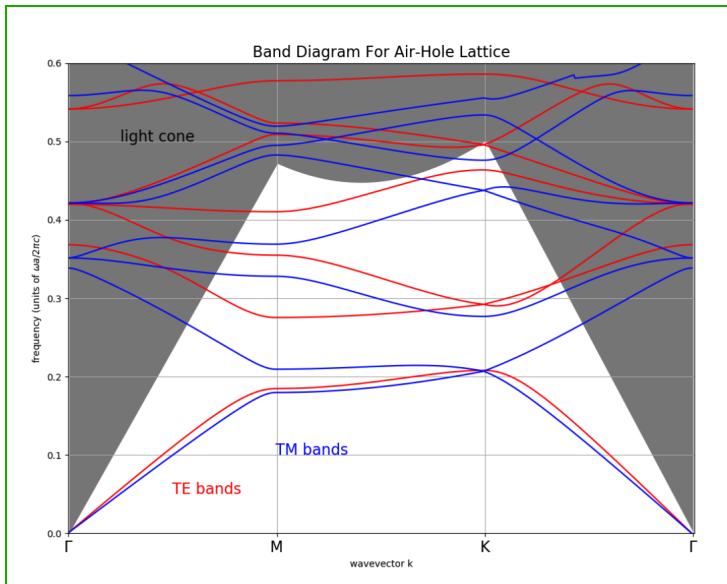
Figure 2.12: Band diagram for a hexagonal symmetric photonic crystal including the light cone. The TE and TM bands are shifted in frequency compared to Figure 2.11. The shift is caused by a difference in air-hole radius (air hole radius in Figure 2.11 is 0.48a while in this figure it is 0.3a). Frequency is given in units of $\omega a/2\pi c$ and wavevector k is given in units of $2\pi a/\lambda$.

Figure 2.12 is a similar band diagram to that of Figure 2.11. It differs in that it only illustrates TE-bands and that it offers information about the light cone. The light cone is a projection of all states that can radiate into the cladding, in this case air. The light cone is an important factor when evaluating and designing PC devices. Propagating states within a PC device can couple to the cladding (light cone states) if the difference in k-vector between a propagating state and light cone state becomes small enough.

2.7 Defects In Photonic Crystals

Defects in PC are intended interruptions of symmetry. The hexagonal photonic crystal structure has a six-fold rotational symmetry and a translational symmetry along the lines of high-symmetry (Γ, M, and K). By introducing defects, the symmetries at best become perturbed. The PC border is in the same way an interruption to the underlying symmetry but is often neglected when considering PC. Defects can typically be point or line defects.
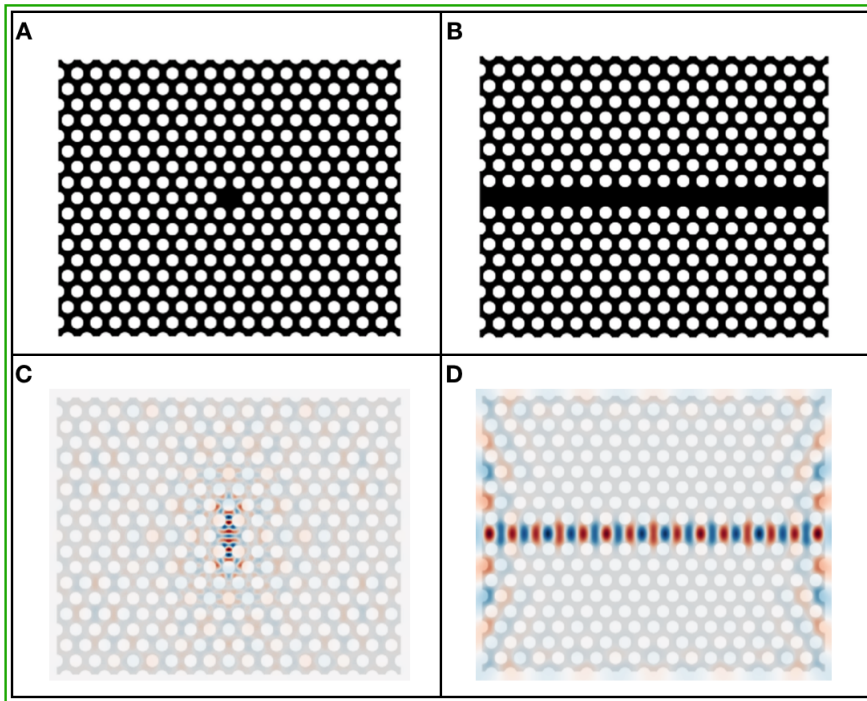
Figure 2.13: Figure **A** illustrates a two-dimensional PC with a point defect in its center. The defect is designed by simply removing one air-hole. Figure **B** illustrates a two-dimensional PC with a line defect. The defect is designed by simply removing one row of air-holes. Figure **C** is a FDTD simulation over the point defect. The point defect clearly confines a large portion of the electric field. Figure **D** is a FDTD simulation over the line defect. The line defect clearly confines and guides the electric field within the defect.

2.7.1 Point Defect

A point defect is an alternation of the dielectric function around a single lattice point. A defect-free PC exhibits a dispersion relation similar to that illustrated in Figure 2.11. A defect introduces localized modes both inside and outside of the photonic band-gaps. The newly introduced modes that lie within the band-gap are usually of more interest and are subject to engineering considerations. The defect can be carefully design, often by controlling the hole size or shifting the hole center to tune the defect mode's frequencies. A defect mode within the photonic band-gap, localized at the corresponding defect site is allowed to propagate at the defect site. A fact that might be obvious but nonetheless should be emphasized. The defect mode decays evanescently away from the defect site spatially. The PC symmetry and its corresponding photonic band-gap behaves as an omnidirectional mirror for the defect mode. A point defect with a defect mode localized within the photonic band-gap can act as resonators with very high Q-factors.

2.7.2 Line Defect

A line defect is an alternation of the dielectric function around consecutive lattice points forming a line. The perturbation introduced by a line defect is often more severe than that of a point defect. A line defect, in the same way as a point defect introduces defect modes. Defect modes located within the photonic band-gap propagates along the line defect and evanescently outside the line defect. The mode profile of a PC guided waveguide is much like a mode of a slab waveguide. A PC line defect, also known as PC guiding is fundamentally different from slab waveguides in how it confines light. A slab waveguide confines light with only one material interface. Since there is only one material interface, the light becomes confined by total internal reflection (TIR). PC guiding confines the light by gap guiding. Gap guiding refers to a a guided mode being confined by a photonic band-gap. With slab waveguides the light has to be confined to a high index material surrounded by a lower index material. With PC guiding the light can be confined to a low index material as well as a high index material. Which material the light is confined to depends on the PC configuration and the mode number in question. For triangular air-hole PC purposes a line defect is usually introduced along the Γ-K direction of the PC (see Figure 2.10).

2.8   Frequency Analysis and the Fourier Transform

Fourier analysis (FA) is important to understand electromagnetic waves and their interaction with matter. The reader is assumed to have a fundamental understanding of FA. The reason why frequency analysis and the Fourier transform (FT) have their own section, and are sorted after Section 2.1, is because of their impact on design solutions. The theory in this section is intended to motivate for the design solutions and is tailored specifically for that purpose. The FT can mathematically be explained as.

$$g(sx) = \frac{1}{\sqrt{2\pi}} \int_{-\infty}^{\infty} f(x)e^{isx\cdot x}dx \tag{2.45}$$

The inverse FT is given as.

$$f(x) = \frac{1}{\sqrt{2\pi}} \int_{-\infty}^{\infty} g(sx)e^{-isx\cdot x}dsx \tag{2.46}$$

Equation 2.45 is the integral notation of the FT and relates spatial frequency variations of a function to its corresponding spatial variations [17]. Important for the design solutions (in Chapter 4) is how a spatial-varying function corresponds to its spatial-frequency counterpart function. The relation between a rectangular function and its transform, and a Gaussian function and its transform is especially important for the design solutions.

	Spatial variable, x	Spatial frequency, sx	
Rectangular function	$\sqrt{\frac{\pi}{2}}$ If $\|x\| < a$ 0 If $\|x\| > a$	$\frac{sin(asx)}{sx}, a > 0$	**Sinc function**
Gaussian function	$exp(ax^2), a > 0$	$\frac{1}{\sqrt{2\pi}}exp(\frac{sx^2}{4a}), a > 0$	**Gaussian function**

Table 2.1: Table containing Fourier transform pairs. Rectangular function and Sinc function are one pair. A Gaussian function Fourier transforms into an other Gaussian function [34].

Table 2.1 contains the FT pairs Rectangular-Sinc functions, and Gaussian-Gaussian functions. The mathematical picture of spatial constraints inflicted on a mode is illustrated in Figure 2.14.
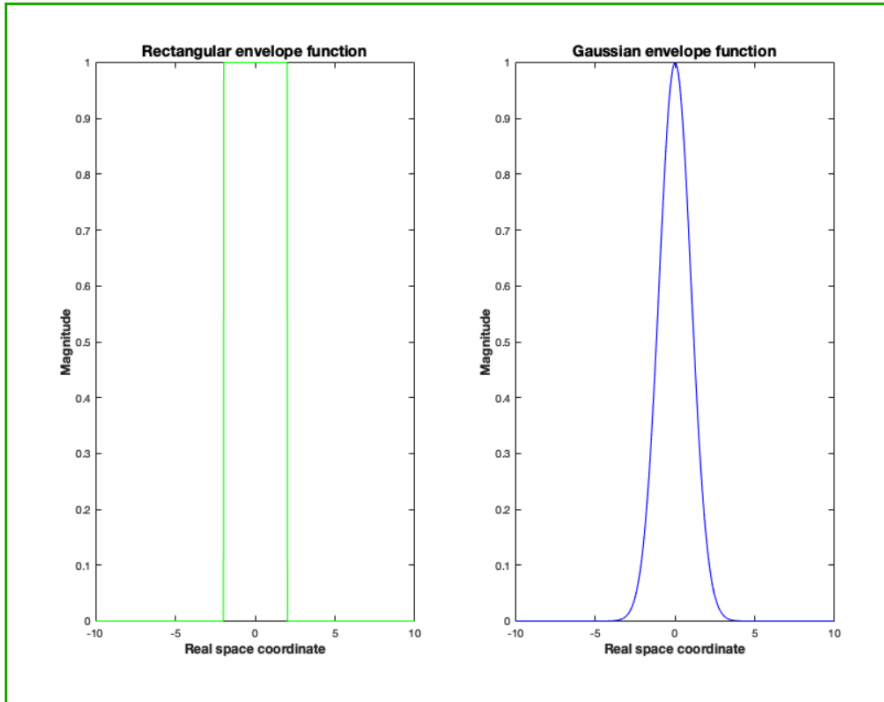
Figure 2.14: Plot illustrating the functions in table 2.1. Left graph illustrates the rectangular function, also stated mathematically in the top-left box of Table 2.1. Right graph illustrates the Gaussian function, also stated mathematically in the bottom-left box of Table 2.1. They mathematically illustrate the spatial constraints inflicted on a mode in a line defect (see Figure 3.4 for line defect).

Figure 2.14 illustrates the mathematical functions describing a regular cavity (left) and a Gaussian cavity (right). If the PC structure only is interrupted by a line-defect the mathematical description becomes a rectangular function. If the PC structure is interrupted by a line defect that is smoothened by either increasing hole radius or shifting the hole location to nearby holes the mathematical description becomes more Gaussian distributed like. The nearby holes can even be designed to trap the modes with a perfectly Gaussian mode profile [5].
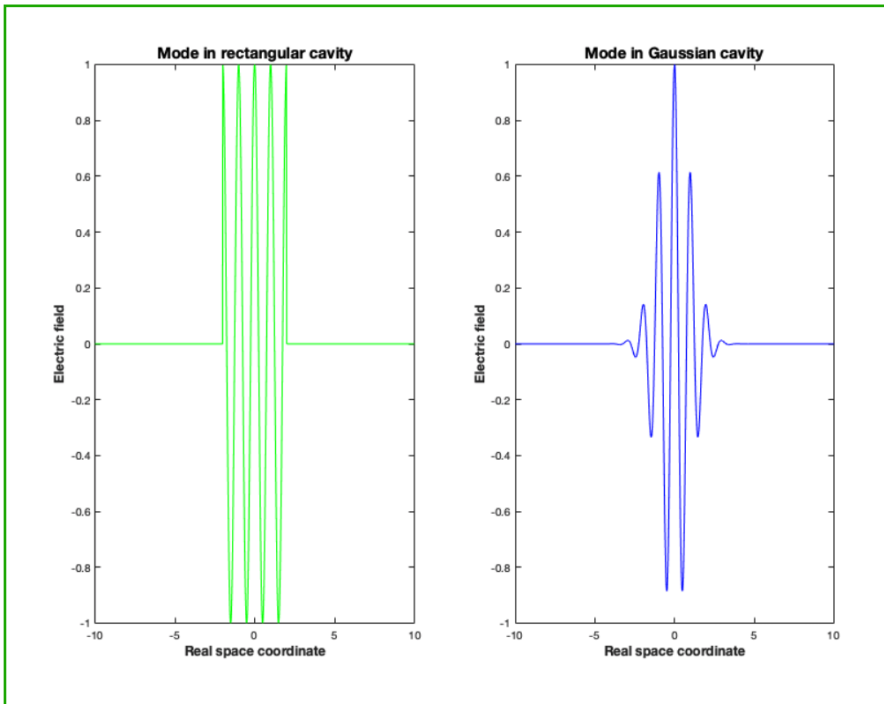
Figure 2.15: Plot illustrating a mode trapped in a rectangular cavity (green/left) and a mode trapped in a Gaussian cavity (blue/right).

Figure 2.15 illustrates two modes, one trapped in a rectangular cavity (green/left) and an other trapped in a Gaussian cavity (blue/right). The mode frequency becomes enveloped by the cavity representation. Figure 2.16 offers a better illustration of why the shape of the cavity matters, and why the Gaussian shaped cavity experience less loss compared to the rectangular cavity.
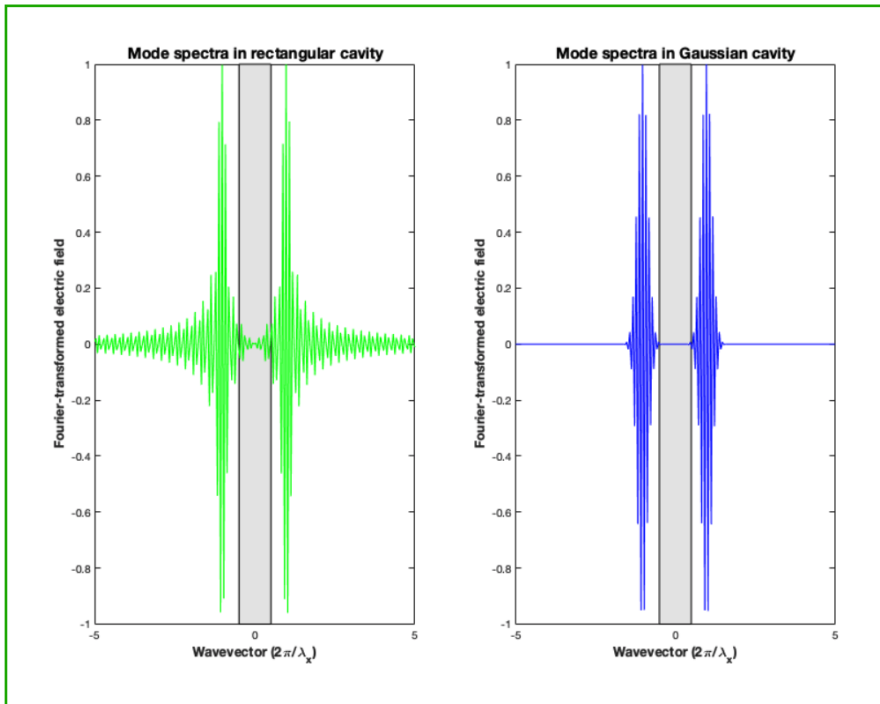
Figure 2.16: Spectra of the two trapped modes, rectangular cavity mode to the left and Gaussian cavity to the right. The gray area centered around a wavevector equal to zero defines leaky modes within the light cone. The rectangular cavity modes clearly exhibits more small frequency components, potentially leaking out into a surrounding cladding.

Figure 2.16 illustrates the spectras of the two trapped modes in Figure 2.15. Here again, the spectra for the rectangular cavity trapped mode to the left in green and the Gaussian cavity trapped mode to the right in blue. The gray area, centered around a wavevector of zero defines all frequencies belonging to leaky modes. Leaky modes are modes that can couple out to either the air above the silicon layer or to the silica layer below. There are more frequency components within the gray area for the rectangular cavity mode than there is for the Gaussian cavity mode. Designing line defects to exhibit Gaussian-like mode distributions can therefor reduce loss due to frequency components coupling to leaky modes [5].

2.9 Q-Factor

Q-factor (Quality factor) is a dimensionless measure of how long-lived a harmonic system is. For an underdamped oscillating systems it describes how long the system oscillates before it comes to rest. Q-factor is inversely proportional to imaginary frequency. By time-harmonic representation, modes can be represented as $\mathbf{U}(\mathbf{r})e^{i\omega t}$. An imaginary frequency component, ω_i results in an exponential increase (positive ω_i) or decrease (negative

ω_i) of **U** with time-evolution.

With regards to PC resonators the Q-factor becomes a measure of how well a mode is "trapped" within the resonator [69]. A well "trapped" mode interacts more with the resonator. The more a mode interacts with a resonator the lower the LOD for the sensor becomes. The Q-factor is defined mathematically in Equation 2.47.

$$Q = \omega \times \frac{\text{field energy stored by resonator}}{\text{power dissipated by resonator}} \tag{2.47}$$
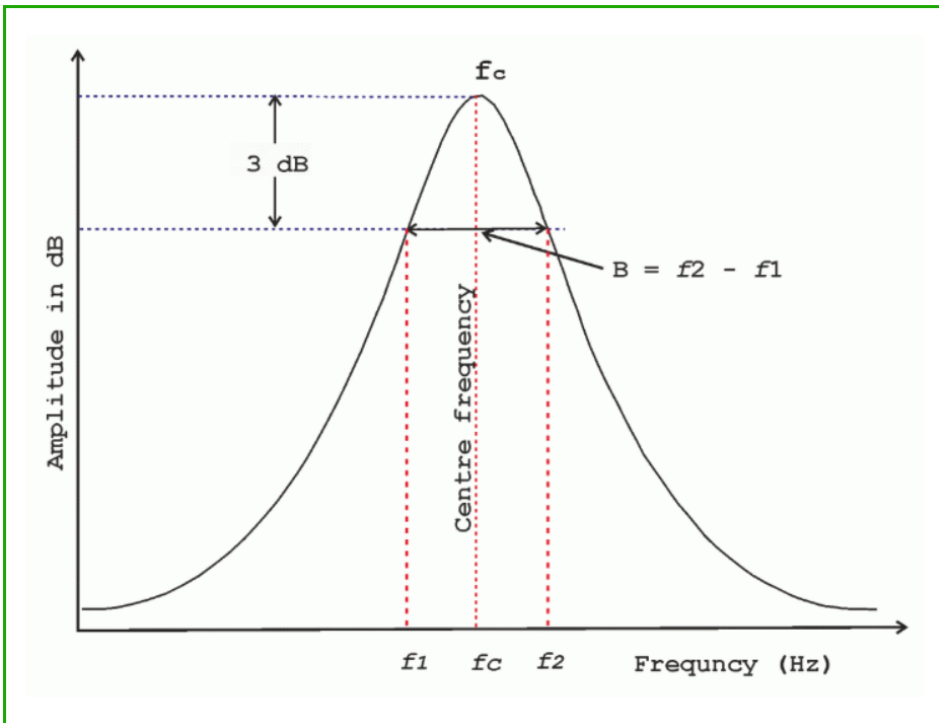
Figure 2.17: Illustration of how Q-factor is defined in frequency-space. The Q-factor increases with an increasing f_c and decreasing B. f_c is the center frequency of a mode, while B is the bandwidth of the mode at full-width-half-maximum (FWHM) (i.e. an amplitude reduction of 3 dB).

Figure 2.17 illustrates the Q-factor in frequency-space. In relation to Figure 2.17 the Q-factor can be defined as in Equation 2.48

$$Q = \frac{f_c}{B} \tag{2.48}$$

f_c is the center frequency of a mode, while B is the bandwidth of the mode at full-width-half-maximum (FWHM) or at an amplitude reduction of 3 dB. A high center frequency and a small full-width-half-maximum (FWHM) results in a high Q-factor. For such a case

the energy is highly localized in frequency, substantiating "trapping" of a mode. More specifically for PCRR energy stored can be given in terms of electric field, input power, permittivity, and mode volume. The result of substituting for energy is given in Equation 2.49.

$$Q = \frac{\omega \epsilon E_0^2 V}{4P} \tag{2.49}$$

P is the dissipated power, E_0 the electric field, ω the frequency, and ϵ the permittivity of the material where the q-factor is considered. The mode volume, V, is defined as the volume encapsulating the stored energy of consideration. Mode volume in context with PCRR is often the volume of the ring resonator itself. Q-factor and mode volume have a linear relation. If the mode volume increases, the q-factor increases linearly. Physically it makes sense that if the volume considered increases the mode long-livety also increases as it takes time for the mode to escape the considered volume. All ring resonators in this thesis are of the same size allowing the ring resonators to be compared directly by their q-factors. An intuition for Q-factor can be presented by considering a simple damped oscillator. The longer it takes for a damped oscillator to come to rest, the higher the oscillators q-factor is [17]. All PCRRs considered in this thesis can be modelled as underdamped oscillators. Q-factor is an important parameter in evaluating the performance of PCRR and is the parameter compared in Chapter 4.

2.10 Loss

There are several factors that in PC leads to loss. A general idea and understanding of these factors are beneficial for understanding the simulations and also to gain insight from the discussion following the results. Loss factors can be divided into intrinsic, geometrical, and fabrication losses. Intrinsic losses are related to the material in question and the surrounding physical environment affecting the material's properties. Geometrical losses accounts for loss related to geometrical configurations of PC and waveguide structures. It is common that fabricated devices have a reduced performance compared to the predicted results from simulations. In some situations geometrical loss naturally feeds into intrinsic loss, and vice versa.

2.10.1 Intrinsic loss

Intrinsic loss is associated with material properties and possible mis-matches when different designs are combined (i.e. slab waveguide/PC guiding). Dispersion loss is present in any light-matter interaction. Loss due to dispersion naturally depends on the frequency of the light. There are other loss mechanisms when considering material differences. Silicon comes in various constellations. Crystalline-silicon (c-Si) belongs to point group m3m (space group 227) while amorphous-silicon (a-Si) does not belong to any point group due to its lack of lattice structure. a-Si has a higher content of coordination defects due to its lack of lattice structure [48]. Coordination defects introduce dangling bonds which again introduce defect states in the band-gap. These defect states are unbound electrons from the dangling bonds interacting with photons from an external source. There are ways to

reduce the density of coordination defects, and they are discussed further in Chapter 3, Section 4.2.

2.10.2 Geometrical loss

Geometrical loss is loss associated with geometrical configurations in permittivity variations. When designing PCRRs, corner holes may be slightly changed in some way. Design choices might affect the overall loss of the structure. One design decision consistent for all PCRRs introduced in this thesis is the decision of using two-dimensional PC. One major source of loss regarding two-dimensional PC is out of plane loss. Along the third axis light is only confined by total internal reflection (TIR). TIR light confinement is highly dependent on refractive index contrast across the boundary. Figure 2.18 illustrates why high refractive contrast is important for light confinement.
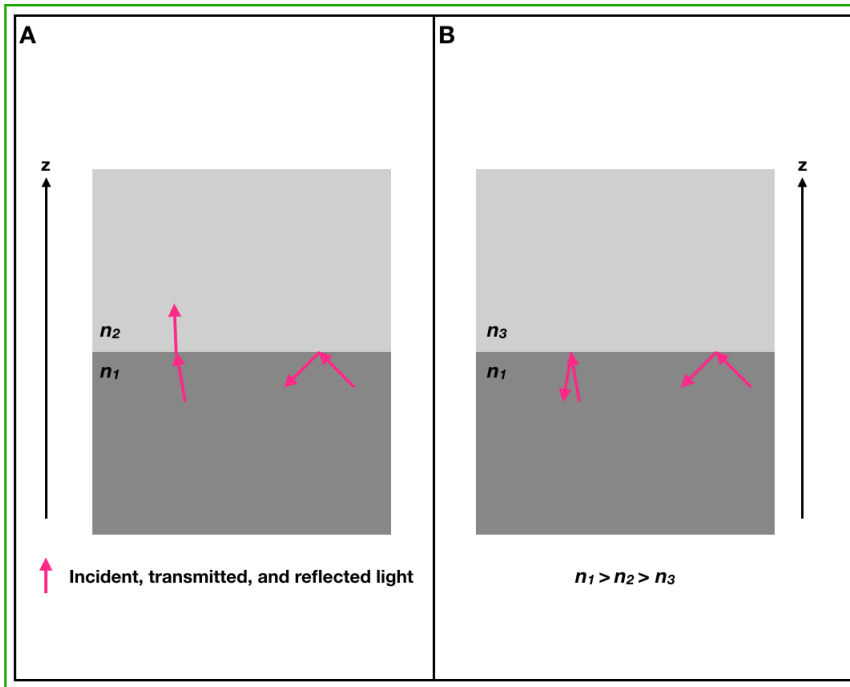
Figure 2.18: Illustration of out-of-plane loss. Figure **A** illustrates an interface exhibiting lower refractive contrast than the interface in Figure **B**. Both Figure **A** and **B** illustrate two different rays incoming at slightly different angles. For one of the two rays the reflective ray is identical for both figures. For the other ray the ray is reflected in figure **B** and transmitted in figure **A**. When the ray component parallel to the interface becomes too small TIR no longer occurs. The magnitude of the parallel ray component for which TIR no longer occurs depends on the refractive contrast across the interface.

Figure 2.18, **A** illustrates an interface exhibiting less refractive contrast than the interface in Figure **B**. Both Figure **A** and **B** illustrate two different rays incoming at slightly

different angles. For one of the two rays the reflective ray is identical for both figures. For the other ray the ray is reflected in figure **B** and transmitted in figure **A**. When the ray component parallel to the interface becomes too small TIR no longer occurs. The magnitude of the parallel ray component for which TIR no longer occurs depends on the refractive contrast across the interface. For triangular PCRR there is loss associated with the ring resonator corners. Explaining the ring resonator corner loss theoretically is complicated beyond stating that the corners introduce more reflections. Modification of ring resonator corners is therefore interesting from an optimization perspective. The PC hole radius is also a geometrical parameter that can be associated to loss. Generally speaking for triangular air-hole PC the photonic band-gap increases for TE-modes with increasing hole radius. With a larger band-gap it is easier to design a defect-state that does not couple to guided modes. Another prominent trend in triangular air-hole PC is the flattening of bands with increasing hole radius. When the dispersion relation flattens the group velocity goes down, and the light is slowed down. Mismatch between group velocity for slab waveguide and PC guided modes is also a source to loss.

2.10.3 Fabrication loss

Fabrication loss is any loss associated with fabrication imperfections. Many of these loss mechanisms are highlighted in Chapter 3, where fabrication methods are explained. Fabrication imperfections are typically roughness of PC holes, inclination of the side-walls of the waveguide and PC structure, imperfect anisotropic etch of PC holes, variation in etched radius of PC holes, and thickness variations in thin film layers. The origin of these imperfections can vary as more than one of the several fabrication steps are capable of producing imperfections. Roughness of PC holes can originate from poor PECVD deposited layer, from an unaligned EBL column, and from an un-optimized ICP-RIE process. Inclination to side-walls can come from an overly isotropic etch. Imperfect anisotropic etch is usually related to the etching process and the trade-off between ion bombardment and chemical etching [57]. All of these fabrication losses are further described in the proceeding chapter.

2.11   Light Coupling To Sample

Within photonics there are many different structures and devices that have been made. It is possible to distinguish between active and passive devices. An active device is a devise that exhibits a light source. LOC is made from silicon. Silicon exhibits indirect band-gap and therefor makes photon generation problematic. The LOC devices is a passive device because it must instead rely on an external source.

   The total loss that occurs between insertion and extraction of light from an optical device is referred to as insertion loss [7]. Many of the loss factors constituting insertion loss is mentioned in Section 2.10. Since the LOC is a passive device there is also loss related to light coupling from an external source to the optical device itself. For the devices fabricated in this thesis work the external light is guided from the source to the device through a fiber. Coupling the fiber directly to the waveguides on the device is referred to as butt-coupling. Reducing fiber device interface loss is beneficial, and suggestions for how to do so are many [63][12][40][39]. Most suggestions evolve around tapers or

diffraction optics. Both methods matches the mode size across the fiber-device interface. Tapers offer an adiabatic mode size conversion, by slowly increasing the waveguide cross-sectional area until the mode size match that of the fiber. Tapers are the simpler suggestion as they can be produced together with the PCRRs without any additional fabrication steps. Three-dimensional tapers are ideal for mode matching, but challenging to fabricate [12]. Figure 2.19 illustrates a suggested inverse taper waveguide.
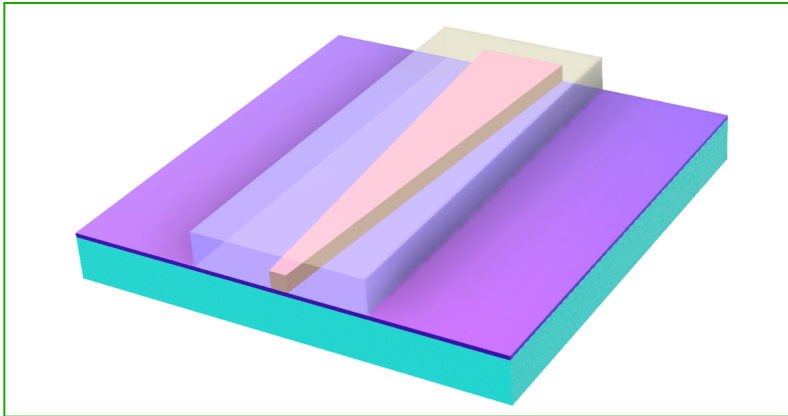
Figure 2.19: Illustration of an inverse taper waveguide. The waveguide is tapered from small to normal waveguide cross-section, opposite of traditional tapers. The waveguide is coated with a polymer material.

The taper forces the mode to expand while the polymer material confines the mode, preventing light to couple out and escaping the device [65]. The device-fiber interface is less sensitive to misalignment when an inverted taper design is implemented [46].

3. Simulation and Fabrication Methods

This chapter describes the simulations and fabrication methods used to design and fabricate the PCRR structures. Simulation tools used are MIT Photonic Bands (MPB) and MIT electromagnetic equation propagation (Meep). They are both simulation tools built on conventional algorithms for solving light-matter interaction, although they vary in which domain they are solving for. Plasma Enhanced Chemical Vapor Deposition (PECVD), Electron Beam Lithography (EBL) and Inductively Coupled Plasma-Reactive Ion Etching (ICP-RIE) are fabrication tools used to process the PCRR. All three are fabrication steps and instruments are well known from CMOS technology. Both the simulation software and fabrication instruments are highly technical and have emerged from fields of extensive research. The description given in this thesis is not comprehensive. The descriptions are intended to be introductory but sufficient to understand why the specific software and tools are used. Detailed descriptions are given where necessary to understand the motivation behind certain decisions. For further details the reader is referred to the references.

3.1 Computational Electromagnetism

Computational electromagnetism is the process of computing electromagnetic waves and their interaction with matter. It is widely used in research and industry to solve theoretical problems related to antenna radiation, absorbance/scattering of small particles, electromagnetic compatibility, lens and waveguide development, and electromagnetic wave propagation in various devices. When structures become complex in their shape and material composition closed form solutions to Maxwell's equations (ME) can be difficult to derive. Computational electromagnetism offers a way to derive ME in these situations, often by pixelating the structure of interest and grinding through ME at all pixel boundaries. When pixelating the structure of interest the solution is merely an approximate solution that converges to the real solution with decreasing pixel size. The software used in this thesis is MIT Photonic Bands (MPB) and MIT electromagnetic equation propagation (Meep). Both are freeware and offer scriptability through scheme and python. Computational electromagnetism can be both time and memory consuming. Understanding the software's limitations, benefits, and inner workings is crucial both for running the simulations correctly and evaluating the simulation results.

3.1.1 MIT Photonic Bands

MPB is a frequency-domain solver (FDS) program. FDS performs a direct computation of the eigenstates and eigenvalues of ME, and specifically the master Equation 2.23 in a periodic medium. The direct computation of eigenstates and eigenvalues is performed using a planewave basis [2][32]. ME is transformed for sources and fields at a constant frequency into matrix form $Ax = b$. Matrix A is derived from the wave equation operator while column vectors x and b describe the field and source, respectively. A Yee-cell grid similar to that of Meep is the underlying discretisation allowing and deciding how the matrix representation is set up. For periodic mediums it is sufficient to only evaluate the dispersion relation, $\omega(\mathbf{k})$, for the irreducible Brillouin zone since the Bloch envelope of the magnetic field is periodic. The advantages of performing a frequency-domain simulation compared to time-domain are:

- Certainty of collecting all the eigenstates.

- The error in frequency in an iterative solver decays exponentially with the number of iterations.

- The frequency and the corresponding eigenstate is calculated simultaneously.

- The number of iterations is only weakly dependent of resolution [33].

MPB can also be used to produce the dispersion relation for periodic structures that exhibit some form of defect. For periodic structures with defects the finite unit cell is larger then the irreducible Brillouin zone of the corresponding periodic defect-free structure. Producing all dispersion relations can therefor be more time- and memory consuming. Introducing a defect is also generally accompanied with several new guided eigenstates. A traditional disadvantage with FDS methods is that all of the lowest eigenstates must be computed before the desired eigenstate can be computed. MPB offers a targeted eigensolver which computes the eigenstates in a given frequency region. This allows eigenstates associated with defects to be computed efficiently by only considering the bandgap of interest.

Scripting in MPB is similar to that of Meep. First the simulated structure must be defined. Secondly the solver evaluates the predefined structure before it outputs corresponding frequencies and eigenstates at various points in the predefined structure. The outputted data can be exported to a preferred program for graphical representation. Unlike Meep, MPB is not dependent on any initializing source (i.e. initial values).

3.1.2 MIT electromagnetic equation propagation

Meep is a FDTD program. The FDTD method solves Maxwell's equations (ME) in time and space according to initial- and boundary values. Solving ME in time allows for simulations of non-linear media as frequency no longer needs to be conserved. The trade-off is long simulation time when simulating high Q-factor modes (i.e. sharp frequency variations). Figure 3.1 illustrates the flowchart of a FDTD simulation.
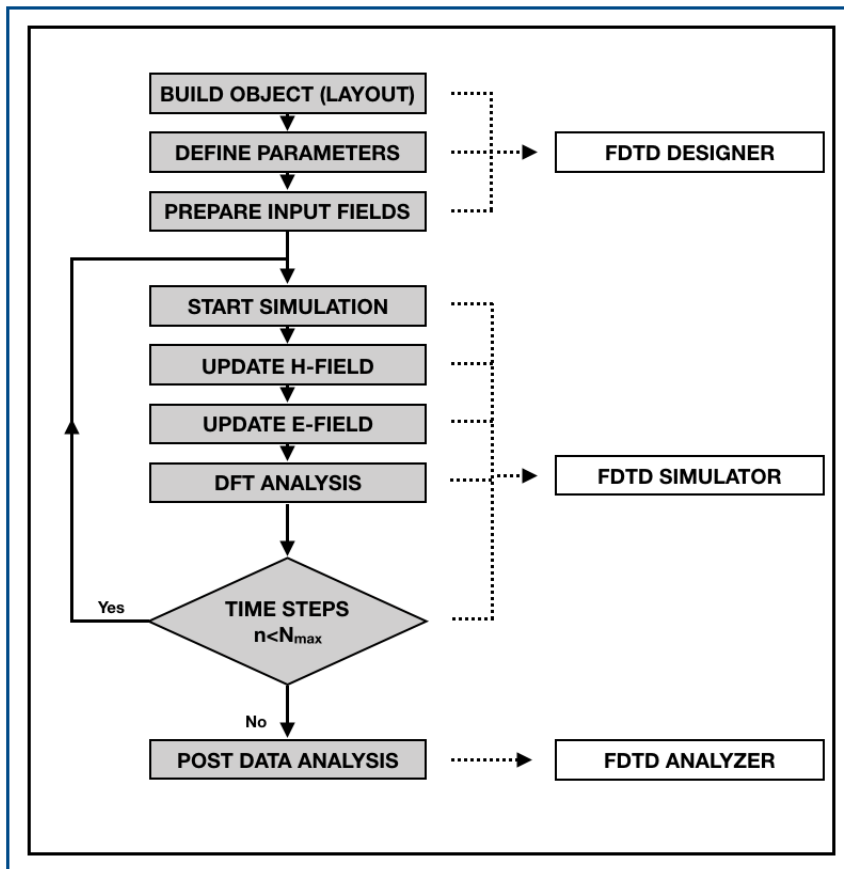
Figure 3.1: Flowchart of the algorithm behind FDTD. FDTD can be divided into three sections: Designer, Simulator, and Analyzer. The Designer sets up the necessities to run a simulation. Simulator iterates through ME at each pixel for as long as defined in designer. Before the software checks if N_{max} is reached a discrete Fourier transform (DFT) analyses and saves frequency information collected from the simulation space. When N_{max} is reached the FDTD program moves on to the post data analyzer. The analyzer returns the data of interest from a point, line, surface, or volume defined in designer.

Referring to Figure 3.1, the FDTD Designer involves setting up the simulation space, defining initial- and boundary conditions, and defining the resolution of the simulation space. When the FDTD Simulator is started, ME is calculated at the boundary of each calculation cell (decided by the defined resolution). Figure 3.2 illustrates how a Yee-cell operates and conversely how the "update H field" and "update E field" steps of Figure 3.1 are executed. Frequency information from the simulation space is analyzed by the DFT analyzer.
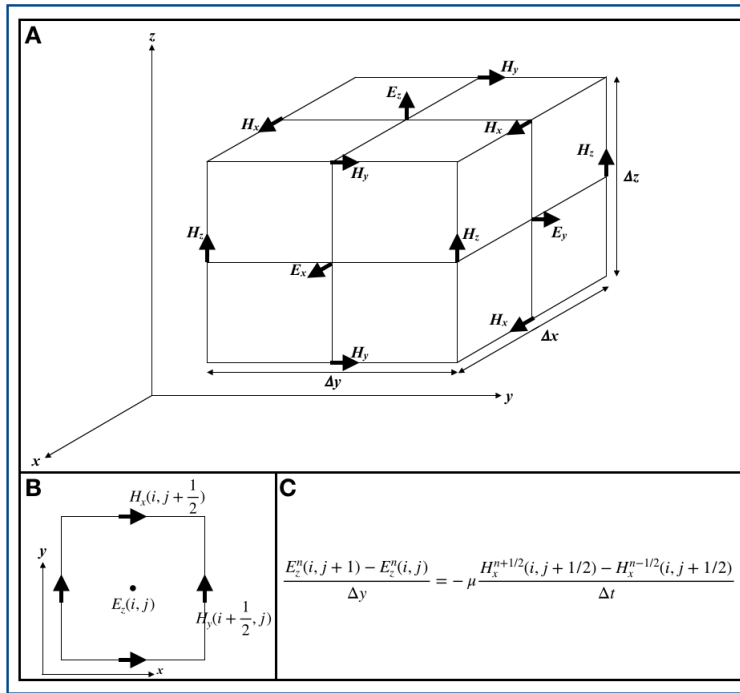
Figure 3.2: Illustration of a cubic Yee-cell (**A**), a two-dimensional Yee-cell (**B**), and how ME are calculated at the cell boundary (**C**). The Yee-cell is defined in FDTD Designer (see Figure 3.1), usually by the user in terms of dimension and resolution. The computation of ME as illustrated in Figures **A**, **B**, and **C** is a good description of steps "UPDATE H-FIELD" and "UPDATE E-FIELD" in the FDTD Simulator of Figure 3.1.

By considering Figure 3.2 A, choosing a resolution that captures a satisfactory amount of information but also allows for reasonable computational time becomes evident. The fact that two-dimensional simulations are faster than three-dimensional also becomes evident. Figure 3.2 C is the ME to be solved for the top horizontal boundary of the Yee-cell in B. The FDTD Simulation stops simulating either on a time requirement or an intensity requirement at a certain point in the simulation space. The FDTD Analyzer analyzes the raw data from the simulation cells according to scripted instructions. The output analysis can for example be transmittance and reflectance spectra, resonant modes and frequencies, or field patterns [1][51]. In Appendix B a python script for transmission spectrum for a chosen ring resonator design is commented with "FDTD designer", "FDTD simulator", and "FDTD analyzer" to relate the flowchart in Figure 3.1 to an actual simulation script.

3.2   Fabrication

Fabrication of photonic crystals (PC) is usually performed in a cleanroom facility. Four inch silicon wafers, predeposited with silicon dioxide (SiO2, silica) are commercially available. Plasma Enhanced Chemical Vapor Deposition (PECVD) is a technique performed to deposit a given thin film on top of any sample or wafer. For the LOC project PECVD is used to deposit amorphous-Silicon (a-Si) on top of the silica covered silicon wafer. In order to produce photonic crystals designed for infra-red applications a high lithography resolution is required. Electron beam lithography (EBL) meets the resolution requirements and is therefore the common lithography technique. For smaller lithographic work, such as inverted tapers a mask less aligner (MLA) is used. The pattern created by the EBL must in some way result in a structural pattern in the sample or wafer. the lithographic work specific for this thesis work involving MLA does not require etching (explained in Chapter 4). Transferring the EBL pattern to a structural pattern in the sample is done by etching. Inductively Coupled Plasma-Reactive Ion Etching (ICP-RIE) is the common etching technique for photonic crystals. The three process techniques, PECVD, EBL, MLA, and ICP-RIE are described in detail in the following subsections. Some introductory knowledge of these process techniques is valuable to understand fabrication trade-offs and limitations.

3.2.1   Plasma Enhanced Chemical Vapor Deposition

Plasma Enhanced Chemical Vapor Deposition (PECVD) is a process technique where the end result is to deposit a solid-state thin film on a substrate. The thin film can range from single atomic layer to a few microns in thickness [53]. The thin film is produced by combining a certain combination of elements in a gaseous state. The gaseous combination of elements, known as precursor gases react in a plasma created by a radio frequency (RF) source. A plasma is an ionized gaseous substance. The applied RF is responsible for ionizing the precursor gases. The RF is applied between two parallel electrodes. The capacitive coupling between the electrodes excites the reactant gases into a plasma. The frequency of the RF power depends on the application, with typical frequencies found at 40 kHz, 400 kHz, 13.56 MHz, and 2.45 GHz [53]. The plasma enhancement provides an advantage of lower temperature processing compared with other CVD processes such as low pressure chemical vapor deposition (LPCVD). Typical process temperatures for PECVD range between 200-450°C [53]. In comparison, process temperatures for LPCVD range between 425-900°C. Chemical vapor deposition (CVD) processes must take place under vacuum to avoid creation of side products from the reaction of the ambient components of the precursor gases. The method of operation is illustrated in Figure 3.3.
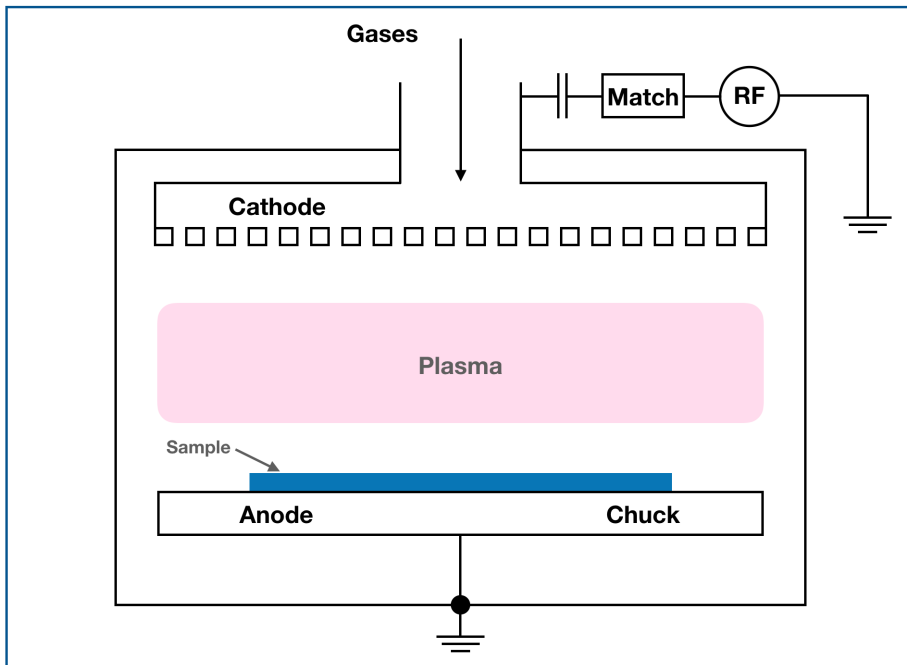
Figure 3.3: Cross-sectional illustration of a PECVD chamber. A combination of gases enters from the top and flows through a perforated metal sheet that acts as a cathode for the radio frequency source. When the gases are localized between the cathode and anode the radio frequency electric field interacts with the gases creating a plasma. The sample is placed on top of the chuck.

Figure 3.3 illustrates a cross-section of a PECVD chamber. A combination of gases enters from the top and flows through a perforated metal sheet that acts as a cathode and electrode for the radio frequency source. The perforated metal sheet also helps to provide a uniform distribution of gas flow across the sample surface. When the gases are localized between the cathode and anode the radio frequency electric field interacts with the gases creating a plasma. The sample is placed on top of the chuck. The chuck acts as the anode and grounded electrode. A DC voltage difference between the electrodes makes sure that the free electrons due to ionization are absorbed at the chuck. The advantages of using plasma during CVD are:

- Lower processing temperature.

- Excellent gap-fill for high aspect ratio gaps (high-density plasma).

- Good film adhesion to the wafer.

- High deposition rates.

- High film density.

- Wide range of applications due to lower processing temperature [53].

To ensure high thin-film quality numerous parameters must be controlled; these include pressure, gas flow, discharge excitation frequency, and power. These parameters affect plasma characteristics such as electron density, electron energy distribution function, and fluxes of different species toward the sample or wafer surface [43]. The reaction rates of the produced plasma is rather complicated, even for relatively simple gas mixtures. For the LOC project a-Si is the only thin-film material deposited using PECVD. High optical performance requires uniformity across the device. Surface roughness and fluctuations in refractive index reduces the performance by introducing scattering loss, internal boundaries that are subject to reflections and path of propagation deflections. Unlike c-Si, which exhibits continuous crystal lattice structure a-Si is absent of long range crystal structure [48]. The lack of crystal lattice structure introduces a higher density of defects. The defects can come in form of dangling bonds, vacancies, and interstitials. For a-Si the simplest defect is coordination defect. A coordination defect introduces mid-gap states, much like a dangling bond. A mid-gap state allows an incoming photon to excite an electron, causing loss in some form. In pure a-Si the density of these defects can be 10^{19}cm^{-3} and upwards [48]. Such a high density of defects make the amorphous thin-film a lossy material for waveguide purposes. By introducing hydrogen as one of the precursor gases a large amount of the coordination defects can be passivated. introducing hydrogen can reduce the density of mid-gap states from 10^{19}cm^{-3} to $10^{15} - 10^{16}\text{cm}^{-3}$ [48]. A reduction of three to four orders of magnitude manifests itself in ridge waveguides for infra-red purposes with propagation losses of less than 2dB/cm [61].
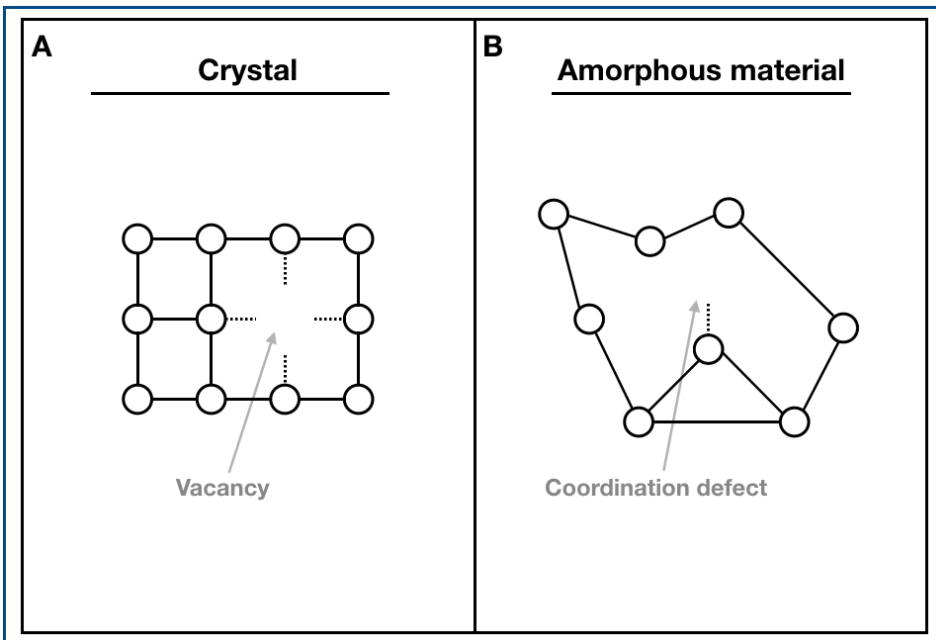
Figure 3.4: Illustration of defects in Silicon. Figure **A** illustrates c-Si and its simplest defect, vacancy. Figure **B** illustrates a-Si and its simplest defect, coordination defect.

3.2.2 Electron Beam Lithography

Electron beam lithography (EBL) is a process technique that imprints a custom pattern on an electron-sensitive surface. The electron-sensitive surface is called resist. A resist usually consists of organic polymer materials and can either be positive or negative depending on its chemical response to electron exposure. A negative resist creates polymer cross-linking when exposed to an electron beam. When polymers cross-link the resist becomes less soluble. A positive resist experiences polymer bond breaking when exposed to an electron beam [36]. The exposed area becomes soluble relative to the unexposed resist. The solubility differences within the resist is later exploited when developed. The sensitivity of a resist affects the end resolution of the lithographic process. The sensitivity is the dose (electron beam dose) per area needed for sufficient exposure. The sensitivity depends on factors such as resist material, the spatial thickness of the resist, the substrate material, and which developer is used and how the development is performed. Figure 3.5 illustrates the logical difference between positive and negative resist.
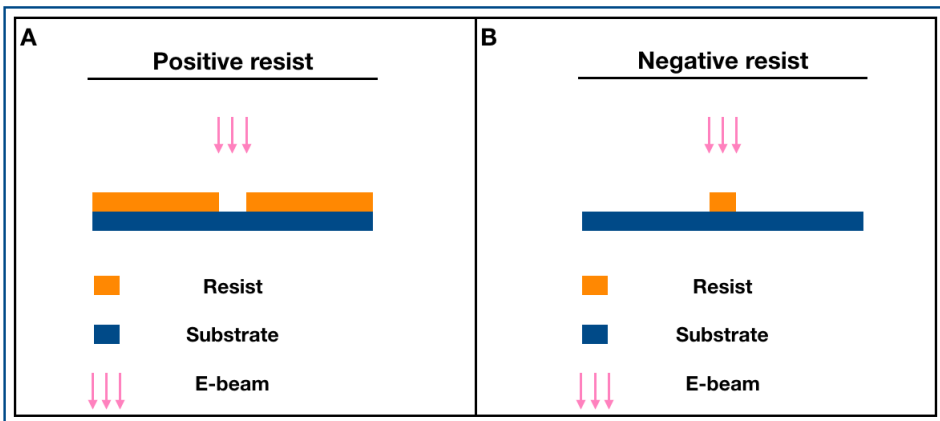
Figure 3.5: Illustration of the logical differences between positive (**A**) and negative (**B**) resist after development. Positive resist becomes more soluble when exposed to an electron beam. Negative resist becomes less soluble when exposed to an electron beam.

Figure 3.6 is a schematic cross-section of an EBL chamber with external connections to computer and pattern generator.
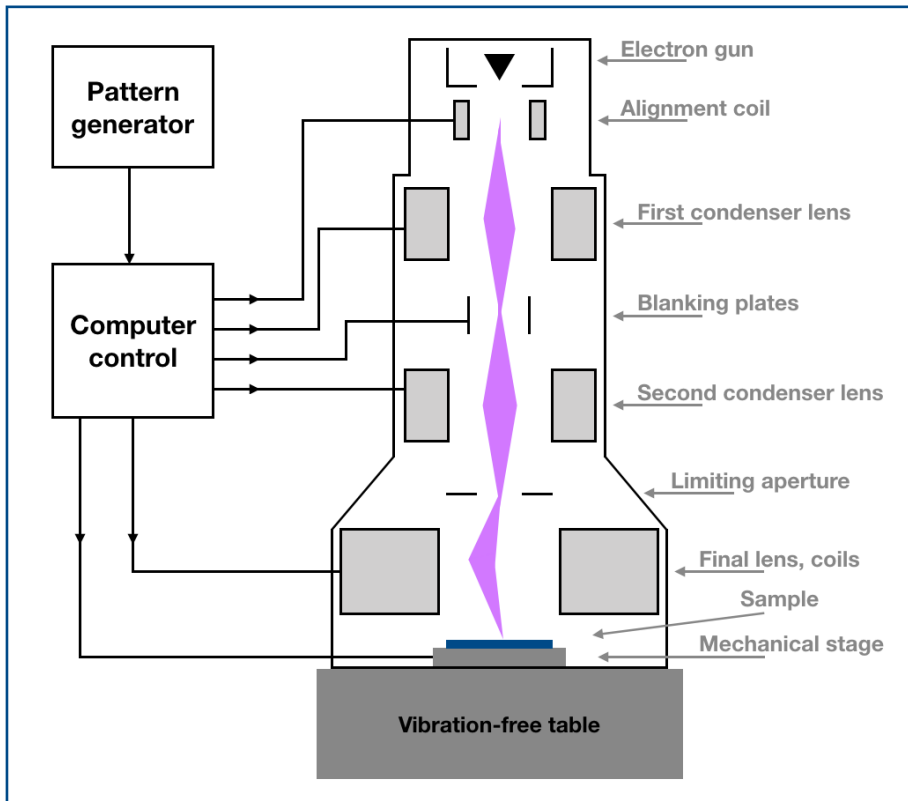
Figure 3.6: Schematic cross-section of an EBL column with external connections to computer and pattern generator. An EBL consists of several condenser lenses, an electron gun, coils for alignment and lenses, a mechanical stage, blanking plates, and a limiting aperture. The EBL is externally controlled from a computer. The pattern that is to be imprinted is designed in computer software of choice. The instrument itself is sensitive to external vibrations and is therefore placed on a vibration-free surface.

An EBL takes a graphic database system (GDS) file as input to the pattern generator. GDS files is the integrated circuit (IC) industry file format standard for IC layout artwork. From a GDS file the EBL is able to interpret beam current, write time, and where to expose. An EBL is equipped with several condenser lenses. They are either magnetic or electro-static. Magnetic lenses usually experience less aberrations compared to electrostatic lenses [24]. In general, magnetic and electrostatic lenses are not as good as optical lenses [24]. The two types of aberrations that are predominant for EBL are spherical and chromatic aberration. Spherical aberration is when the outer zones of the lens focus more strongly than the inner zones. Chromatic aberration captures when electrons of slightly different energies get focused at different image planes. Both types of aberrations can be reduced

by minimizing the convergence angle of the system so that electrons are confined to the center of the lenses. The trade-off is greatly reduced beam current. Apertures are small slits or holes which the beam passes through. Blanking plates is a form of aperture that turns the beam on and off. They are used when the stage is being moved. Alignment coils are used to align the beam. Together with all the other lenses they ensure that the electron beam reaching the sample is uniform and centered at the desired location. Alignment coils also prevent astigmatism. Astigmatism is when the cross-sectional shape of the electron beam becomes elliptical. The desired shape is circular. An oval beam shape results in a smeared image in the resist. The mechanical stage is moved in accordance with assigned write fields and move each time the write field is changed. Write fields are produced by the pattern generator (see Figure 3.6) based on the GDS file input. The lithographic process for an EBL is serial which implies that the mechanical stage moves each time the imprint within a write field is completed. The final lens controls the final movement within the current write field.

Because of the serial nature of an EBL, electron beam write time is important. Electron beam write time is the minimum time to expose a given area for a given dose, and is expressed in Equation 3.1.

$$T = \frac{D \cdot A}{I} \tag{3.1}$$

T is the write time, D, A, and I are the dose, exposed area, and beam current, respectively. The dose, D is related to the resist sensitivity, where the intention is to select a dose that equals the sensitivity. If the area subject to exposure is 1 cm^2, the dose equalling the sensitivity of a typical EBL resist of 172 μC/cm^2 (for CSAR62) [19], and beam current of 1 nA the write time would be almost 48 hours. There is also time consumption associated with moving the mechanical stage and blanking, beam corrections that are not accounted for by electron beam write time.

Limiting resolution mechanisms are several and rise from both the resist/developer used and from the EBL instrument itself. The EBL column consists of several lenses, alignment coils, and apertures that if not used correctly or installed incorrectly will lead to a worsened resolution. Aberrations as mentioned above are a limiting factor for the magnetic and electrostatic lenses. Astigmatism is also a limiting factor related to the EBL instrument [36]. Stitching errors can occur when the mechanical stage is moved. They become evident as overlap or mismatch in write fields. The chemical composition of the resist affects the resolution. The chemical composition is, for the scope of this thesis gathered in the term sensitivity. If the dose factor used does not match the resist sensitivity the exposed resist profile may aberrate. Figure 3.7 illustrates the impact of unmatched dose factor for positive resist. The impact becomes evident first after developing, the beam (pink) is added to illustrate where the sample has been exposed.
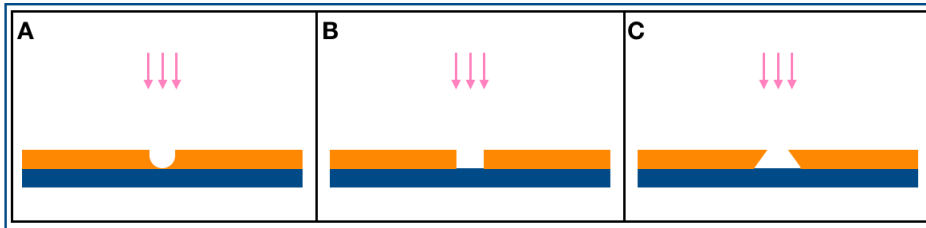
Figure 3.7: Illustration of unmatched dose factor for positive resist. Figure **A** illustrates the effect of development on resist that has been exposed to a dose smaller than the sensitivity. Figure **B** illustrates the effect of development on resist with perfectly matched dose and sensitivity. Figure **C** illustrates the effect of development on resist that has been exposed to a dose larger than the sensitivity.

One of the main limiting factors is forward scattering of electrons in the resist [24]. Figure 3.8 is a Monte-Carlo simulation of the interaction of an electron beam with a resist coated sample [52]. The Monte-Carlo simulation illustrates how the electron beam imprint broadens within the resist.
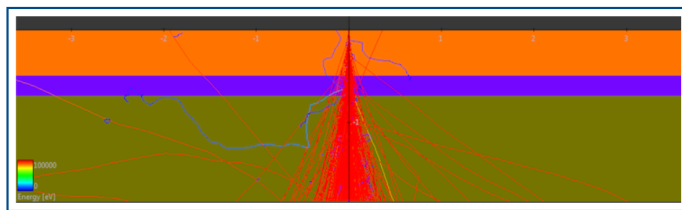
Figure 3.8: Monte-Carlo simulation of the electron beam interacting with a sample. The sample consists of a 490 nm thick resist layer (orange), 220 nm thick silicon layer (purple), and a 2 μm thick silica layer (green). The beam color indicates energy of the traced electron, red is high energy (100kV) and blue is low energy (¡5kV).

EBL resolution is about an order of magnitude smaller than that of conventional optical lithography [9]. Ultimate lithographic resolution is not limited by electron optics, but rather the electron beam's interaction with the resist layer. When the electron beam interacts with the resist, electrons scatter and cause secondary processes to occur (see Figure 3.8. Secondary processes are processes due to ionization products, and are called secondary because they are generated by other radiation than the main source itself. From Figure 3.8 it is evident that the lithographic imprint broadens with sample depth. The ultimate lithographic resolution is typically in the range of a few nanometers, depending on the energy of the electrons and the resist that is used [24]. The drawback with EBL is the relative long time it takes to perform the lithographic process compared to other forms of lithography [53]. The time consumption mainly comes from the need to divide the sample into write fields and then scan each field serially. Due to time considerations EBL is mostly used when resolution is of importance and in research.

3.2.3   Mask Less Aligner

A mask less aligner (MLA) is a direct laser write tool. It performs the lithography with out any aid from a photomask. Lithography has traditionally been performed using a photomask that block light in certain areas, transferring a specific pattern to a photo resist. A mask less aligner uses a precise beam to transfer the pattern to the photo resist. The beam is scanned across the sample to produce the pattern. Performing a mask less aligned lithography process is more time-consuming than using a photomask. The advantage with MLA is its flexibility in changing lithography patterns from one run to the next, without the cost of a new photomask. Feature size of 9 nm has been reported produced using MLA [18]. A mask less aligner often exhibits more than one laser source, predominantly in the visible and UV range. As with the EBL a mask less aligner accepts GDS files as input.

3.2.4   Inductively Coupled Plasma-Reactive Ion Etching

Inductively coupled plasma-reactive ion etching (ICP-RIE) is a dry etch accommodated by a radio frequency (RF) source that generates a plasma [53]. There are general differences between dry and its counterpart, wet etch. A dry etch is known as a plasma-phase etch, while a wet etch is known as liquid-phase etch. The benefit of performing a dry-etch over a wet-etch is:

- Easier to control.

- Capable of defining small features below 100 nm [REF].

- Can produce high anisotropy.

- Reduced material consumption.

ICP-RIE is an etching method that is flexible and has a high degree of controllability. The induced plasma allows the trade-off between reactive etching and physical etching to be controlled. The inner workings of the plasmas are quite complicated. Optimized etching processes are therefore usually found empirically. Figure 3.9 is a cross-sectional illustration of an ICP-RIE chamber.
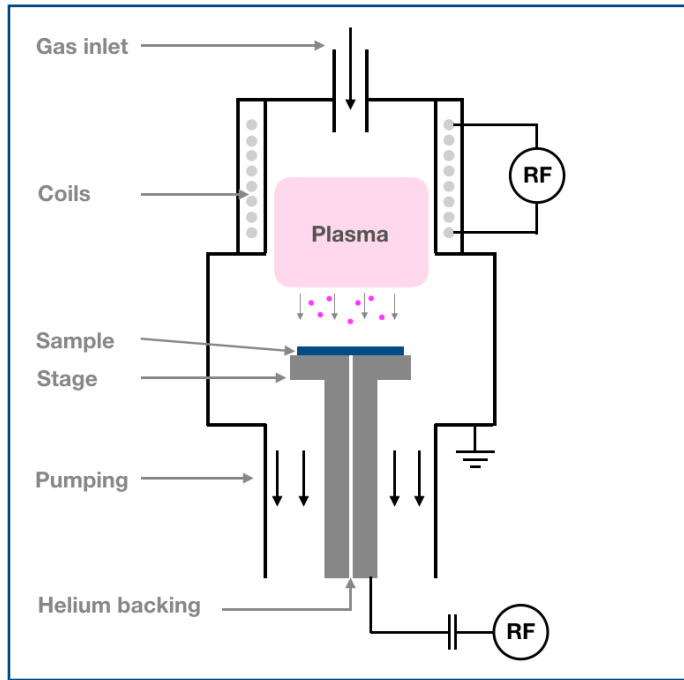
Figure 3.9: Cross-sectional illustration of an ICP-RIE chamber. A gas inlet allows for reactant gases to flow into the chamber. Metal coils surround the chamber creating a RF magnetic field within the chamber. The magnetic field inductively couples to the reactant gases creating a plasma. The RF source connected to the stage is responsible for accelerating the plasma particles to the sample. The RF source connected to the stage capacitively couples to the plasma. A pumping system assures that vacuum conditions are maintained.

The ICP-RIE has a gas inlet that allows reactant gases to flow into the chamber. In an ICP-RIE there are two RF sources connected to the instrument. One is connected to a coil surrounding the chamber creating a magnetic field that inductively couples to the reactant gases. The other RF source is connected to the stage and capacitively couples to the reactant gases. The chamber walls are grounded. Electrons that are detached due to the electric and magnetic fields are mainly absorbed by the grounded sidewalls. The gas-molecules are too heavy to be affected by the alternating fields. When a sufficient amount of electrons have been absorbed by the chamber walls a DC voltage tends to build up between the stage/sample-surface and plasma. The DC voltage is responsible for accelerating the plasma ions towards the sample surface. Depending on the DC voltage build-up the ions predominantly sputter or react with the sample surface. A higher DC voltage build-up increases the amount of sputtering [57]. A pumping system maintains vacuum condition within the chamber. The pressure is conventionally held very low, in the mTorr range.

Figures of merit to describe the ICP-RIE process are:

- *Etch rate:* A given distance etched for a certain time.

- *Uniformity:* Equal etch rates across the surface for identical materials.

- *Selectivity:* Ability to only etch the desired material.

- *Anisotropy:* Verticality of etch profile [57].

These figures of merit are sufficient to describe a successful etch. How each of the four factors are controlled for a successful etch is rather complicated. Etch rate can be controlled by the DC voltage and pressure (presence of gas molecules). Uniformity is more dependent on the gas molecules that are being used and their reaction process with the substrate to be etched. Selectivity is chemically influenced and controlled by the reactant gases, substrate to be etched, and applying a resist that does not interact with the etching ions. Anisotropy can be controlled by the DC voltage. A high DC voltage manifests itself in more physical bombardment of the ions [57]. Physical bombardment generates an anisotropic etch. If the material to be etched is anisotropic in nature chemical anisotropic etching can be possible. Table 4.5 illustrates each factor or figure of merit.

Table 3.1: Table illustrating the figures of merit. Yellow and blue colors are identical to Figures 3.5 and 3.7 illustrating resist and substrate, grey color illustrates part of substrate that is not intended to be etched. Column **A** is the figure of merit, column **B** illustrates the ideal etch case and is identical for each row, and column **C** illustrates a poor etch case due to the respective figure of merit.

The etch rate is important to know precisely, otherwise under-etching or over-etching can occur. An under-etched slab waveguide would not confine light nearly as good as a properly etched waveguide since the geometry would be totally changed if under-etched. Uniformity in etch rate is important for the same reasons as etch rate itself. Selectivity is important when several materials are involved and geometrical details are important. Again, if a slab waveguide is etched with a resist and waveguide material that do not offer good selectivity, the etching process would etch away some of the resist before etching waveguide material that was not intended to be etched. Anisotropy is a measure that compares the etch rate in one direction to the etch rate in the plane perpendicular to that direction. Typically the direction of interest is the vertical axis and the plane perpendicular to the vertical axis would be the surface plane of the sample or wafer. Anisotropic etching is important when fabricating photonic crystals. The inclination of ring side walls affects the dispersion relation as well as transmission/reflectance values at each hole/substrate interface.

3.3 Characterization

Produced structures are usually characterized using some profilometer or microscope. A scanning electron microscope (SEM) is extensively used in the LOC project for characterization. A laser setup to perform transmission testing of the devices is also used. The theoretical understanding of such a setup is briefly described below.

3.3.1 Scanning Electron Microscope

In a scanning electron microscope (SEM) an image is produced by scanning the sample surface with a focused electron beam. The electron beam interacts with atoms in the sample creating various signals with information about the sample's topography. The different types of signals created in a SEM are summarized in Figure 3.10.
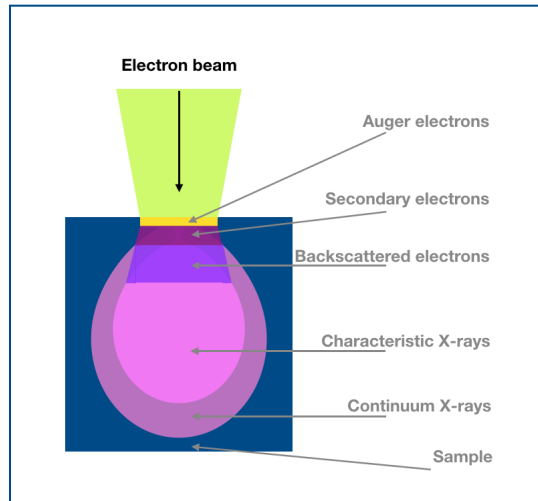
Figure 3.10: Illustration of the different electron/sample interactions and their interaction volumes.

It is typical for a SEM to have detectors for secondary electrons (SE). SE detectors can often have 1 nm resolution since the SE scatter when interacting with atoms close to the sample surface. SE are low energy electrons (>50eV). They eject from either the valence or conduction band of the sample atoms by inelastic scattering interaction with the electron beam electrons. Their low energy corresponds to originating from only a few nanometers below the sample surface. The SE electrons are detected by a Everhart-Thornley detector. An amplifier is mounted in the detector allowing the signals from SE to be visualized on a monitor. Backscattered electrons (BSE) scatter from deeper in the sample. The resolution from BSE is therefore less than for SE and the BSE also exhibits more energy. BSE scattering is predominantly elastic scattering. BSE intensity depends strongly on the atoms they have interacted with. Heavy atoms (high atomic number Z) backscatter electrons more strongly than light atoms (low atomic number Z). The scattering dependency on interacted material gives information about material distributions within the sample. Sensors dedicated to detect BSE are positioned in a doughnut shape above the sample. Strong topographical contrast is produced by collecting back-scattered electrons from one side above the sample, using an asymmetrical directional BSE detector; the resulting contrast appears as illumination of the topography from that side.

Figure 3.11 is a cross-sectional illustration of a SEM column.
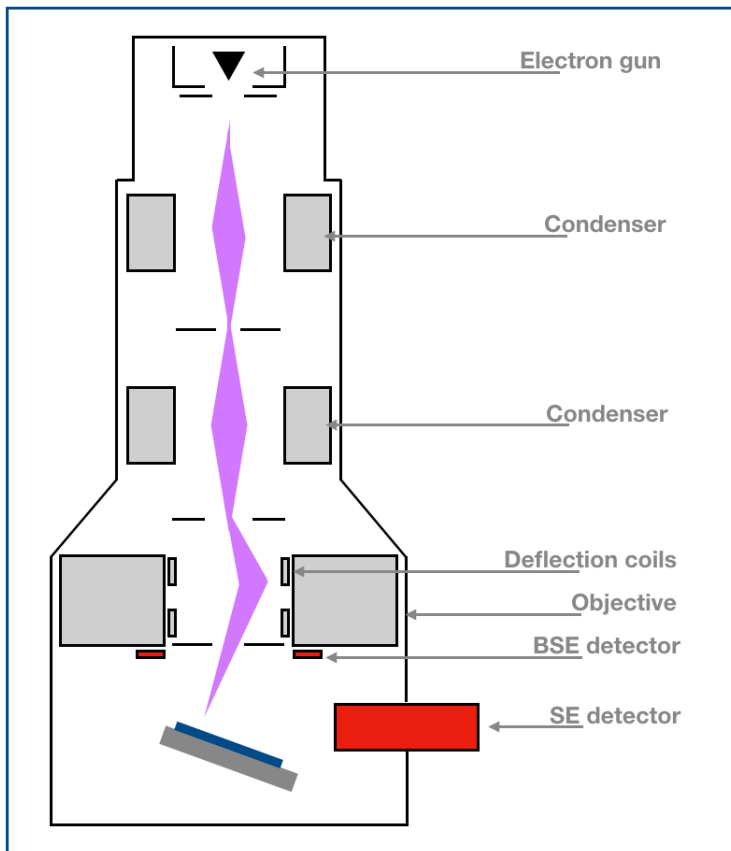
Figure 3.11: Cross-sectional illustration of a SEM. An electron gun is mounted above the sample stage. Between the sample stage and the electron gun the electron beam passes by a set of condenser lenses, deflection coils, apertures, and detectors. Unlike the EBL, a SEM's objective is to collect information about the electrons interaction with the sample. For that reason a SEM is mounted with back scattered electron (BSE) detector and secondary electron (SE) detector.

SEM imaging is performed under vacuum conditions. The sample is placed on a stub often supported by adhesive tape. Some SEMs can tilt and rotate the stage 45 degrees and 360 degrees, respectively. Above the sample stage rises a column containing an electron gun and devices guiding the electron beam down to the sample. A SEM column shares some similarities with the EBL column (see SubSection 3.2.2). The electron gun is mounted on the top of the column. It accelerates electrons to energies ranging from 1 keV to 30 keV. Between the sample and electron gun the column is equipped with a number of magnetic lenses and apertures. The magnetic lenses are similar to that of the EBL. Deflection coils deflect the electron beam when interaction with the sample is unwanted. Unlike an optical system, the resolution in a SEM is not limited by the diffraction limit,

lenses-, mirrors-, or detector array resolution. The spatial resolution of the SEM depends on electron beam spot size. The electron beam spot size depends on the electron wavelength and the electron-optical system producing the scanning beam. Aberrations in the magnetic lenses are an issue for a SEM, just like the EBL. Unlike a scanning tunneling microscope, imaging individual atoms is not possible with a SEM. For that the spot size and the interaction depth (into the sample) is too big in area and volume, respectively. The resolution in a SEM can come down to 1 nm under the right conditions.

4. Experimental Procedure

This chapter is included in the thesis as an explanation to the reader of every step that goes in to producing a photonic crystal ring resonator (PCRR). The steps are put forth in a chronological order, starting with simulations and ending with characterization. The intention from the author is to explain everything to such a detail that the reader can reproduce the experimental procedure. For the simulation section the reader may be referred to appendix (simulation code) or the software documents for information about the inner workings of the simulation [1][2][51][32]. The thesis covers what the simulation code accomplishes and why it has been done. For the fabrication procedure every step is explained by mentioning all its parameters for reproduction purposes.
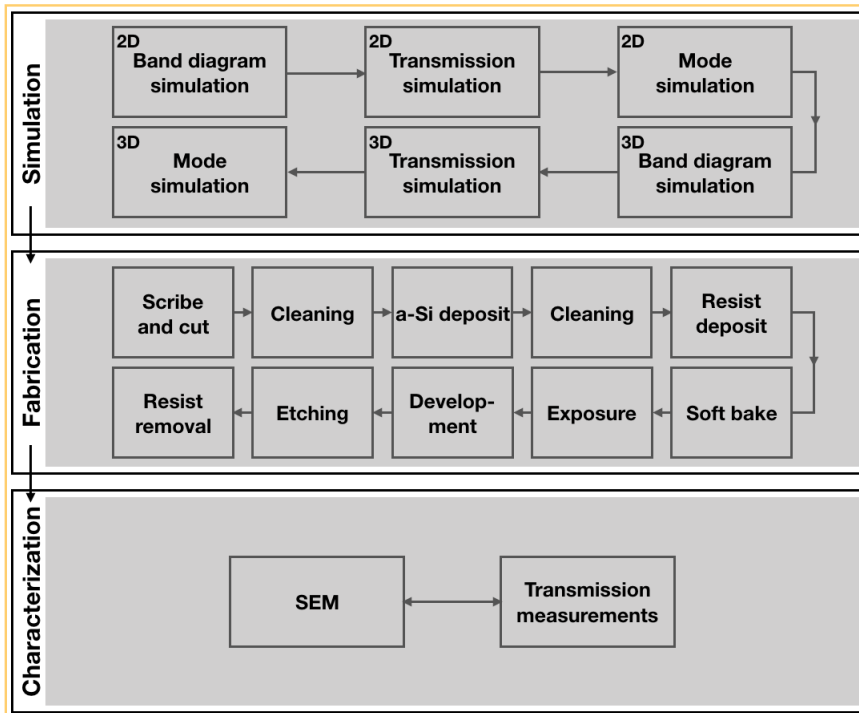
Figure 4.1: Schematic illustration for the experimental procedure of producing PCRRs.

Figure 4.1 is a schematic illustration of the experimental procedure. Just as the following sections the figure is divided into simulation, fabrication, and characterization. The fabrication part of Figure 4.1 renders all the fabrication steps to fabricate an ordinary PCRR. Extraordinary steps, associated with waveguide tapering and under-etching are not included in the figure.

4.1 Simulations

Simulations are performed as illustrated in Figure 4.1. Band-diagrams for intrinsic two-dimensional PC along all high-symmetry directions is calculated. PC with line defect band-diagrams and slab waveguides are calculated along the $\Gamma - K'$ symmetry direction (see Figure 2.11, Chapter 2), the same direction as the line defect itself. All band-diagram simulations are performed using MPB. Transmission simulations of PCRRs are performed using Meep. Band diagrams for intrinsic PC, line defects, and slab waveguides are all performed because they are all environments that light has to interact with on its way from an external source to an external detector.

Transmission simulations are useful as validation for band-diagram calculations and vice-versa. In addition to validation transmission simulations offer information about modes within the band-gap. Finally, mode simulations are performed using Meep. The source bandwidth is narrower for mode simulations than for transmission simulations, and the center frequency is set to coincide with the appearing modes from the transmission simulations. The procedure is identical for three-dimensional simulations. The procedure will be explained for an ordinary PCRR. After the procedure is explained, all the design solution will be introduced. The procedure is identical for all design solutions.

All simulations are scaled to a lattice constant of unity. The convenient way of doing so is to relate all variables to the lattice constant. Some geometrical consideration apply for all simulations. They are listed in Table 4.1.

Parameter	Dimensionless value	Physical value
a	1	420nm
r	0.3a	126nm
h	0.55a	231nm

Table 4.1: Geometrical considerations that apply for all simulations. Every parameter is scaled with the lattice constant a. a is set to unity in simulations and is linked to an IR-source centered at 1550nm through its physical value of 420nm. r is the hole radius of a normal PC air-hole (i.e. not a hole specific for a design solution). h is the height of the PC layer. Both r and h are set to center a wavelength of 1550nm within a PC bandgap.

4.1.1 Band Diagrams

The band diagrams are calculated using MPB. MPB solves the Master Equation 2.23 in frequency domain and returns data points for the amount of dispersion bands and wavevector points given as input from the user. The calculations are set up as a user written python script (see Appendix [MPB]). The MPB-script includes certain key features that are essential for a successful simulation:

- Number of spatial dimensions.

- Computational cell.

- Geometric structure with defined permittivity.

- Number of dispersion bands to compute.

- Resolution.

- Boundary conditions.

- Number of wavevector points for which to compute the dispersion relation $\omega(k)$.

A computational cell defines the size of the simulation domain. The geometry for which to compute the bands is essential as permittivity input to the Master Equation. How many dispersion bands to compute determines the amount of data points that are returned. In most PC designs the structure is designed to operate (with regard to frequency) within the ten first bands of the design. The number of dimensions should correspond to the computational cell and the defined geometric structure. The resolution can be divided into different resolutions along each individual axis. The resolution is set to $a/32$ for in-plane directions, and $a/16$ for the vertical axis. Boundary conditions for MPB computations are periodical. The number of wavevector points to calculate for is set to 200. The calculation itself is initiated by a run-command [2].

Band-Diagram For Intrinsic PC
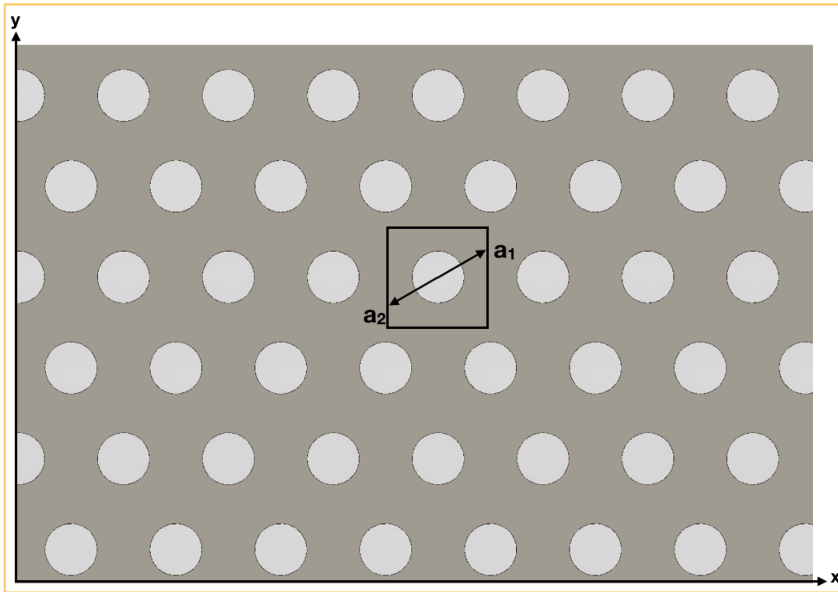
Figure 4.2: Hexagonal photonic crystal with no defects or symmetry interrupts except for not extending to infinity. Black square represents the computational cell. a_1 and a_2 are the basis vectors assuring that the periodic boundary condition mimic a triangular lattice instead of a square lattice.

The band-diagram is computed for a PC with hexagonal rotational symmetry. MPB is the software used for simulating the band-diagram. Figure 4.2 illustrates the structure and simulation space used. The structure and simulation space are either two-dimensional or three-dimensional. The defined structure is only as large as the computational cell, illustrated in Figure 4.2 with a black square. The boundary conditions for the simulation is set to assume periodicity along two predefined axis. For triangular air-hole PC the predefined axis are: $a_1 = [\frac{\sqrt{3}}{2}, \frac{1}{2}]$ and $a_2 = [\frac{\sqrt{3}}{2}, -\frac{1}{2}]$. Under the assumption that the structure extends to infinity the simulated structure becomes a valid representation for the larger PC

illustrated in Figure 4.2. The wavevector points calculated are located along the irreducible Brillouin zone proximity. The simulation solves the Master Equation 2.23 for a specified number of frequency bands. The permittivity (i.e. geometric structure) that goes in to the Master Equation is determined by the wavevector point that is evaluated. The initiating run command of the MPB-script starts the calculation of the structures dispersion relation. The resulting data points from the simulations are collected and graphically represented as diagrams or graphs in Chapter 5.

Band-Diagram For Line Defect

When calculating the bands for a line defect, a structure identical to that illustrated in Figure 4.3 is defined.
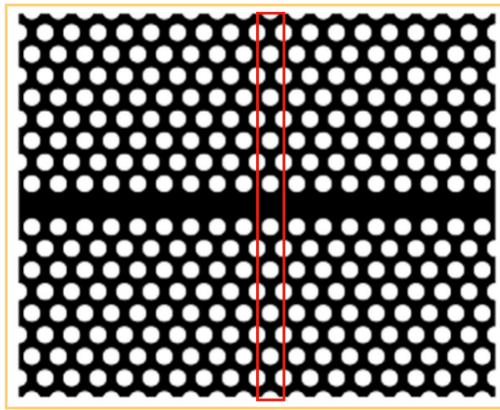
Figure 4.3: Illustration of the structure created when calculating the bands for a line defect in triangular PC. The red rectangle represent the simulation cell. The Master Equation is solved for wavevectors along the line defect. It is sufficient to compute for the wavevectors from Γ to K'. Γ is located in the center of the computational cell, K' at each end of the computational cell and within the line defect.

The translational symmetry is only conserved in the x-direction when introducing the line defect. Only the wavevector components parallel to the line defect are calculated, in this case k_x along the x-axis from lattice point Γ to K'. K' is located on the edge of the reciprocal lattice, or at the center of each vertical line of the computational cell of Figure 4.3. The line-defect is constructed by increasing the geometric structure (compared to intrinsic PC) along the y-axis and removing an air-hole. The boundary condition is only periodic in the x-axis, thus representing the structure beyond the simulation cell in Figure 4.3. The initiating run function is set to find TE and TM modes satisfying the Master Equation 2.23. The intention with performing a line defect simulation is to identify the guided modes (i.e. additional dispersion modes) introduced by the line-defect itself. The guided modes for a line defect are of interest because PC line defects couple to both the PCRRs and to slab waveguides.

Band-Diagram For Slab Waveguide

When calculating the bands for a slab waveguide, a structure identical to that illustrated in Figure 5.6 is defined.
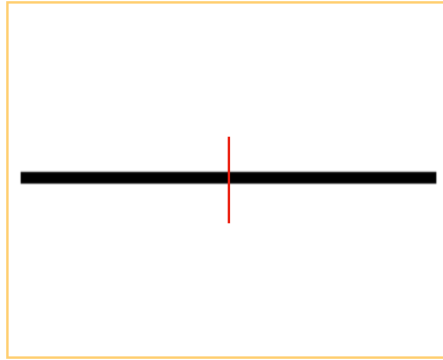
Figure 4.4: Illustration of the structure created when calculating the bands for a slab waveguide. The Red line illustrates the computational cell, in this case two-dimensional. The Master Equation is solved for wavevectors along the line defect. Same as for the line defect in Figure 4.3.

Only the wavevector components parallel to the slab waveguide are calculated, in this case k_x along the $\Gamma - K'$ symmetry direction (same as for line-defect, see Figure 4.3). There are no permittivity variations along the slab waveguide, and therefor the computational cell does not need to extend along the waveguide. The guided modes for a slab waveguide are of interest because the slab waveguides couple to PC line defects.

4.1.2 Transmission Simulations

The intention of performing a transmission simulation is to observe which frequency components (emitted from a source) couples into the ring resonator. A slab waveguide is introduced and located near the ring resonator. The slab waveguide becomes a line defect within the PC. The line defect couples to the ring resonator. The simulation is set up with a source at one end of the waveguide and a flux detector on the other side of the waveguide, on the opposite side of the ring resonator (see Figure 4.5). The simulation is scripted in a similar manner as the MPB-scripts an run with Meep (script is offered in Appendix B). Transmission simulation solves Maxwell's equations in time domain. The simulation script defines the following parameters:

- Source

- Computational cell

- Permittivity defined structure

- Boundary layer

- Number of dimensions (two or three)

- Resolution

- Symmetries

- Flux regions or planes

The source in this case is a Gaussian electric dipole, polarized along the y-direction (see Figure 4.2). The y-component is the only electric field component capable of coupling to the PCRR. The center frequency of the source is set to a frequency resembling the mid-band-gap frequency of the band diagram (see Figure 5.4). The half maximum bandwidth is set to cover the band-gap. The flux-detector is equally polarized to detect the y-component of the electric field. The permittivity defined structure is illustrated in Figure 4.5. The computational cell is surrounded by the yellow frame of Figure 4.5. A boundary layer is not a visual object but rather a method of dealing with field components at the computational cell proximity. The boundary layer in this case is set to absorb all field components, avoiding reflections that could possibly disturb the flux measurements. Such a boundary condition is known as a perfectly matched layer and essentially extends the computational cell to infinity. Number of dimensions determines the spatial size of the computational cell. Both two and three dimensions are used in this thesis. A resolution of 16 is used in all transmission simulations. The resolution defines the computational cell resolution per unit distance [1]. The unit distance in the simulation is set to unity, resulting in 16 pixels per unit distance. 16 pixels per unit distance has been reported as being the optimum resolution for Meep simulations [37]. Exploiting symmetry is essential for reducing computational time. Whenever the fields and structures in a simulation act symmetrically the symmetry can be predefined in the simulation script. As an example; a mirror symmetry in a simulation can reduce the simulation time by a factor of two. The simulation only needs to be performed for half of the simulation space and later copied

to account for the other half of the simulation space. For the two-dimensional transmission simulation setup there are no symmetry planes. For three-dimensional transmission simulations there exists a mirror symmetry plane in the z-plane whenever the layer above and below the PC layer are identical. Figure 4.5 illustrates the simulation space for a transmission simulation setup.
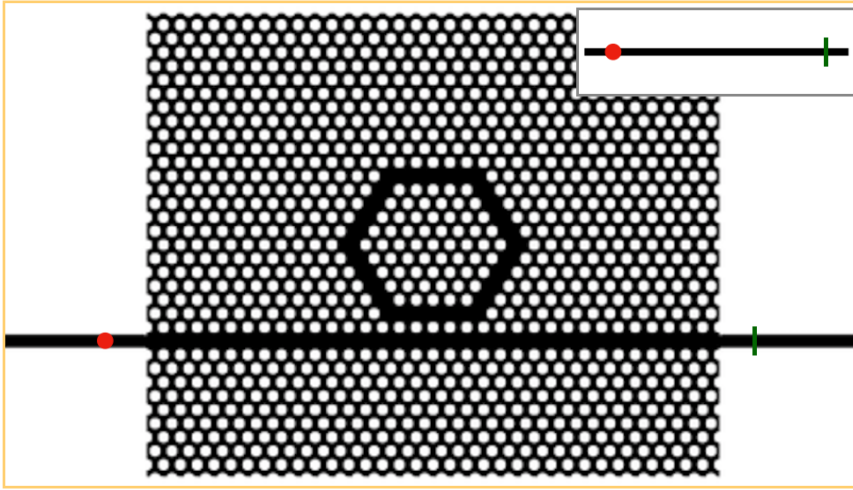
Figure 4.5: Overview of the setup for transmission simulations. Red marker indicates source location and green marker indicates flux detector location. The source is given as a Gaussian source with a large bandwidth. The bandwidth should ideally cover the whole band-gap to be exploited. The flux detector will detect all frequency components that travel straight from the source to the detector. Frequency components that couples to the ring resonator appear as missing frequency components at the flux detector. The flux spectra collected from the transmission simulation is compared to a similar flux spectra collected from a straight waveguide, visualized in the upper right corner. The geometry of the waveguides and the distance from source to flux detector is identical for both structures.

The source in Figure 4.5 is located at the red marker and a flux detector is located at the green marker. The frequency components that are not present at the flux detector are assumed to couple to the ring resonator. The source is a Gaussian source with a large bandwidth. The bandwidth should ideally cover the whole band-gap to be exploited. The flux spectra collected from the transmission simulation is compared to a reference transmission simulation, visualized in the upper right corner of Figure 4.5. The geometry of the reference waveguide, computational cell, source, flux detector size, and distance from source to flux detector for the reference simulation is identical to that of the ring resonator simulations. The appearing band-gap from the transmission simulations are compared to the band-gap from dispersion computations in Subsection 4.1.1 as a sanity check. The reference structure is deliberately designed as a slab waveguide, and not as a PC guided waveguide. A PC guided waveguide identifies band-gaps as well, but support standing-wave modes located at the band-gap edge. The supported standing-wave modes are not of interest and only contribute with noisy frequency components at the band edges.

4.1.3   Mode Simulations

Mode simulations are performed to identify how well the ring resonators confine light. The longer it confines light the higher the q-factor and sensitivity of the structure is. Mode simulations have a setup similar to transmission simulations. The simulation script is similar, and includes almost all of the same parameters. For a mode simulation some of the parameters are tuned differently. The source is a Gaussian magnetic dipole pulse polarized along the z-axis (axis normal to the PC plane). The polarization of the source is changed from the transmission simulations. All TE-modes are of interest when running mode simulations. By applying a magnetic dipole polarized along the z-axis the simulation is assured to excite all TE-modes. Tuning parameter of the source is its full-width-half-maximum (FWHM) (*df* in Appendix C and B in Figure 2.17 Chapter 2). FWHM is usually decreased to fit the mode as well as possible. A smaller FWHM implies that more energy from the source is able to match the mode of resonance. A smaller FWHM creates a more time consuming simulation, according to Kramer-Kronig relation [55]. The flux detector from the transmission simulations is replaced by a harminv detector for mode simulations. Harminv stands for harmonic inversion and applies a filter diagonalization method to determine frequencies, decay constants, amplitudes, and phase of sinusoids [41]. The decay constant is the q-factor. A long lived oscillation or a small decay constant gives a high q-factor. The harminv detector measures the magnetic components normal to the PC-plane (parallel to z-axis). Transverse electric field components are the only interesting electric field components due to the TE band-gap. Transverse electric field components are directly related to magnetic components perpendicular to the PC-plane. Figure 4.6 illustrates the structure defined for a mode simulation
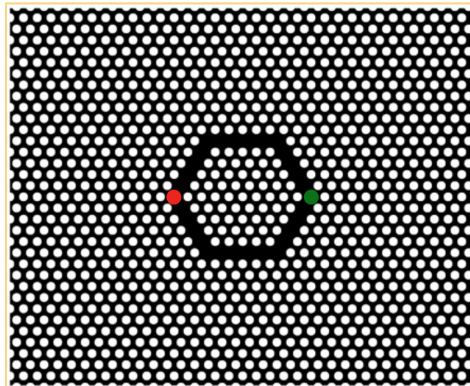
Figure 4.6: Simulation structure for resonant mode simulations. Red marker illustrates source position. Green marker illustrates the position of a harminv detector. A harminv detector detects the damping of a mode (i.e. the q-factor).

Figure 4.6 illustrates a resonant mode structure. The red circle marks the initializing source while the green circle marks a Harminv detector. The source and detector are located as shown in Figure 4.6 to maintain mirror symmetry in the y-plane. The y-plane mirror symmetry effectively reduces the computational time be a factor of two. Symme-

try is exploited in mode simulations. For the two-dimensional simulations there exists a mirror symmetry y-plane. The x-plane mirror symmetry is broken by the positioning of the source. For three-dimensional simulations there exists a z-plane mirror symmetry whenever the material below and above the PC layer are identical. Two mirror symmetry planes reduces the computational time with a factor of four. There are some differences in the proceeding for two-dimensional and three-dimensional mode simulations. They are therefor treated separately below.

Two-Dimensional Mode Simulations

From spectras similar to the one in Figure 5.9 the source is tuned to match resonant modes apparent in the spectras. Generally modes in the band-gap center are preferred modes. A mode can only exist as an evanescent wave outside its mode frequency. A mode far from the band-edge experiences less coupling to the band-edges. At the same time a mode can couple to other modes within the band-gap, thus choosing a mode that appears isolated or far from other modes in frequency can be beneficial. The magnitude of the mode is also important for the resulting Q-factor (see Equation 2.47, Chapter 2); a larger magnitude results in a larger Q-factor. A larger magnitude indicates more power dissipated at the corresponding frequency. The dissipated power is (as mentioned earlier) assumed to couple to the ring resonator. The Q-factor will increase with decreasing FWHM and increasing PC structure size. These two parameters are kept constant across all simulations, providing a simulation setup that substantiates a framework for comparison of various PCRR designs. FWHM is set to 0.005 normalized frequency. A smaller FWHM would provide a higher Q-factor but also increase the simulation time. A normalized frequency of 0.005 is chosen as a trade-off between Q-factor and simulation duration.

Three-Dimensional Mode Simulations

From the spectra originating from a three-dimensional transmission simulation there are few characteristic and sharp modes present from the transmission simulations. Therefor the same proceeding as for two-dimensional simulations cannot be followed. With three-dimensional mode simulations the modes are found by running consecutive mode simulations. For the first mode simulations the FWHM of the source is kept broad, not to exclude any potential modes. The most promising modes identified are pursued in the next mode simulation, now only with a smaller FWHM. This is repeated until the FWHM becomes a 0.005 normalized frequency bandwidth (same bandwidth as for two-dimensional simulations). The three-dimensional simulations are time consuming and therefor run on Fram, the supercomputer hosted by the University in Tromsø. Running the simulations on Fram does not affect the simulation results in any way. It only allows the simulations to complete faster.

4.2 Fabrication

Fabrication is performed in a cleanroom facility at NTNU, provided and run by Norfab. Four inch silicon wafers come predeposited with silica, and six inch wafers come prede-

posited with silica and c-Si. Plasma Enhanced Chemical Vapor Deposition (PECVD) is performed to deposit a layer of amorphous Silicon (a-Si) on top of the silicon dioxide. Electron beam lithography (EBL) patterns the PR with a pattern resembling the desired structure design. Inductively Coupled Plasma-Reactive Ion Etching (ICP-RIE) etches the pattern into the silicon layer and creates the desired structure. In between the steps including the instruments explained in Chapter 3 are several process steps vital for producing SOI photonic crystal ring resonators. All the process steps are covered in the proceeding sections, and are predominantly presented in chronological order. Figure 4.7 is an illustration of all the process steps involved with producing SOI PCRRs with a-Si. As LOC has been an active project since 2014, the overall fabrication procedure is similar to previous thesis-work for the LOC-project [26][25][27].
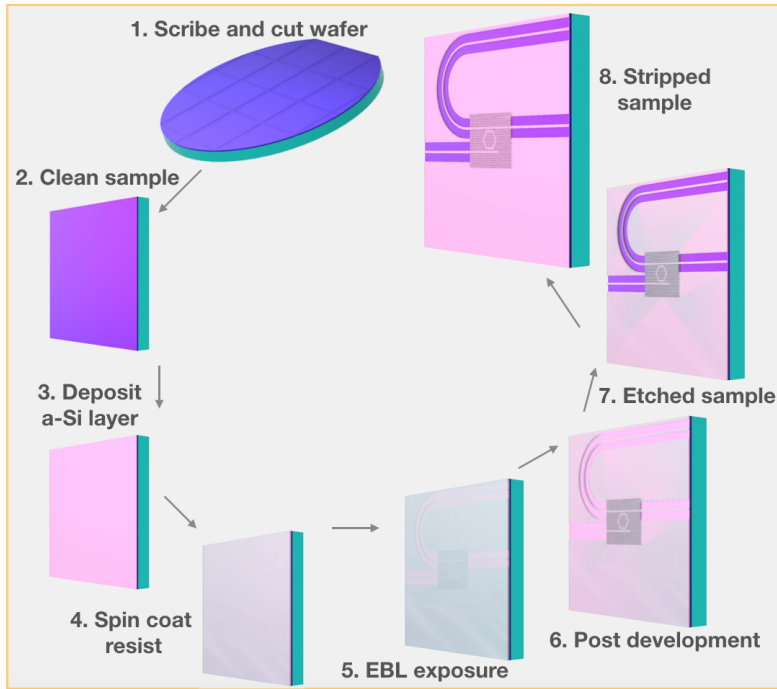
Figure 4.7: Illustration of the process steps involved in fabricating a SOI PCRR with a-Si. Step 1 illustrates a four inch silicon wafer, with a layer of silica on top in the process of scribing and cutting. Step 2 is a sample piece from the four inch wafer. Step 3 illustrates the sample after a layer of a-Si has been deposited. Sample in step 4 is spin coated with resist. Step 5 illustrates the sample after exposure to the EBL. The pattern is barely visible through the resist. Sample in step 6 is a post developed sample. The a-Si layer is now exposed and ready for etching. Sample in step 7 illustrates an etched sample. The resist is stripped from the sample and the end result is illustrated as the sample in step 8.

4.2.1   Sample Preparation

Wafers are delivered as either four or six inch wafers (in diameter). The wafers come pre-coated with a 2μm thick silica layer, or pre-coated with 2μm thick layer of silica and a 220nm layer of c-Si on top. To utilize the wafers in an efficient way they must be divided into smaller pieces. The common method to partition wafers is by scribing and cutting them. The wafers are scribed and cut using Dynatex DX-III. Dynatex DX-III is a combined scriber and breaker. The scriber has a diamond tip that runs over the sample surface making cuts with a maximum channel width of 5μm. The breaking mechanism delivers an exact pressure impact directly below the scribe line. Alternatively the wafers could be scribed and cut by hand which often results in more wafer residue contaminating the sample surface. Step 1 in Figure 4.7 illustrates a wafer in the process of scribing and breaking.

4.2.2   Thin Film Deposition

Before depositing a layer of a-Si the wafers must be cleaned to assure good adhesion between silica and the a-Si layer to be deposited. For c-Si samples deposition is not performed since the wafers come pre-deposited with all the needed layers. The PECVD instrument utilized is an Oxford Instruments Plasmalab System 100 [15].

Cleaning: The samples are cleaned by immersing them in a beaker of acetone followed by a beaker of ethanol, both with a duration of 2 min. The sample is then rinsed with isopropanol (IPA) and dried with N_2 gas. Finally the samples undergo plasma cleaning in a plasma chamber. Sample surface is physically cleaned by ion bombardment, and chemically cleaned by the ionized gas. The instrument is a Diener Electronics Femto. The plasma cleaning parameters are listed in Table 4.2.

Parameter	Amount	Duration
Generator frequency	20 kHz (50%)	1 min
O_2	100 sccm (50%)	1 min

Table 4.2: Plasma cleaning parameters. The percentage indications refers to how the instrument is controlled. Values are set as a percentage of the maximum capacity.

A sample exposed to all the cleaning steps is visualized as step 2 in Figure 4.7.

Deposition: The a-Si films are deposited using recipes with the parameters listed in Table 4.3. The samples are placed on four inch carrier wafers during deposition.

Parameter	a-Si
SiH₄	50 sccm
Ar	150 sccm
Pressure	500 mTorr
LF power	200 W
Temperature	300 °C
Duration	~150 s

Table 4.3: Deposition parameters for a-Si deposition.

An a-Si deposited sample is illustrated as step 3 in Figure 4.7.

Film Thickness Measurements: The thickness of the deposited layer is measured with a reflectometer. The parameters listed in Table 4.3 are tuned to produce a 220 nm thick a-Si layer. Reflectometry is used to validate the deposition process. The reflectometer instrument used is a Filmetrics F20 Tabletop Film Thickness Measurement System. The instrument must be calibrated before each measurement. Calibration is performed by measuring the reflectance of a reference silicon wafer, the sample, and finally the background (nothing placed under the reflectometer). Performing reflectometer measurements at several locations on the sample validates thin film layer thickness uniformity. Cross-section SEM can also be utilized to investigate thin film thickness and uniformity.

4.2.3   Lithography

Lithography is performed using an Elionix ELS-G100 100kV EBL system. Chemicals used in the lithography steps are listed in Table 4.4

Chemical	Silicon patterning	Polymer waveguides
E-beam resist	AR-P 6200.13	SU-8
Developer	AR 600-546	mrDev 600
Development stopper	Isopropanol	Isopropanol
Resist remover	Ar 600-71	PG remover

Table 4.4: Chemicals used in the lithography process steps.

Cleaning: Samples are cleaned using acetone and ethanol, both for a duration of 2 min. Samples are rinsed in IPA before dried with N_2 gas. Samples not coming directly from deposition are subject to plasma cleaning for a duration of 1 min.

Spin coating: E-beam resist, CSAR62 is spin coated onto the samples at 3000 RPM for 60 s with an acceleration of 500 RPM/s. The acceleration is included in the 60 s. The given acceleration and duration results in a resist thickness of approximately 490 nm.

Soft bake: After the resist is spin coated the samples are soft baked on a hot plate. Hot plate temperature is set to 150 °C and the samples are baked for 60 s. Soft baking the samples evaporate the solvents in the resist. Step 4 in Figure 4.7 illustrates a post baked sample.

Exposure: The EBL-guns acceleration voltage is set to 100 kV, and the area exposure dose to 350 μC/cm^2. Write fields of 500×500 μm^2 size, and a beam current of 1 nA are used. Step 5 in Figure 4.7 illustrates a post exposed sample.

Development: Samples are immersed and very lightly agitated in the developer for 60 s. samples are transferred to a beaker of development stopper (IPA), where they are immersed for 60 s. Step 6 in Figure 4.7 illustrates a post developed sample.

Inspection: An optical microscope is utilized to perform visual inspection of the lithographic process. The optical microscope exhibits magnification up to 100x. If the lithographic procedure is found unsatisfactory the photoresist is stripped and the process steps are repeated.

4.2.4 Etching

The silicon layer is etched at all EBL exposed regions by an Oxford Instruments Plasmalab System 100 ICP-RIE 180 instrument. The etching is performed using a recipe developed by L. Vigen [64]. The steps involved with etching are described in the proceeding steps.

Chamber preconditioning: Chamber preconditioning is performed whenever the previous user of the instrument has performed a process including a different etching chemistry. Chamber preconditioning is performed by etching a dummy wafer for 3 min.

Etching: Samples are etched according to the recipe in Table 4.5. Etch time is approximately 47 s. The samples are placed on a carrier wafer during the etching process. Due to pressure and vacuum conditions in the instrument the samples are glued to the carrier wafer with fomblin [42]. Fomblin can contaminate the ICP-RIE chamber. It is therefor important that the fomblin is used with care, and is only exposed to the sample/carrier-wafer interface. Figure 4.7, step 7 illustrates an etched sample.

Parameter	Value
SF_6	7.5 sccm
CHF_3	50 sccm
Pressure	15 mTorr
CCP power	40 W
ICP power	600 W
Temperature	20 °C
Duration	~30 s

Table 4.5: Parameters for ICP-RIE etching.

Resist removal: Resist is stripped of the samples either by sonication for 5 min in the resist remover for Silicon patterning in Table 4.4 or by plasma cleaning for 16 min. The process for plasma cleaning is similar to that listed in Table 4.2, only the generator frequency and O_2 gas flow are both set to 100%. For sonication removal the samples are rinsed with ethanol and IPA, and dried with N_2.

4.2.5 Inverted Taper Coupling

Inverted tapers have already been imprinted in the silicon layer by the exposure step in Subsection 4.2.3. The inverted tapers need a polymer waveguide coating to confine input light. The steps performed to produce the inverted taper coating are explained below. The chemicals used in the fabrication steps are listed in Table 4.4 under polymer waveguides. The MLA used for exposure is a Heidelberg instrument MLA150. It has two light sources. One with a center frequency at 405 nm, the other at 375nm. The photoresist, SU8 serves the purpose as polymer waveguide coating. Etching is therefor not needed as a process step for inverted taper fabrication.

Cleaning: The samples are cleaned using the plasma cleaner (Diener Electronics Femto) with the parameters in Table 4.2, but for a duration of 2 minutes instead of one.

Spin coating: Photoresist is spin coated onto the samples at 3500 RPM for 60 s with an acceleration of 1000 RPM/s.

Soft bake: After the resist is spin coated the samples are soft baked on a hot plate. Hot plate temperature is set to 95 ∘C and the samples are baked for 3 min.

Exposure: The MLA source at 375 nm and a dose of 3050 mJ/cm^2 is used.

Post exposure bake: Samples is baked for 3 min at a temperature of 95 ∘C after exposure.

Development: Samples are immersed and lightly agitated in the developer for 60 s. Samples are transferred to a beaker of development stopper (IPA), where they are immersed for 60 s. Samples are carefully dried with N$_2$ gas.

Inspection: An optical microscope is utilized to perform visual inspection of the lithographic process. The optical microscope exhibits magnification up to 100x. If the lithographic procedure is found unsatisfactory the photoresist is stripped and the process steps are repeated.

4.3 Characterization

Fabricated samples are examined and characterized using a SEM and by transmission testing in a laser setup.

4.3.1 Scanning Electron Microscope

A FEI APREO is the SEM instrument used for visualizing and examining the samples. The SEM is predominantly used after development, etching, and resist removal. The sample is attached to a sample stub by adhesive tape or placed in a cross-section sample holder. The sample stub, or sample holder is mounted in the SEM chamber. The FEI instrument images rely on the two physical processes, secondary electron detection and back scattered electron detection. The acceleration voltage of the electron beam can be tuned from 0.2 kV to 30 kV, and the maximum beam current is 400 nA.

4.3.2 Transmission Measurements

Transmission measurements are performed using a laser setup. the laser setup is illustrated by the block diagram in Figure 6.5.
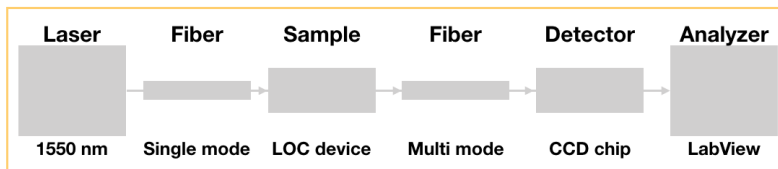
Figure 4.8: Schematic illustration of a laser setup to perform transmission measurements. The laser is a tunable diode laser with a center frequency at 1550 nm. A single mode fiber guides the light from the laser to a sample subject to transmission testing. The sample in this case is a fabricated LOC device. A multi mode fiber guides the light from the LOC device to a detector. The detector is a silicon charge coupled device (CCD) chip. Information from the CCD chip is relayed to a computer where the software LabView is used to analyze the received information.

The laser used is a tunable diode laser (TLK-L1550M Thor Labs) with a center frequency at 1550 nm. It is tunable in the wavelength range 1480-1640 nm (see Appendix H). The output light is guided to a sample subject to transmission testing through a single mode fiber. The sample is in this case a LOC device. A multi mode fiber guides the light from the LOC device to a detector. The detector is a silicon charge coupled device (CCD) chip. Information from the CCD chip is relayed to a computer where the software, LabView is used to analyze the received information [30]. The signals relayed from the CCD chip are amplified before analyzed by LabView. A camera is attached to the microscope allowing transmission measurements to be visually verified as the laser sweeps over a defined wavelength range.

Straight waveguides and line defects are measured by coupling light in at one end of the sample and detecting at the other end. For PCRR measurements the procedure is slightly different. The PCRRs are coupled to two waveguides. One waveguide is intended

for input and transmission output. The third waveguide is used for drop-filter transmission measurements. The PCRRs are swept across the laser range in transmission setup. As the laser sweeps, the drop-filter waveguide is visually inspected to identify possible frequency components. If frequency components are detected the detector is moved to the drop-filter transmission waveguide to inspect the observed frequency components. When inspecting the visually observed frequency components the sweep speed and range are both reduced to improve resolution.

5. Results and Discussion

This chapter includes the results from simulations, fabrication, and characterization. First all the various design solutions are presented. Design solutions are illustrated and geometrically explained. The theoretical reasoning for each design solution is explained. Explanations are either based on previous work on PCRRs and PC cavities, or on theory presented in Chapter 2. Results from band diagram simulations, transmission simulations, and mode simulations are presented for both two- and three-dimensional cases. Simulation results are discussed and compared across design solutions.

Images captured from various fabrication steps is presented as results. The images are explained and discussed as a mean to reflect on fabrication challenges. Cross-sectional images captured form the PC sections of the LOC devices are also presented. A section covering fabrication challenges and visual results substantiates a discussion about transmission results of fabricated LOC devices.

Transmission spectra from produced LOC devices are presented and discussed. They are compared across design solutions. Comparisons between simulation and fabrication results are also presented and discussed.

5.1 Design Solutions

There are several design configurations subject to simulation and fabrication. They are all covered in this Subsection. The various design solutions are both simulated and fabricated identically. The only procedural difference is their geometrical representation in simulation scripts and GDS-files (file read by EBL). Table 5.1 represents all design solutions.
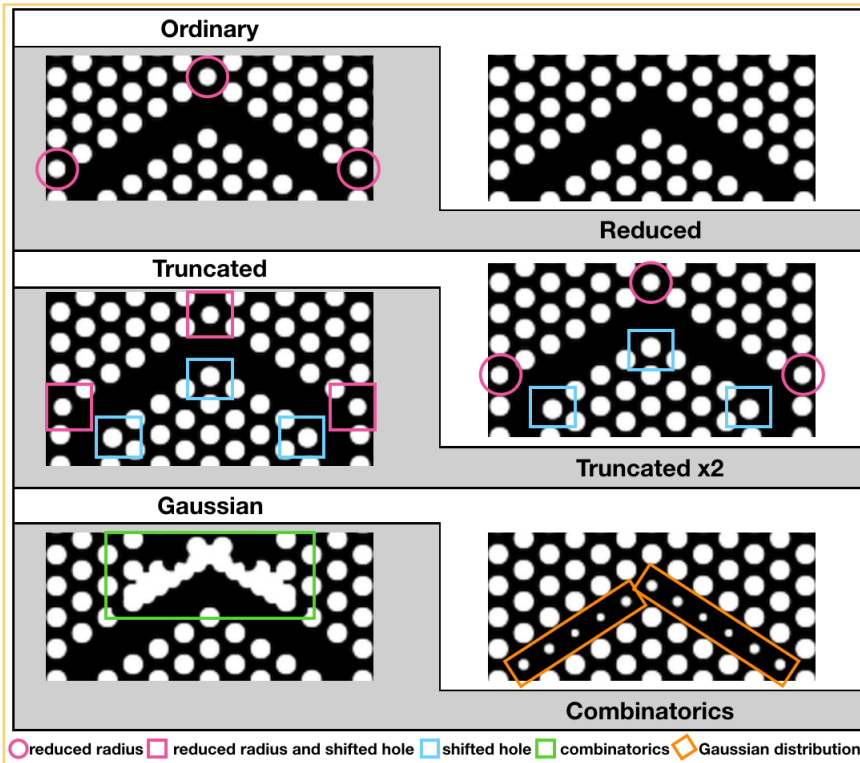
Table 5.1: Table listing all the designs solutions that are simulated and fabricated. The radius is reduced with a factor of 0.889 for the holes with a surrounding pink circle [71]. The holes surrounded by a pink rectangle are additionally shifted by a factor 0.1 of the lattice constant. Holes surrounded by a blue rectangle are only shifted, not reduced as the pink rectangles. The green rectangle illustrates the area subject for combinatorial modifications. The yellow rectangles surround holes subject to a Gaussian distribution defined hole radius.

The design solutions listed in Table 5.1 represent all the design solutions, and highlight their design characteristics. Their characteristics are illustrated as a partition from a ring resonator ring-side. Figure 5.1 illustrates the partitioning for the Gaussian design solution. The partitioning is identical for all ring resonator ring sides, except for the combinatorics design (see Figure 5.3). The combinatorics design exhibits a mirror symmetry around the grey dashed line in Figure 5.1, the other designs exhibit a six-fold rotational symmetry. Illustrations of all the designs are found in Appendix D.
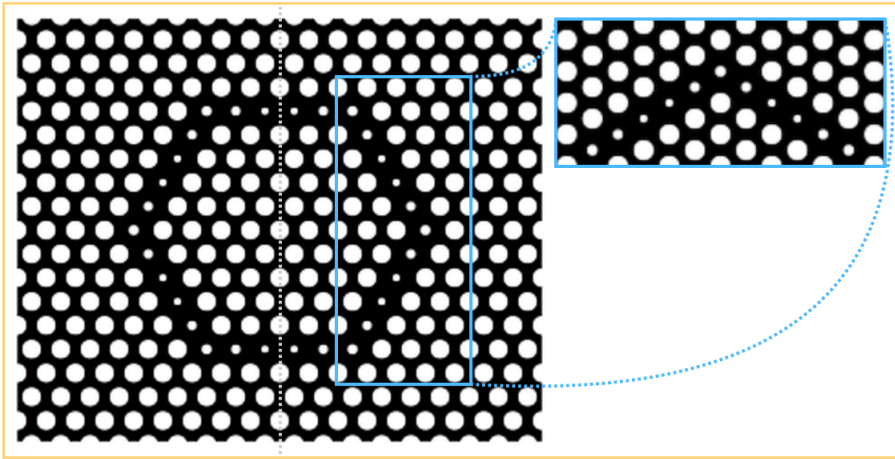
Figure 5.1: Figure describing the relation between the PCRRs and the illustrations in Table 5.1. The Gaussian design is used for illustration purposes. For all design solutions except for the combinatorics design the relation is as illustrates by the Gaussian design. The combinatorics design exhibits two-fold rotational symmetry, or mirror symmetry along the grey dashed line. All other designs exhibit the same six-fold rotational symmetry as the Gaussian design (see Appendix D).

Ordinary

The ordinary design is created by simply removing air-holes from the PC. The holes are removed in a circular manner, creating a hexagonal pattern. The other designs are created by performing variations to the ordinary design.

Reduced

The reduced design is created by reducing the holes located on the outside of the ring resonator corner by a factor 0.889. The physical explanation for doing so is explained by J. Xia et Al. in "High-quality-factor photonic ring resonator" [71]. Briefly explained, a reduction in hole radius of corner holes reduces the amount of small tangential wavevector components. Small wavevector components can couple to light cone modes (see Figures 2.12 and 2.16). Light cone modes can escape to the PCRR cladding, which is either air or silica. Tangential wavevector components are defined as components within the photonic crystal plane. The reduction factor of 0.889 was empirically found to be the optimum by J. Xia et Al..

More specific optimization work on PCRR has not been found in this thesis work, and further design solutions have drawn inspiration from other PC design structures.

Truncated and Truncated x2

The truncated design has the same outer ring-resonator corner hole configuration as the reduced design. In addition the truncated design has shifted inner ring-resonator corner holes. The holes are shifted by a factor 0.1 of a lattice constant. The holes are shifted

towards the origin, therefor the name truncated. The truncated x2 design is very similar to the truncated design. It exhibits all the attributes mentioned for the truncated design. In addition the outer ring-resonator corner holes are shifted towards the origin with a factor 0.1 of a lattice constant. Truncating the corner holes is an attempt to smooth out the corners in the ring resonators. When light propagates in the ring resonators the light experiences a 60° bend at each corner. There is loss associated with each 60° bend. The 60° bends are an intrinsic property of a triangular air-hole lattice PC, and are difficult to avoid. Although truncating the corner holes is an attempt to smooth out the ring resonator, it also perturbs the intrinsic symmetry beyond the introduction of the ring resonator itself. The effects of further symmetry perturbations are difficult to define without empirical testing the structures.

Gaussian

The Gaussian design differs from the ordinary design in that it exhibits air-holes within the line-defects constituting the ring resonator. The holes within the line-defects have a Gaussian distribution determined hole radius (see Figure 5.1 and Table 5.1). Specifically, the hole radius is determined as.

$$r(d) = 0.15a - a\frac{e^{-d^2}}{5} \tag{5.1}$$

a in Equation 5.1 is the lattice constant, d is the spatial variable along the line-defect in units of lattice constant. d is defined as zero at the center of the line defect, and reaches its maximum absolute value of 2.5 at the line-defect corner holes. The specific hole radii are $r = [0.1465, 0.1241, 0.0796, 0.0796, 0.1241, 0.1465] \cdot a$. The factors 0.15 and 5 in Equation 5.1 are set to prevent the air-holes of becoming too large and thereby erasing the ring resonator, or too small and becoming unfeasible for fabrication. The design idea behind Gaussian distributed ring resonator holes is inspired by work done on drop filters and nanobeam cavities [5][62]. The physical explanation for a Gaussian distribution is explained in Chapter 2 Section 2.8.

Combinatorics

The combinatorics design is based on removing air-holes in a defined region where combinatorial computation determines the spatial permittivity distribution. The combinatorial computational cell has a resolution of 32 pixels. One pixel is the size of a normal air-hole (radius of 0.3a). With no constraints applied, the number of possible solutions exceeds 4×10^9. The constraints applied on the combinatorial computational cell are:

- The cell must exhibit mirror symmetry (see Figure 5.3).

- Resulting structure must topologically be either a sphere, torus, or a genus [20].

- The pixel size must be feasible to fabricate.

Mirror symmetry effectively reduces the computational cell and resolution by a factor of two. Sphere, torus, and genus are topologically defined structures. The topological

constraint ensures that the resulting air-hole is not two or more separate air-holes. The resulting air-hole is allowed to have "islands" of silicon within itself. This constraint is anchored in topological mathematics and is not necessarily a performance enhancing constraint. The constraint is important in reducing the number of possible solutions. With the given constraints, the number of possible solutions is reduced to 199. A two-dimensional mode simulation is performed on each solution to determine their q-factors. The geometric structure used for the mode simulations is illustrated as the smaller inserted structure in Figure 5.3. The result from the mode simulation is presented in Figure 5.2.
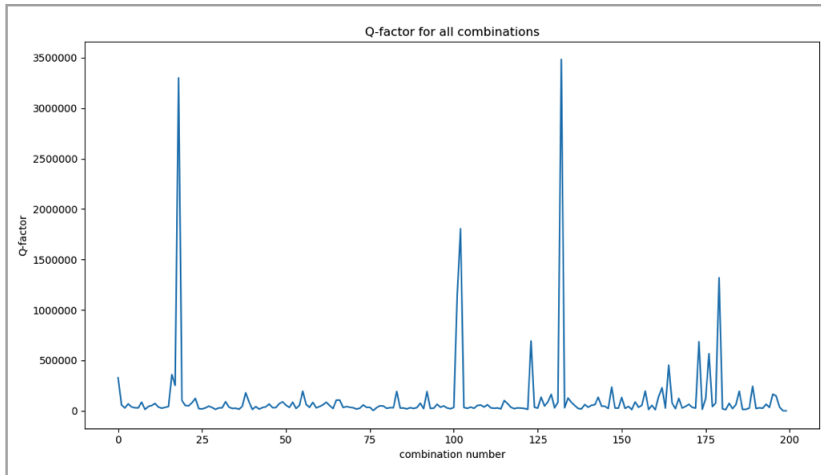
Figure 5.2: Result from the two-dimensional mode simulation on all 199 possible design solutions. Vertical axis is Q-factor and horizontal axis is design solution number. The peak q-factor value of 3.5×10^6 belongs to design solution number 133.

Figure 5.2 reveals that design solution number 133 exhibits the highest q-factor of 3.5×10^6 and is illustrated in Figure 5.3.
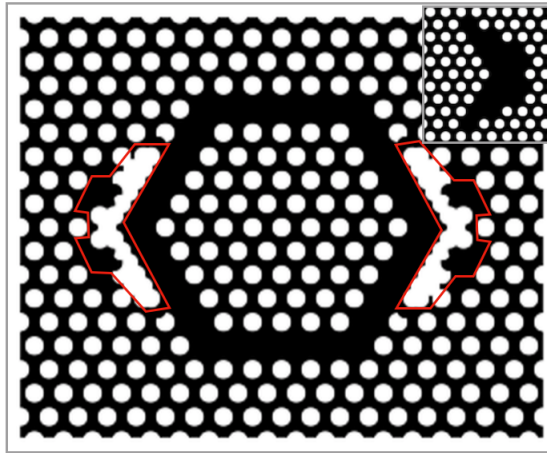
Figure 5.3: Illustration of the design solution achieving the highest q-factor (q-factor of 3.5×10^6). The red areas defines the combinatorial computational cell. The inserted structure illustrates the structure used to distinguish the possible solutions by their q-factors.

Figure 5.3 illustrates the ring resonator structure achieving the highest q-factor. The inserted structure illustrates the structure used to distinguish the possible solutions by their q-factors. The area within the red window is the combinatorial computational cell.

A combinatorial approach to PCRR design is inspired by work done on optimizing PC $60°$ bends [54][16]. M. Kristensen et Al. reported a reduction in PC waveguide bend loss from 8 dB to below 1 dB for topological designed corners. They also reported an increase in transmission bandwidth for TE polarization for the same topological designed corners. The transmission bandwidth was reported to exceed 200 nm [16].

5.2 Simulations

Simulation results are presented in the same order as in Chapter 4. MPB results for intrinsic PC are presented for both two- and three-dimensional simulations. Results from frequency domain simulated line defects and slab waveguides are presented together with intrinsic PC simulation results. The frequency domain simulations are discussed before the attention is shifted to time-domain transmission simulation results. Two- and three-dimensional simulation spectras are compared, both with each other and with frequency domain simulation results. Finally, mode simulation results in terms of Q-factor are presented and compared across design solutions.

5.2.1 Band Diagrams

Band diagrams have been calculated for two-dimensional and three-dimensional structures. Band diagrams of two-dimensional intrinsic PC is presented in Figure 5.4. Varying air-hole radius causes the differences in band diagrams.
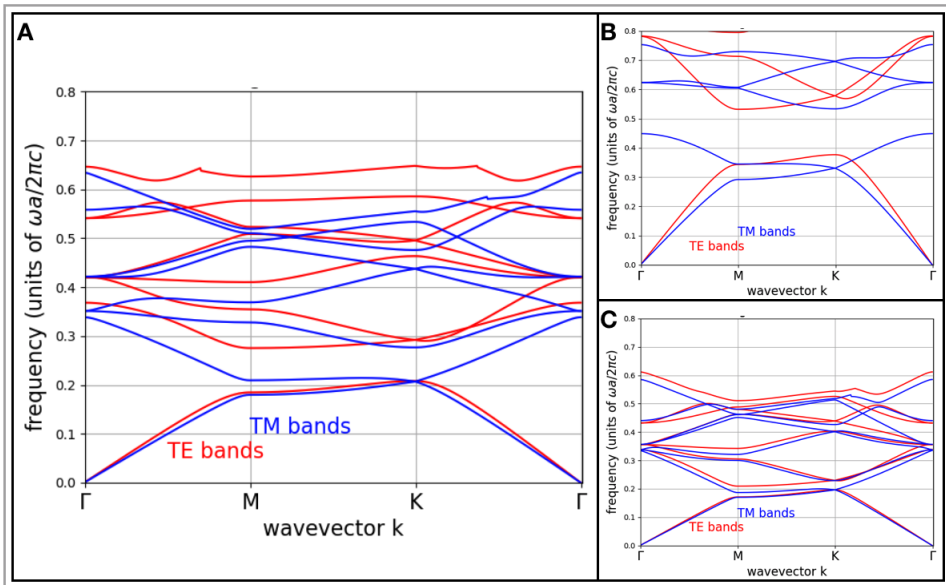
Figure 5.4: Band diagrams for two-dimensional triangular air-hole lattice PC with hole radii 0.3a (**A**), 0.48a (**B**), and 0.2a (**C**). As the hole radii is increased the dispersion relation blue-shifts in frequency. The band-gaps themselves increases with increasing hole radii.

Figure 5.4 illustrate plots of the band diagram for intrinsic hexagonal PC. Plot A represents a PC with hole radius of 0.3a, while B and C have hole radii of 0.48a and 0.2a, respectively. TE-polarized bands are marked in red while TM-polarized bands are marked in blue. The vertical axis is frequency normalized for lattice constant, a and speed of light c. Horizontal axis is wavevector, k along the boundary of the irreducible Brillouin zone (IBZ) (See Figure 2.11 in Chapter 2 for explanation). The dispersion relation is plotted along the IBZ since dispersion relation maximum and minimum tend to appear there. Band-gaps of interest are those between band one and two. The reason being that for hexagonal PC the larger band-gaps appear between band one and two. Band diagram simulations are done for the first eight bands for each polarization.

For Figure 5.4 A a TE-polarized band-gap is apparent from normalized frequency 0.208 to 0.275. A complete band-gap from frequency 0.449 to 0.532 is observed for a hole radius of 0.48a. A complete band-gap appears wherever TE- and TM-polarized band-gaps coincides. The TE-polarized band-gap extends beyond the complete band-gap, all the way down to 0.377 normalized frequency. For Figure 5.4 C the band-gap is truncated to the extent that the band-gap almost disappears. The center frequency of the disappearing band-gap is approximately 0.20.

Dispersion relation for air-hole PC lattice along x-direction is also of interest. The interest in x-direction dispersion relation becomes evident when considering line-defects in intrinsic PC. A line-defect interrupts symmetry in all directions except for x-direction.
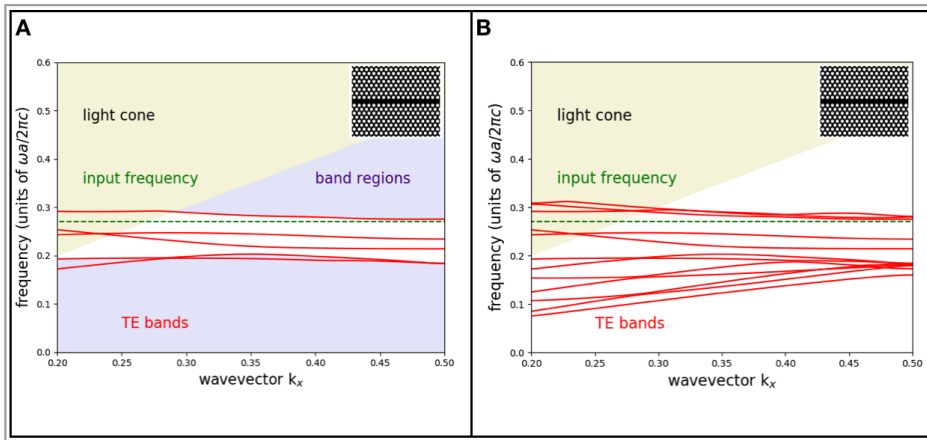
Figure 5.5: Dispersion relation along x-direction for line-defects in two-dimensional PC is illustrated in figures **A** and **B**. Input frequency is illustrated with a green dashed line and corresponds to a input center wavelength of 1550 nm. All dispersion relations are only valid for PC with a hole radius of 0.3a. Wavevector k_x is given in units of $2\pi a/\lambda_x$.

The dispersion relation in Figure 5.5 is plotted for normalized frequency (normalized on lattice constant a and speed of light c) and wavevector k_x from 0.2 to 0.5. Figure A illustrates the dispersion relation for PC with line-defect along x-direction. The TE-bands with no relation to the first band-gap have been replaced by purple band regions. Figure B illustrates dispersion relation for PC with line-defect. Figure B differs from A in that it includes the first 12 TE polarized bands. A line-defect introduces additional propagating modes. Some of the propagating modes are introduced in band regions, and others are more interestingly introduced in band-gap regions. The two modes in the white area of Figure 5.5 A, are propagating modes introduced in the first band-gap region.

Frequency domain simulations presented so far as results have all been two-dimensional simulations. The same simulations have been performed for the equivalent three-dimensional structures. The substrate (layer beneath the silicon layer) has been varied for three-dimensional simulations. The substrate has either been air or silica. Air has a refractive index of approximately unity while silica exhibits a refractive index of 1.45 in the 1550 nm wavelength range. The difference in refractive index affects the refractive index contrast experienced within the PC. Introducing a silica substrate to the simulated structure breaks any symmetry in the slab thickness direction. The symmetry breakage causes TE- and TM-like modes to couple and destroy any TM/TE-only band-gap [31].
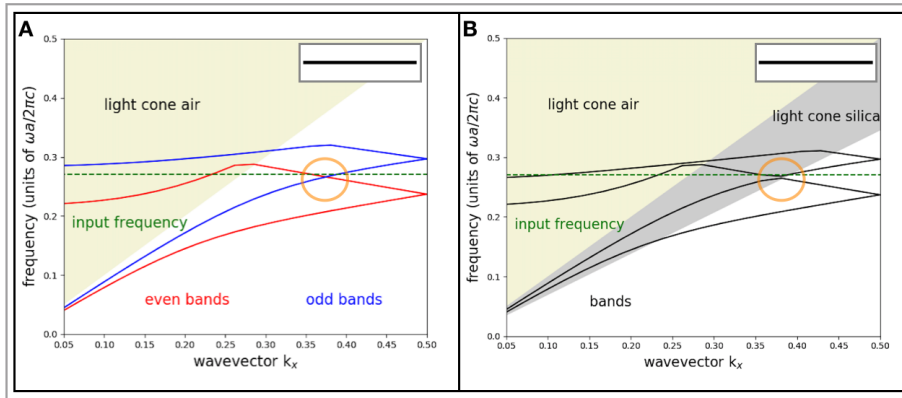
Figure 5.6: Illustration of guided modes in a slab waveguide. The dimensions of the waveguide are given in Table 4.1. The width of the waveguide is set to 500 nm. The substrate for the structure simulated in Figure **A** is simulated as air. The substrate for the structure simulated in Figure **B** is simulated as silica. The dispersion relation for both structures are is simulated along the waveguide length. Wavevector k_x is given in units of $2\pi a/\lambda_x$.

Figure 5.6 illustrates the dispersion relation for slab waveguides. The dispersion relations are simulated for three-dimensional structures. Figure A represents a slab waveguide structure where the substrate is simulated as air. In Figure B the substrate is simulated as silica. The symmetry breakage associated with silica substrates is evident within the yellow circles. For an air-substrate structure, where the symmetry in the slab thickness direction is conserved the even and odd bands are intact. For the silica-substrate structure the symmetry is broken and the even and odd modes have coupled with each other.
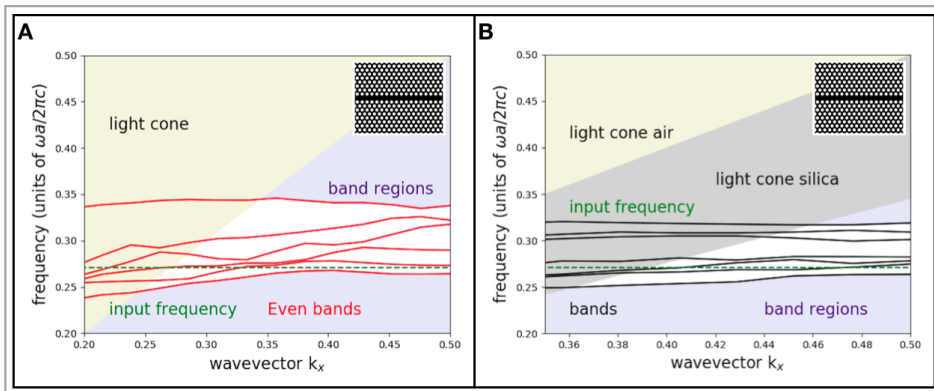
Figure 5.7: Dispersion relation along x-direction for line defects in three-dimensional PC is illustrated in figures **A** and **B**. Figure **A** represents a structure where the substrate is simulated as air. Figure **B** represents a structure where the substrate is simulated as silica. Input frequency is illustrated with a green dashed line and corresponds to an input center wavelength of 1550 nm. All dispersion relations are only valid for PC with a hole radius of 0.3a. Wavevector k_x is given in units of $2\pi a/\lambda_x$.

Figure 5.7 illustrates the dispersion relation for line defects in PC along the x-direction (Γ to K' in Figure 2.10). Figure A represents a structure where the substrate is simulated as air, while in Figure B the substrate is simulated as silica. The x-axis is shifted from Figure A to Figure B. A smaller wavevector range is of interest for Figure B due to the silica light cone. Figure 5.7 illustrates that there exists a band-gap that overlaps with an input frequency (when PC is designed with air-hole radius 0.3a) for line defects along the x-direction for slab PC, both with air and silica substrate.

Figure 5.8 illustrates the dispersion relation along the IBZ for intrinsic slab air-hole triangular PC. Figure A represents intrinsic PC with simulated air substrate, while Figure B represents intrinsic PC with simulated silica substrate. Figures include the light line for air and silica. A input center wavelength of 1550 nm is visualized with a green dashed line.

Figure 5.8: Dispersion relation for two slightly different intrinsic slab PC structures. Figure **A** illustrates the case where the substrate is simulated as air. The light line for air is visualized to clarify for which wavevector values modes can couple to the substrate. Figure **B** illustrates the case where the substrate is simulated as silica. The light line for air and silica is visualized for the same reason as in Figure **A**. The green dashed line indicates a input frequency corresponding to a wavelength of 1550 nm. Both dispersion relations are valid for structures with a air-hole radius of $0.3a$.

The dispersion relation for three-dimensional simulated structures is evidently quite different from the two-dimensional counterpart. For two-dimensional simulations there exists a complete TE-mode band-gap with a hole radius of $0.3a$ (see Figure 5.4). TE-mode band-gaps only exists in certain reciprocal lattice directions for three-dimensional structures. These observations are made with out considering the light line (see Figure 2.12). When considering the light line confined band-gaps the band-gaps resemble each other despite the dimensional difference. However, the frequency is blue-shifted for three-dimensional simulations. The blue-shift can be understood by considering one very thin and one very thick slab PC. The very thick slab PC will approach the dispersion relation for a two-dimensional PC, as in Figure 5.4 as the slab thickness approaches infinity. Guided bands for a thin slab PC will approach the light line as the thickness approaches zero

(i.e. no PC structure). The dispersion relation for a slab thickness defined in Table 4.1 is expected to behave as something in between the two extreme conditions. The first even band in Figure 5.8 is clearly more "attracted" to the light line than the case for two-dimensional PC (see Figures 2.12 and 5.4). All even bands with a frequency smaller than that of the light line will naturally become blue-shifted towards the light line. The thickness of the slab is in other words shifting the band-gap.

There are some difference in dispersion relation for an air-substrate structure and a silica-substrate structure. When considering Figure 5.8 the higher frequency guided bands appear to be red-shifted in frequency. This is not the case. The explanation for what appears to be a red shift is similar to the slab waveguide explanation (see Figure 5.6). The silica substrate breaks symmetry in the slab thickness direction. Even and odd modes couple with each other as a result of the symmetry breakage. The bands in Figure 5.8, B are therefor a combination of even and odd bands that have coupled together. The amount of bands calculated for are the same for Figure A and B. Since only even bands are calculated in Figure A, the dispersion diagram includes higher frequency bands.

5.2.2 Transmission Simulations

Transmission simulation spectra are found in Appendix E, both for two- and three dimensional simulations. Only transmission spectra from a few of the design solutions are offered in this Subsection.

Figure 5.9 illustrates the resulting spectra for the ordinary design solution.
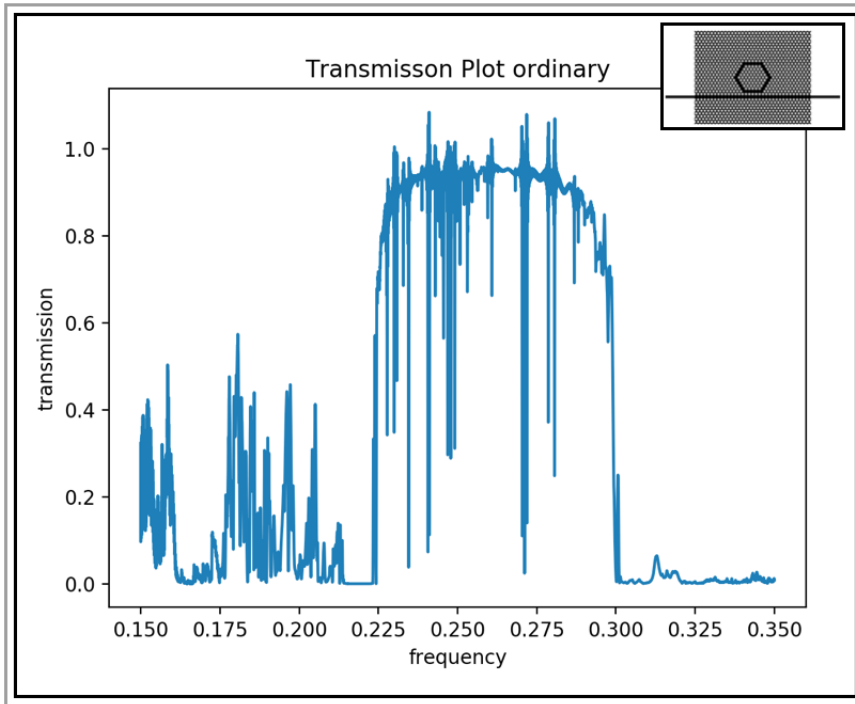
Figure 5.9: Transmission spectra for the design solution ordinary. Transmission spectra is normalized by the reference structure (see Figure 4.5). The transmission band is clearly visible from 0.225 to 0.300 normalized frequency. The transmission spectra exhibit several missing modes in the transmission band, assumed to have coupled to the ring resonator.

Figure 5.9 is a spectra from a two-dimensional transmission simulation. The frequency axis is normalized by the lattice constant, a and the speed of light, c (identical to Figure 5.8). The transmission band is clearly visible from 0.225 to 0.300 normalized frequency. Within the transmission band there are several inverted spikes. These inverted spikes are assumed to be modes that have coupled into the ring resonator. The spikes visible from 0.150 to 0.200 normalized frequency are partially guided modes from the line defect. They are not of interest as they lay outside the band-gap intended for exploitation. The transmission spectra in Figure 5.9 can be compared to the dispersion relation in Figure 5.4, A. By only evaluating the dispersion relation a band-gap is expected to appear in the normalized frequency range 0.208 to 0.275. The transmission simulated band-gap is evident from normalized frequency 0.225 to 0.300. The two bandwidths are overlapping. There is a mismatch from 0.208 to 0.225 and 0.275 to 0.300. The mismatch can be explained by the fact that the dispersion relation in Figure 5.4, A and the spectrum in Figure 5.9 do not represent the same structure. The dispersion relation is calculated along the IBZ proximity for an intrinsic PC configuration, while the spectra is detected for electric field y-components transmitted through the transmission setup. The overlap in band-gaps should be dominant enough to convince the reader that the spectral band-gap is a photonic crystal property.
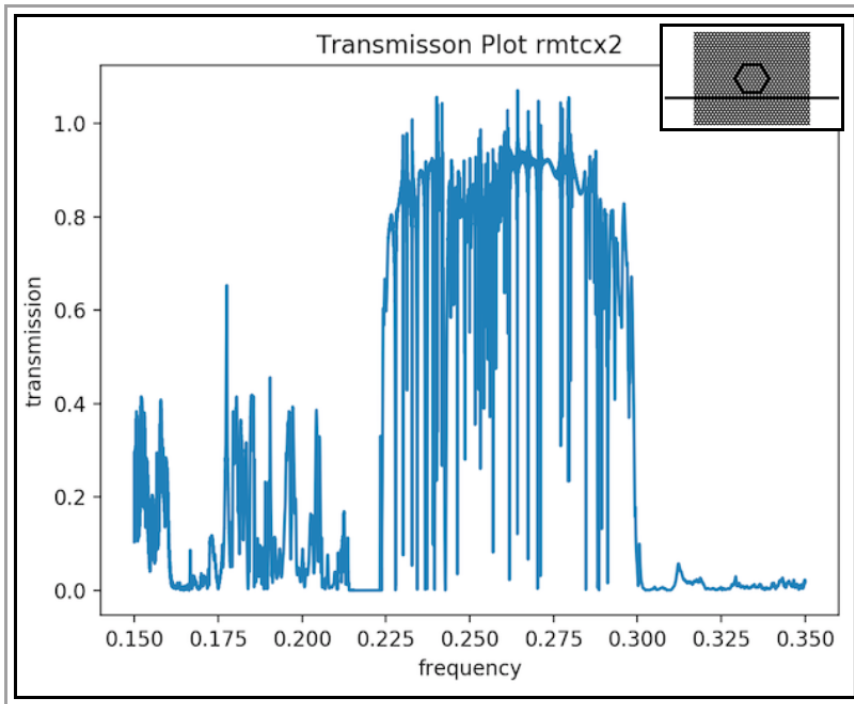
Figure 5.10: Transmission spectra for the design solution rmtcx2. Transmission spectra is normalized by the reference structure (see Figure 4.5). The transmission band is clearly visible from 0.225 to 0.300 normalized frequency. The transmission spectra exhibit several missing modes in the transmission band, assumed to have coupled to the ring resonator.

Figure 5.10, which represents the rmtcx2 design solution is offered as a comparison to the ordinary design solution. The band-gap itself has the same bandwidth and center frequency as the band-gap for the ordinary design solution. Within the band-gap there are more inverted spikes for the rmtcx2 design solution. The rmtcx2 design solution exhibits design features such as shifted and reduced corner holes (see Table 5.1). An isolated reduced air-hole can be compared to a point defect (point defects are covered in Chapter 2). A point defect introduces localized modes. How these localized modes are introduced when the surrounding geometry is designed as a PCRR is too complex to describe in a detailed manner. The best possible explanation is to treat the ordinary design solution spectra as a reference spectra for the rmtcx2 design solution. The additional modes in the band-gap for the rmtcx2 design solution are in this framework dedicated to the shifts and reduction in corner holes. More modes may substantiate mode matching at a line-defect/ring-resonator interface. A line defect mode has a higher probability of matching to a ring resonator mode with similar center frequency and group velocity. More modes within the band-gap is not necessarily beneficial for LOC purposes. The spectral distance between modes becomes smaller with more modes. When the spectral distance decreases the likelihood of mode coupling within the ring resonator increases.

Figure 5.11 Illustrates the transmission spectrum for the ordinary design. The spectrum

belongs to a three-dimensional simulation where the substrate is simulated to be air.
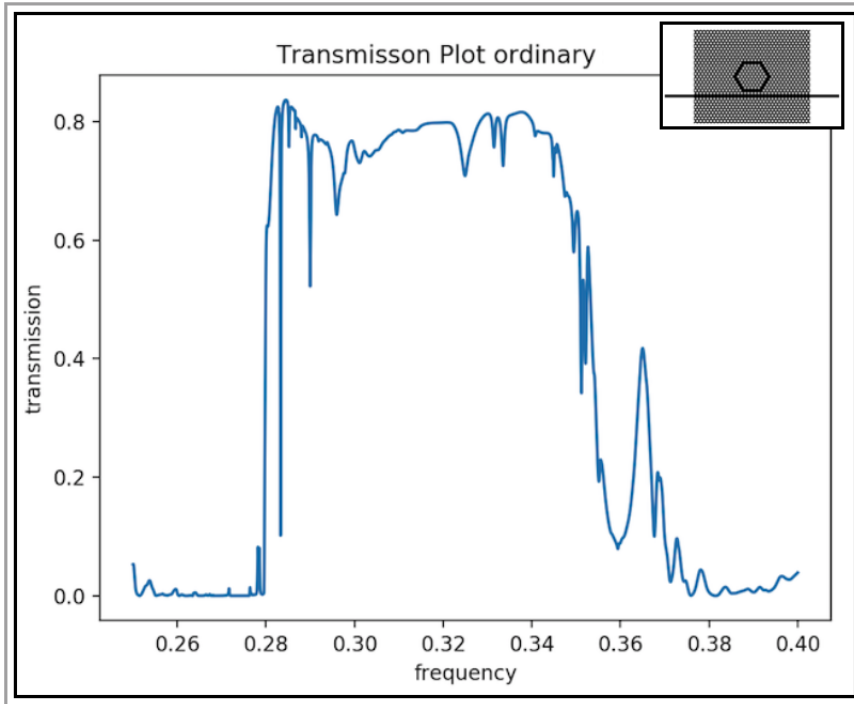
Figure 5.11: Transmission spectra for the design solution ordinary. The spectra represents a three-dimensional structure with substrate simulated as air. Transmission spectra is normalized by the reference structure (see Figure 4.5). The transmission band is clearly visible from 0.228 to 0.380 normalized frequency. The transmission spectra exhibit some missing modes in the transmission band, assumed to have coupled to the ring resonator.

The frequency in Figure 5.11 is normalized with respect to the lattice constant a and speed of light, c (identical to Figure 5.4). A transmission band is visible from normalized frequency 0.228 to 0.380. The Transmission band is blue-shifted in frequency compared to the corresponding two-dimensional case (see Figure 5.9). The explanation for the blue-shift is identical to the explanation given for dispersion relation differences for two- and three-dimensional simulations (see second to last paragraph in Subsection 5.2.1).

The transmission band itself exhibits less inverted spikes than its two-dimensional counterpart. In a two-dimensional simulation, light is forced to only interact with the photonic crystal configuration. Three-dimensional simulations do not impose that same constraint. Light can couple out to substrate as it propagates through the structure. Light originating from a dipole source experiences broadening in structure thickness direction as it propagates away from the source [55]. The broadening itself can be decomposed in in-plane and out-of-plane components. Here in-plane refers to the photonic crystal plane while out-of-plane refers to the plane coinciding with the structure thickness direction. As the light broadens the in-plane wavevector component becomes smaller while the out-of-

plane component becomes larger. A smaller in-plane component can couple to light cone modes, which again couples to the substrate. Light broadening in structure thickness direction is naturally only considered in three-dimensional simulations. The third dimension and light leakage to substrate is accounted for the reduction in number of inverted spikes and their reduction in depth.

5.2.3 Mode Simulations

Mode simulation results are presented for all design solutions. Mode simulation results are Q-factor values expressing the longlivety of a given mode in a specific design solution. All Q-factor values are found in Appendix F. Results are presented for both two- and three-dimensional simulations in this section.
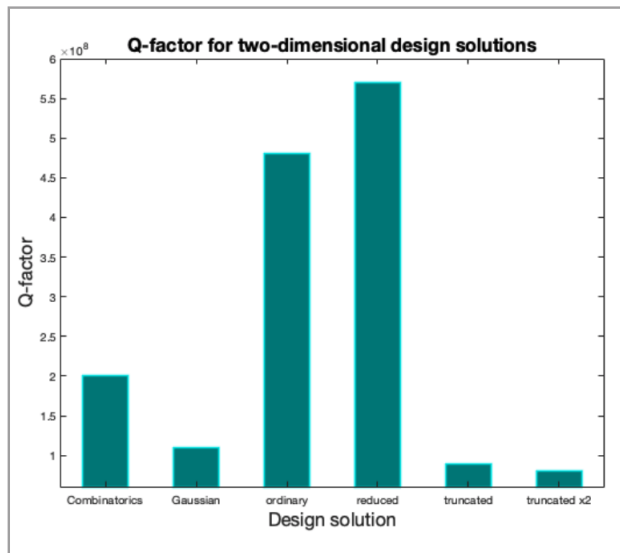
Figure 5.12: Diagram of Q-factors for all design solutions simulated in two-dimensions. All Design solutions exhibit Q-factor values of more than 8×10^7.

Figure 5.12 presents the achieved Q-factor for two-dimensional simulations. All Design solutions exhibit Q-factor values of more than 8×10^7. Design solution reduced achieved the highest Q-factor for two-dimensional simulations of 5.7×10^8. The Q-factor magnitude depends on several factors. One of the factors is the PC area (i.e. how far beyond the PCRR the PC extends). The Q-factor increases with increasing PC area. What is interesting with the mode simulation results is the difference in Q-factor across the different design solutions. For two-dimensional simulations the Q-factor results are all within a range of one order of magnitude from each other. A high Q-factor for all designs and variations less than an order of magnitude indicates that high energy confinement and longlivety of modes are intrinsic properties of PCs. Small variations in design configurations can (as documented) increase or decrease the Q-factor. All design solutions are small

enough changes for the PC structure to maintain its intrinsic properties. Only the reduced design shows improvement over an ordinary PCRR for two-dimensional simulations.

Figure 5.13 presents the achieved Q-factor values for three-dimensional simulations where the substrate is simulated as silica.
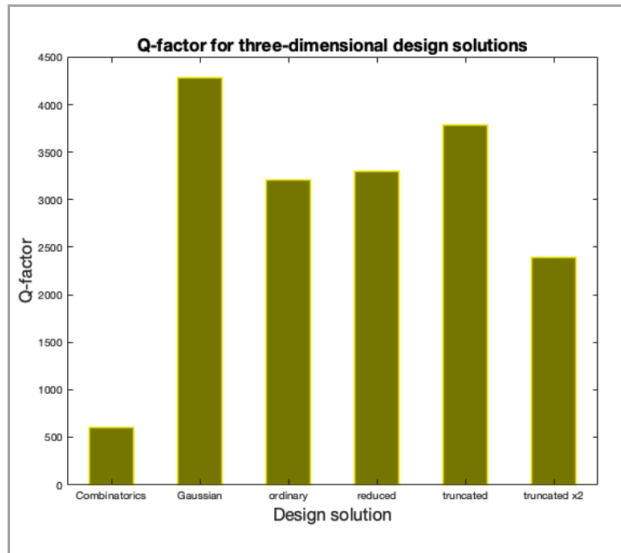
Figure 5.13: Diagram of Q-factors for all design solutions simulated in three-dimensions and with silica as substrate. All design solutions exhibit Q-factor values of more than 2000, except for the combinatorics design solution.

All design solutions exhibit Q-factor values of more than 2000, except for the combinatorics design solution. The Gaussian design solution achieved the highest Q-factor value of 4286. Q-factor values are drastically reduced when simulated in three-dimensions. As with transmission simulations, light from a Gaussian source experience broadening as it propagates away from the source. Change in in-plane and out-of-plane wave decomposition allows for light coupling to the substrate. Coupling to the substrate is evident as the Q-factors are drastically reduced. Not much consistency is observed in Q-factor values across design solutions when comparing two-dimensional simulations with three-dimensional simulations. When performing mode simulations, determining a reasonable time to simulate after the source is turned of is important. If that time is too short the returned Q-factor values can become affected by the source itself [51][1]. Placing the center frequency of the source so that modes are activated is important. Q-factor inconsistency across design solutions when comparing two- and three-dimensional simulations may suggest that run-time or center-frequency arguments where not controlled well enough for one or more simulations. Another explanation for the inconsistency across design solutions follows that of J. Xia et Al. "High-quality-factor photonic crystal ring resonator" [71]: Some design solutions experience a reduction in in-plane wavevector components that are smaller than $k_0 = 2\pi/\lambda_0$. k_0 is in this case the k-vector of the substrate. Wave in the lightcone can escape to the substrate (i.e. wavevector components smaller than k_0). A

two-dimensional simulation does not consider such loss, which could explain the inconsistency across design solutions when comparing to three-dimensional simulations.

Figure 5.14 presents the achieved Q-factor values for three-dimensional simulations where the substrate is simulated as air.
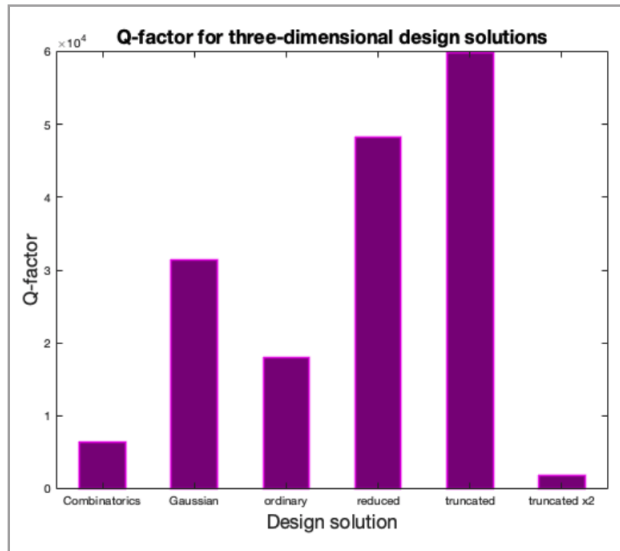
Figure 5.14: Diagram of Q-factors for all design solutions simulated in three-dimensions and with air as substrate.

All design solutions exhibit Q-factor values of more than 10000 except for combinatorics and truncated x2. The truncated design solution achieved the highest Q-factor value of 59871. Q-factor values are higher when the substrate is simulated as air. This is expected as the refractive index contrast is higher for silicon and air than for silicon and silica (slab and substrate). A higher refractive contrast implies that in-plane wavevector components must be smaller to couple out to the substrate. There is more consistency observed across design solutions when comparing simulations with substrate variations than comparing simulations with dimensional differences. More consistency across design solutions when comparing simulations with substrate variations substantiates an explanation based on reduction in small in-plane wavevector components.

5.2.4   Simulation Summary

Simulations for dispersion relations of intrinsic PC, line defects in PC and strip waveguides have been performed in both two and three dimensions. Strip waveguides exhibit band mixing for non-symmetric strip waveguides. The band mixing is in accordance with literature. Simulations of intrinsic PC has an explainable transition from two- to three-dimensional simulations. Line defect simulations exhibit guided modes in the same frequency range as the strip waveguides. Modes in overlapping frequency range across simulations is important for coupling between structures. Intrinsic PC simulations exhibit

a band-gap in the frequency range where line defect and strip waveguide modes exists. Matching line defect modes with the and-gap of intrinsic PC is desirable to substantiate coupling to guided modes within the band-gap for PCRRs.

Transmission simulations have been performed for all design solution in both two and three dimensions. Two dimensional simulations exhibit clear and sharp resonances in form of inverted spikes in the band-gap region (i.e. transmission band). The two-dimensional transmission spectra coincides with dispersion relations for two-dimensional intrinsic PC. Three-dimensional transmission simulations also coincides with dispersion relations for three-dimensional intrinsic PC. Three-dimensional simulation results exhibit less clear and sharp resonances in the band-gap region, compared to the two-dimensional counter-part. This is expected as in-plane wavevector reduction is not an issue in two-dimensional simulations.

Mode simulations have been performed for both two- and three-dimensional PCRR structures. Result trends are as expected when considering reduction in Q-factor from two- to three-dimensional simulations, and from air substrate to silica substrate. The Q-factor trends across design solutions behave inconsistently from two- to three-dimensional simulations. The inconsistency may possibly be explained by various amount of small in-plane wavevector components across design solutions. No investigation into this theory has been made. The truncated design solution achieved the highest Q-factor for three dimensional simulations where the substrate is simulated as silica. Design solution combinatorics has not shown any improvement in light confinement over an ordinary PCRR. Optimizing only a corner of a PCRR and expanding the best solution to a complete PCRR has not performed as intended. More sophisticated optimization tools for FDTD software exists. Meep launched an adjoint class in late April 2019, but too many issues with the release prevented it from being used in the thesis work.

5.3 Fabrication

The fabrication section of the results is dominantly based on SEM-images. SEM-images are therefor not covered in its own section. During the fabrication process SEM-images have been taken to document EBL exposure and development, and etch results. Fabrication results are presented in the same chronological order as they were presented in Chapter 4. Exposure and development challenges, and means to improve those challenges are presented in Subsection 5.3.1. Etch results for both waveguides and photonic crystals are presented in Subsection 5.3.2. Inverted tapers are covered separately in Subsection 5.3.3. At last fabrication results are summarized in Subsection 5.3.4.

5.3.1 Lithography and Development

Lithography and development has been performed in accordance with the recipe provided in Chapter 4. Some variation in process results has been detected. Steps found to be critical for good results are soft bake, stable electron gun during EBL exposure, and a development process performed exactly as described in Chapter 4.

Figure 5.15 is a SEM-image of an etch and resist stripped sample.
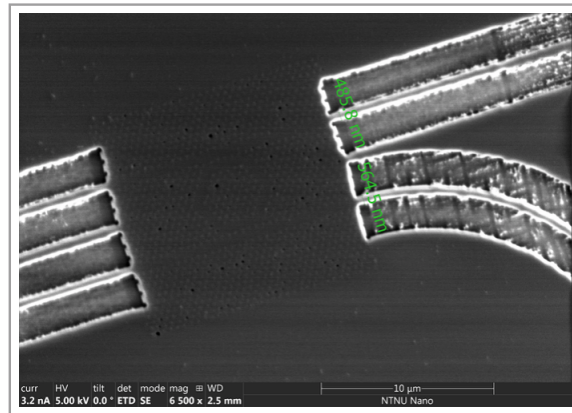
Figure 5.15: SEM-image of an etched and resist stripped sample. Approximate slab waveguide width is marked in green as 485.8 nm and 564.6 nm for the straight waveguide and curved waveguide, respectively. A PC structure is barely visible and the hole uniformity is poor.

Figure 5.15 illustrates a case of poor exposure dose during exposure and poor input file design. The dose time has been too small, resulting in un-etched or barely etched PC holes. A small dose time results in a small exposure dose. Slab waveguides exhibit poor uniformity. Etch depth on both sides of the waveguides is clearly not uniform as it varies in different shades of grey. The curved waveguide exhibits lines constituting squares in the surrounding etched areas. Square shaped etching is an artifact from poor GDS-file management. When structures are designed in a GDS-file supporting software, curved designs are often produced by smaller rectangular shapes. Curved shapes can be smoothened before exposure, eliminating any unintended squares. This has not been done with the design in Figure 5.15, resulting in deeper etched lines. These lines are not necessarily a problem, but when they interfere with the slab waveguide they produce unintended variations in waveguide width.
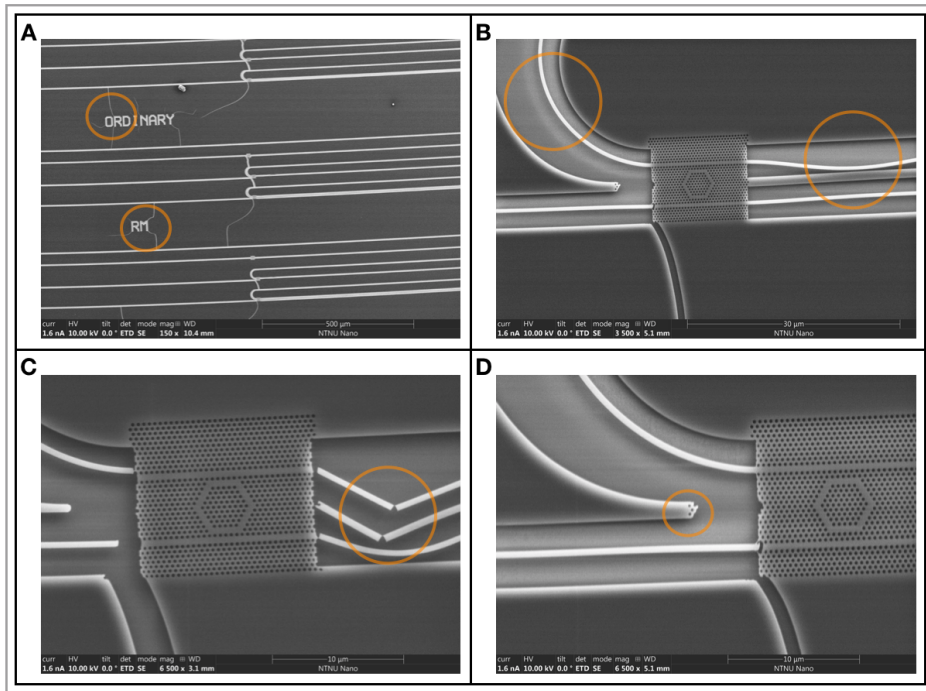
Figure 5.16: SEM images illustrating a case of badly performed development. Figure **A** is a macroscopic image showing exposed and developed ordinary and rm designs. Figures **B**, **C**, and **D** illustrate a PCRR structure with coupling to PC waveguide and slab waveguide. All four images are captured from the same sample. Yellow circles are points of interest.

Figure 5.16 are SEM-images captured from a sample subject to poor development. Figure A is a macroscopic image showing exposed and developed ordinary and rm designs. Cracks in the resist are visible in high spatial gradient areas, and are highlighted with yellow circles. Such cracks can occur if the sample experience an high temperature gradient during soft bake [6]. Resist cracks are usually not a problem as they tend to occur in areas where they do not affect device performance. Figure B, C, and D illustrate waveguide bending, waveguide breaking, and shift in PC location. The cause of bending, breaking and shifts are somewhat uncertain. The main hypothesis is poor development. The sample imaged in Figure 5.16 was subject to the following development procedure:

"**Development:** The sample is immersed and lightly agitated in the developer for 60 s. The sample is transferred to a beaker containing development stopper for 30 s, and finally to a beaker with de-ionized water for 30 s."

This development procedure was formerly used within the LOC project [26][27][25]. Similar results to that illustrated in Figure 5.16 has been experienced by other LOC project participants when applying the development procedure described above. LOC project participants have later switched to the development procedure described in Chapter 4. The

resist is believed to contract in both x and y directions when immersed in de-ionized water. To relieve stress it cracks in certain areas (as seen in Figure C). As a result of the shrinking and cracking larger areas of resist opens up and are free to move around. Areas of interest in Figures B and D are believed to be resist areas that have moved during development. Figure 5.17 illustrates the case where the development procedure in Chapter 4 has been followed.
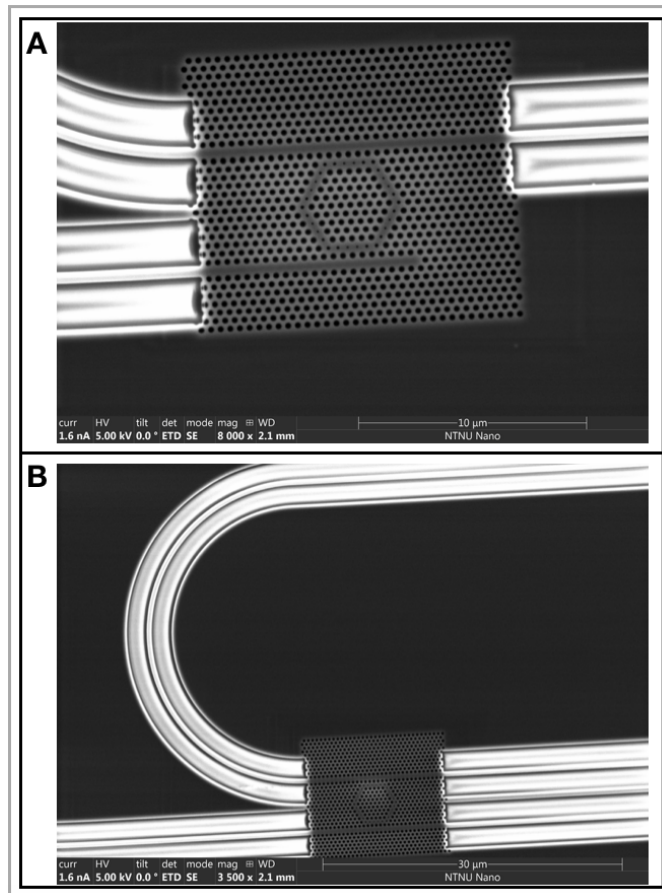
Figure 5.17: SEM-images illustrating the results of a well performed development process. SEM-images show no sign of resist cracks, waveguide bending, or waveguide cracking.

The problems illustrated in Figure 5.16 are not present in Figure 5.17. The waveguides are uniform and smooth without any indication of breaking. There is also no resist cracks at points with a high spatial gradient (as seen in the bottom of Figures 5.16 B, C, and D). Structures with development results similar to that illustrated in Figure 5.17 have been categorized as good enough to proceed to etching.

5.3.2 Etching

Etching is performed by an ICP-RIE instrument as described in Table 4.5, Chapter 4. The etching duration can be varied. Figure 5.18 illustrates two different samples subject to different etch duration. Macroscopic versions of the images captured in Figure 5.18 are offered in Appendix G.
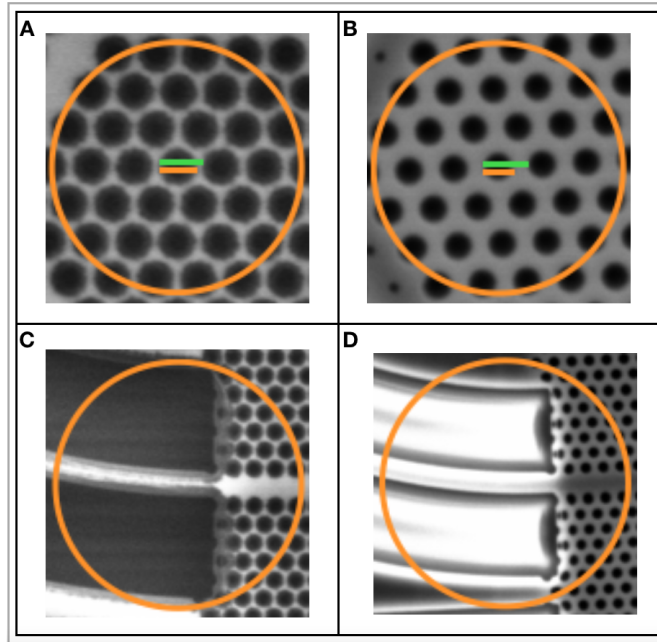
Figure 5.18: Four SEM-images of two different samples are illustrated. Figures **A** and **C** represent a sample etched for 77 seconds. Figures **B** and **D** represent a sample etched for 47 seconds. Yellow circles represent points of interest. The yellow and green lines captures hole diameter and lattice constant, respectively.

Figure 5.18 illustrates four SEM-images of two different samples. Figures A and C represent a sample etched for 77 s. Figures B and D represent a sample etched for 47 seconds. Yellow circles represent points of interest. The yellow and green lines captures hole diameter and lattice constant, respectively. The green line in Figures A and B are both approximately 420 nm. The yellow line in Figures A and B are approximately 335 and 215 nm, respectively. With the measured diameters and lattice constants an etch duration of 77 s has produced an air-hole radius of 0.40a. Air-hole radius of 0.25a is the result of an etch duration of 47 s. An air-hole radius of 0.25a is desirable for transmission measurements as it matches the tunability of the laser. An air-hole radius of 0.40a results in a dispersion relation converging towards a band-gap illustrated in Figure 5.4, B. Such a dispersion relation exhibits a larger and blue-shifted band-gap, as a consequence of a higher air content in the crystal [31]. The dispersion relation also flattens, causing a reduction in group velocity. When the group velocity is considerably reduced the dispersion relation between a

line defect in PC and a strip waveguide becomes unmatched [28]. For the sample etched in 77 s the waveguide is (as seen in Figure C) over-etched. A clear thin ridge is identified within the yellow circle, indicating an increase in etching with increasing distance from waveguide center. The waveguide geometry changes as a result of over-etching. A change in geometry highly affects the dispersion relation, causing the dispersion relation to deviate from the simulations in Figure 5.7, B.

Another concern is the scattering loss from the etch imperfections. Both Figures 5.18 A and B exhibit more surface roughness at air-hole sites and along the waveguide. Scattering loss from such imperfections highly impact transmission measurements as the scattered light propagates of into the silicon slab.

5.3.3 Inverted Tapers

As explained in Chapter 2, adding a polymer waveguide layer on top of an inverted tapered silicon slab waveguide can reduce loss when coupling light from an external source. Figure 5.19 are images taken with an optical microscope with magnification steps 5x, 10x, 20x, 50x, and 100x.
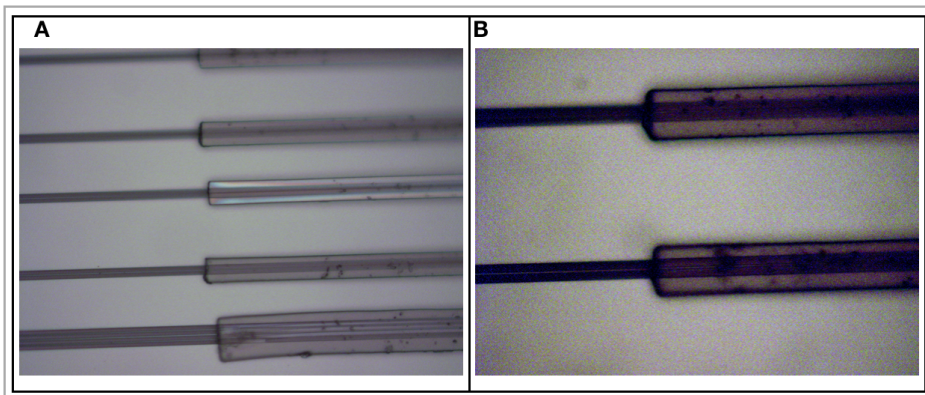
Figure 5.19: Images of inverted tapers captured with an optical microscope. Figures **A** and **B** represent the same inverted tapers. The magnification in Figures **A** and **B** are 20x and 100x, respectively.

The polymer layer is deposited from where the silicon waveguide tapering begins to the end of the sample. The silicon waveguides are produced by etching a 2 μm wide strip on each side of a 550 μm wide slit. The darker areas seen in the optical microscope images are the 2 μm wide etched areas. The waveguide itself is barely visible in the bottom waveguide of each image.

The polymer waveguides extend the etched areas. Extending the etched areas allows light to couple out to the silicon slab. Light that does not couple directly into the inverted tapered silicon waveguide is confined by the polymer waveguide. Since the polymer waveguide overlaps the slab silicon layer light can couple out. When fabricating new LOC devices polymer waveguide layer should be designed to only overlap the inverted tapered silicon waveguide.

5.3.4 Fabrication Summary

PCRRs that exhibit measurable transmission resonances in a drop-filter transmission setup have been fabricated. Steps in the lithography and development process found to be critical were soft bake, stable electron gun during EBL exposure, and a development process only using developer and developer stopper. Documentation of exposure and development when de-ionized water is used for rinsing after development are presented. Introduction of de-ionized water is believed to produce resist cracks and resist movement. Development process only using developer and developer stopper show no indication of resist cracking and resist movement.

Etching results from samples etched in 47 and 77 s are presented. 77 s of etching results in a hole radius of 0.40a. Waveguides become over-etched for longer etch duration, rendering an unintended geometrical configuration. An etch duration of 47 s resulted in a hole radius of 0.25a.

Inverted tapers have been produced on a-Si samples. The inverted tapers where designed to extend etched areas constituting the strip waveguides. By extending the etched areas the inverted tapers overlap slab areas allowing light to couple out into the slab. For further fabrication the design should be changed to prevent light coupling out into the slab.

5.4 Characterization

Characterization of fabricated devices is performed by transmission measurements. Transmission measurement setup is described in Chapter 4. Measurements have been performed on straight waveguides, line defects, and all PCRR design solutions. PCRR measurements presented are result of a drop-filter transmission setup. Measurements have been performed for devices with c-Si, a-Si, and a-Si with inverted tapers as active layer.

5.4.1 Transmission Measurements

Figure 5.20 illustrates the measured transmission spectrum for a straight waveguide on a device with c-Si as the active layer.
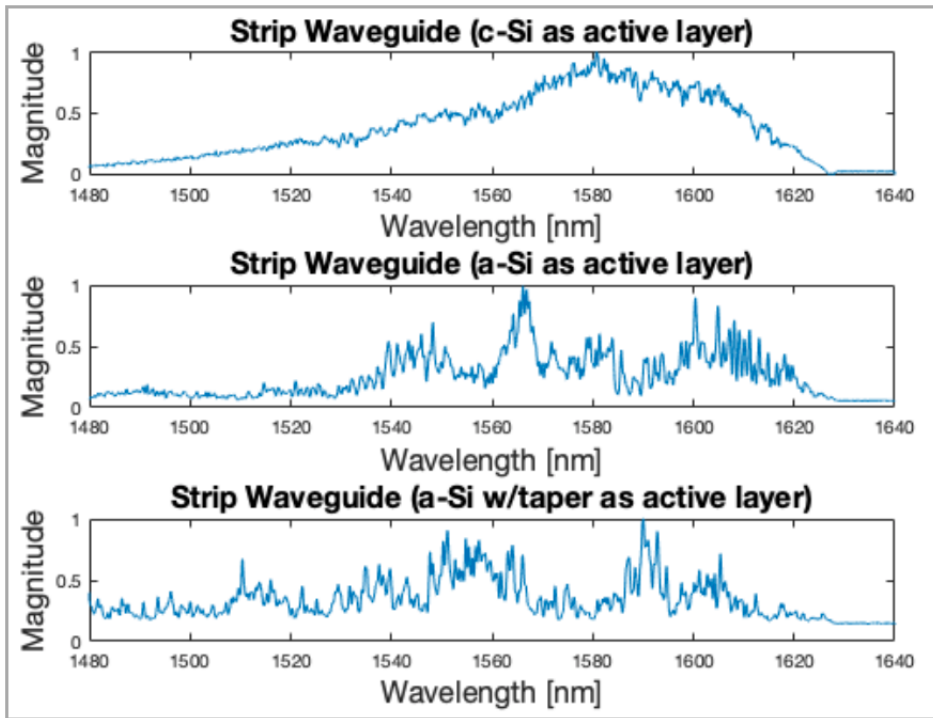
Figure 5.20: Transmission spectra for strip waveguides. The top spectrum represents the case where c-Si is the active layer. The middle spectrum represents the case where a-Si is the active layer. The bottom spectrum illustrates the case where a-Si with inverted tapers is the active layer. All spectra are normalized to unity.

Transmission spectra for strip waveguides vary significantly from c-Si to a-Si as active layer. Spectrum representing a c-Si strip waveguide resembles more the tunable laser intrinsic spectrum (see Appendix H) than the other two spectras. Visual observations as measurements were performed suggests more scattering when testing a-Si and a-Si with inverted taper devices. Transmission measurements support the visual observations as more frequency components have not transmitted through both the a-Si devices, when compared to the c-Si device. Loss associated with the intrinsic properties of a-Si is possible. As covered in Chapter 3, a-Si exhibits more dangling bonds and defects than c-Si. Dangling bonds and symmetry disorders cause light to scatter. Higher degree of surface roughness in a-Si grown thin films has also been reported [26]. Because of the structural disorder in a-Si the amount of energy required to etch away one atom varies significantly more for a-Si than for c-Si. These are all possible explanations to why the a-Si devises exhibit less transmitted frequency components in their spectras for strip waveguides. Light escaping to the slab for a-Si with inverted tapers was visually observed, confirming a suggested problem with the design in Subsection 5.3.3.

Figure 5.21 illustrates the measured transmission spectra for line defects.
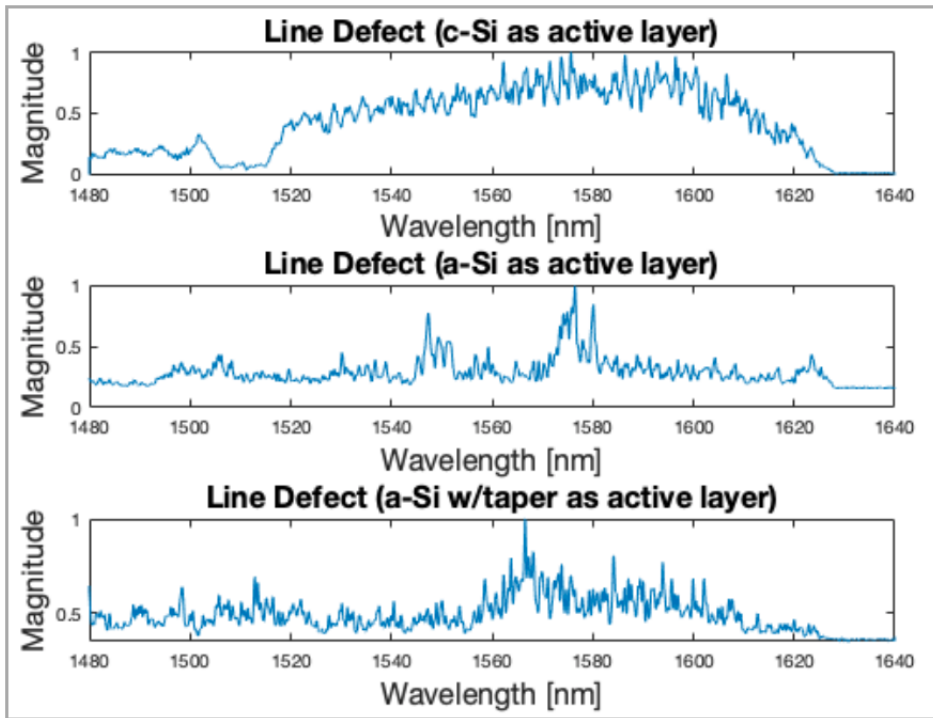
Figure 5.21: Transmission spectra for line defects. The top spectrum represents the case where c-Si is the active layer. The middle spectrum represents the case where a-Si is the active layer. The bottom spectrum illustrates the case where a-Si with inverted tapers is the active layer. All spectra are normalized to unity.

Transmission spectra for line defects follow the same trend as transmission spectra for strip waveguides. Line defect transmission spectra for c-Si resembles the spectra of c-Si strip waveguide, except for the wavelength band from 1500 to 1520 nm. The photonic crystal appears to exhibit a small band-gap with no guided modes in the 1500-1520 wavelength band. Such a band-gap is not comparable to the simulated band-gaps. The tunable laser can cover the wavelength region 1480 to 1640 nm. With a lattice constant of 420 nm those wavelengths correspond to normalized frequencies 0.2837 and 0.2561, respectively. Only a portion of the PC band-gap can therefor be measured with the tunable laser. The spectras for both a-Si line defects exhibits some transmission in the wavelength range 1550 to 1560 nm. The spectras for a-Si devices do not align with the strip waveguide spectras in any clear way.

Transmission measurements have been performed on all PCRR design solutions for all variations of active layer. Only measurements performed on c-Si PCRRs are presented here as too much noise was detected on a-Si PCRRs to offer any insight. Visible detection of light coupling to the drop-filter waveguide was not possible for any of the a-Si PCRRs.

Figures 5.22 and 5.23 illustrates spectra for all design solutions. The spectra are targeted for transmission peaks visually verified to be transmitted through a drop-filter trans-

mission setup. Orange lines indicate transmission peaks for which Q-factor has been calculated.
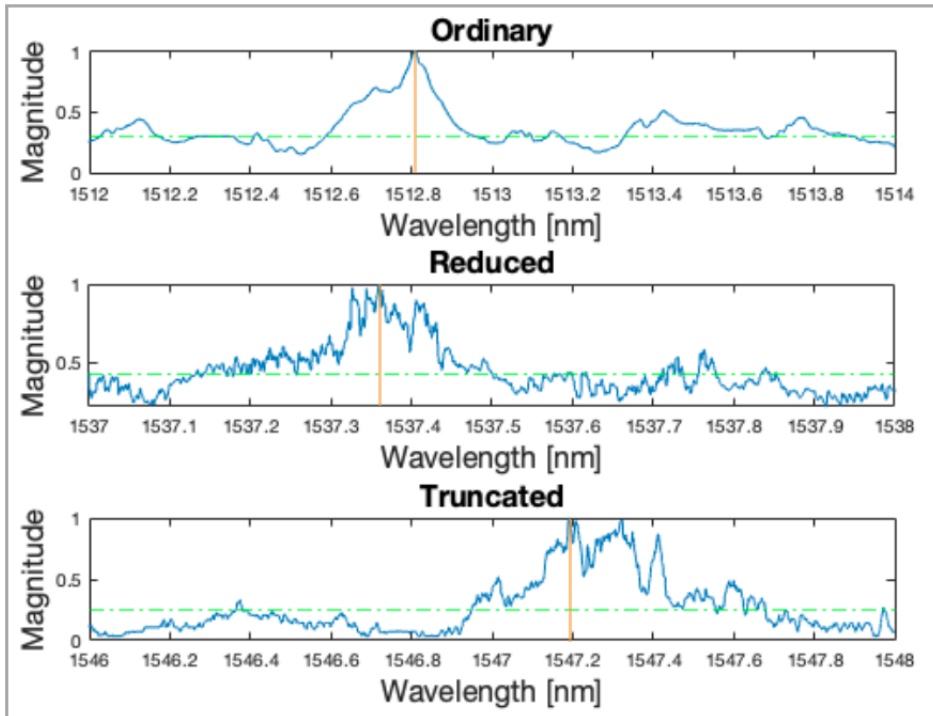
Figure 5.22: Transmission measurements focused in on most prominent frequency component for design solutions ordinary, reduced, and truncated. The wavelength resolution varies from spectrum to spectrum.

The green lines in Figures 5.22 and 5.23 indicate the spectra mean value. It is included to offer an indication of how distinct any transmission peak is, compared to the rest of the transmission spectra. There are several transmission peaks in the spectra. The wavelength range from spectrum to spectrum varies. The wavelength range is kept small to substantiate resolution of detected resonances. Spectra for the wavelength range 1500-1550 nm are offered in Appendix I.
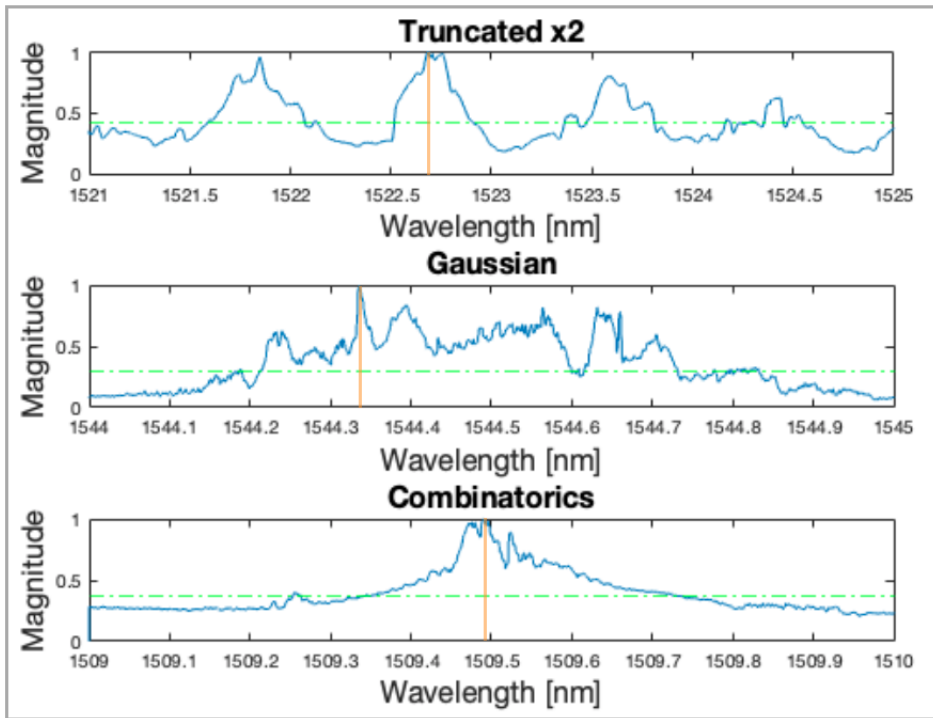
Figure 5.23: Transmission measurements focused in on most prominent frequency component for design solutions truncated x2, gaussian and combinatorics. The wavelength resolution varies from spectrum to spectrum.

The gaussian design exhibits the sharpest resonance mode in the 1500-1550 nm wavelength range. The resonance mode is found in Figure 5.23 at a center wavelength of 1544.35 nm. Table 5.2 presents the resulting Q-factor from the marked transmission peaks in Figures 5.22 and 5.23.

Design Solution	Q-factor
Ordinary	5042
Reduced	7687
Truncated	5157
Truncated x2	5075
Gaussian	25739
Combinatorics	10063

Table 5.2: Table of the calculated Q-factors for the most prominent frequency components in Figures 5.22 and 5.23.

Q-factor values presented in Table 5.2 are calculated using Equation 2.48. The Gaussian design achieved the highest Q-factor value for c-Si active layer devices. Stating that these Q-factor defines the PCRRs would be misleading. The transmission measurement setup is incapable of measuring the whole band-gap region of the devices. The spectra offered in Section 5.4 do not offer any insight beyond the wavelength range they cover. The Q-factor values presented in Table 5.2 can only verify that the PCRRs exhibit resonant modes within the wavelength range 1480-1640 nm. The resonant modes themselves indicates that the PCRR have coupled modes from the strip waveguides and line defects. Observed resonant modes support theory provided in Chapter 2 and simulation results in Section 5.2. The overall measured Q-factors coincides well with Q-factor values from three-dimensional mode simulations where the substrate is simulated as silica. Design solutions gaussian and combinatorics have achieved higher Q-factor values for fabricated devices than their simulated counterpart.

5.4.2   Characterization Summary

Strip waveguides, line defects, and all PCRR design solutions have been measured in the transmission measurement setup described in Chapter 4. Transmission measurements for strip waveguides fabricated in c-Si coincides with the tunable laser bandwidth profile. So does the line defects fabricated in c-Si. a-Si transmission spectra for strip waveguide and line defects indicate more loss compared to c-Si devices. Visual observations while

transmission measurements were performed substantiates the loss reasoning of the transmission spectra. Visual observation of light coupling to the substrate for inverted taper design confirms the problem addressed in Subsection 5.3.3.

Transmission measurements on PCRRs are only presented for c-Si active layer devices. The PCRRs were investigated for resonant modes in the wavelength range 1480-1640 nm, only wavelength range 1500-1550 nm is presented in the thesis. Transmission measurements clearly exhibit resonant modes in the wavelength region 1500-1550 nm. The most distinct resonant mode was achieved for the gaussian design solution. A Q-factor value of 25739 was recorded for the gaussian design. The average recorded Q-factor value coincides with simulation results for three-dimensional mode simulations where the substrate is simulated as silica.

6. Conclusion

The goal of this thesis work has been to optimize PCRRs for biosensing applications, both by simulating optimization suggestions and by fabrication.

Simulations

Computer simulations in this thesis work have consisted of FDS and FDTD simulations of PC structures, with resulting dispersion relations, transmission spectra, and resonant mode information for the respective structures . Simulations have been performed in two and three dimensions. Three-dimensional simulations are more resource demanding and have therefor been run on Fram, a super computer. Various PCRR configurations have been designed to optimize for Q-factor. Structural components essential for a well performing PCRR have been investigated as stand alone devices. Such components are strip waveguides and line defects in PC.

Strip waveguides and line defects in PC were simulated in both two and three dimensions. Guided modes were found to coincide across stand alone devices. PCRRs were transmission and mode simulated in both two and three dimensions. For three-dimensional simulations the substrate layer was simulated as both silica and air. Transmission simulation were found to coincide well with resulting dispersion relations from FDS simulations. Q-factor values from mode simulations exceeded 1×10^8 for two-dimensional simulations. A reduction in Q-factor for three-dimensional simulations was detected. Air substrate simulations exceeded Q-factor values of 5×10^4, while silica substrate simulations exceeded Q-factor values of 4000. The PCRR design "gaussian" achieved the highest Q-factor value for silica simulated substrate devices. The recorded Q-factor value was 4286.

Q-factor trends when comparing two- and three-dimensional simulations, as well as substrate varying three-dimensional simulations are supported by FDTD transmission and FDS dispersion simulations. Three-dimensional simulations experience in-plane wavevector reduction as wavevector components propagate through the simulated structures. Small in-plane wavevector components can couple to the substrate if they are smaller than the substrates corresponding lightcone wavevector. The corresponding lightcone wavevector is larger for silica substrate than for air substrate. More loss is therefor expected in three-dimensional, and especially three-dimensional silica substrate simulations compared to two-dimensional simulations. FDS and FDTD simulation software has been a powerful tool to understand PC devices.

Fabrication

Main processes used for fabricating PC structures where thin film deposition using PECVD, lithography patterning with EBL, and etching with ICP-RIE. Inverted tapers were produced using MLA. An exposure dose and beam current of 350 μC/cm^2 and 1 nA gave the best exposure results, respectively. The development process was found to be sensitive to error. A development procedure containing only developer and developer stopper was found to produce better sample development than previous development procedures including de-ionized water.

An etch time of 47 s was found to be favourable for producing air-hole radius matching the wavelength range of the laser in the transmission measurement setup. The air-hole radius corresponding to 47 s etch duration was measured to 0.25a, a representing the lattice constant. Etch duration of 77 s produced a measurable air-hole radius of 0.4a. The air-holes and strip waveguides subject to 77 s etch duration exhibited more surface roughness and waveguide deformation.

Inverted tapers where found to exhibit design flaws. They extended etched areas constituting strip waveguides. By extending the etched areas the tapers came in contact with the surrounding slab, allowing light to couple out into the slab.

Characterization

Transmission measurements were performed on fabricated devices. Measurements were performed on strip waveguides, line defects in PC, and PCRR structures. Structures fabricated in a-Si were found to suffer from more scattering loss than c-Si devices. Only c-Si devices showed detectable resonances for PCRRs in a drop-filter transmission setup. PC structures were transmission measured in the wavelength range 1480-1640 nm. The range does not cover the whole band-gap of a PCRR structure. The resulting Q-factor values can therefor not define the performance of the respective PCRR structure beyond the wavelength range investigated. Resonant modes were detected for all PCRR design solutions, with the gaussian design achieving the highest Q-factor value of 25739.

Future Work

There is much simulation and fabrication work that can be done to build upon this thesis. Listed below are the next steps I consider to be most important for PCRR design for label-free biosensing purposes.

- Mode and transmission simulations involving optimization wrappers such as Meep Adjoint. Such wrappers can optimize structures based on user defined functions, allowing structures to be optimized with a clear physical reasoning.

- Testing the produced PCRRs with coated biolayer to see how they perform as intended application.

- Under-etching the PCRRs to support more lateral light confinement.

- Setting up a transmission measurement lab allowing to transmission test the PCRRs across the whole band-gap.

Bibliography

[1] Meep, 2018-12-11. https://meep.readthedocs.io/en/latest/.

[2] Mpb, 2018-12-11. https://mpb.readthedocs.io/en/latest/.

[3] Robert Adams and Christopher Essex. *Calculus: A Complete Course, Eighth Edition*. Pearson Education Canada, 2013.

[4] V Ebnali-Heidari M Afzal, S Ahmadi. All-optical tunable photonic crystal nor gate based on the nonlinear kerr effect in a silicon nanocavity. *Journal of the Optical Society of America B: Optical Physics*, 30(9):2535–2539, 2013.

[5] Yoshihiro Akahane, Takashi Asano, Bong-Shik Song, and Susumu Noda. High-q photonic nanocavity in a two-dimensional photonic crystal. *Nature*, 425:944–947, 2003.

[6] Stephan S Heiskanen Arto Dimaki Maria Emnus Jenny Boisen Anja Tenje Maria Amato, Letizia Keller. Fabrication of high-aspect ratio su-8 micropillar arrays. *Microelectronic Engineering*, 98:483–487, 2012.

[7] Martijn J R John Demis D Barton Jonathon S Bruinink Christiaan M Leinse Arne Heideman Ren G Blumenthal Daniel J Bowers John E Bauters, Jared F Heck. Planar waveguides with less than 0.1 db/m propagation loss fabricated with wafer bonding. *Optics Express*, 19(24), 2011.

[8] Robert W. Boyd. *Nonlinear Optics, third edition*. Elsevier Science Publishing Co Inc, 2008.

[9] Hans-Georg Braun. *Electron beam lithography*. PhD thesis, Technical University Dresden, 2008.

[10] Stefano Morichetti Francesco Ferrari Carlo Hu Juejun Musgraves J David Richardson Kathleen Agarwal Anu Kimerling Lionel C Melloni Andrea Canciamilla, Antonio Grillanda. Photo-induced trimming of coupled ring-resonator filters and delay lines in as2s3 chalcogenide glass. *Optics letters*, 36(20), 2011.

[11] David K. Cheng. *Field and Wave Electromagnetics; 2nd ed.* Pearson, 2014.

[12] T R Richardson D Donval A Oron R Oron M Choudhury, A.N.M.M Stanczyk. Method of improving light coupling efficiency between optical fibers and silicon waveguides. *IEEE Photonics Technology Letters*, 17(9):1881–1883, 2005.

[13] T Fennell, P P Deen, A R Wildes, K Schmalzl, D Prabhakaran, A T Boothroyd, R J Aldus, D F McMorrow, and S T Bramwell. Magnetic coulomb phase in the spin ice ho2ti2o7. *Science*, 326(5951):415–417, 2009.

[14] Halvor Fergestad. Optimization of photonic crystal ring resonators for lab-on-a-chip applications, 2018.

[15] Center for Nanoscale Science & Technology. Oxford plasmalab system 100 multipurpose plasma etcher users manual, 2019-06-06. https://www.nist.gov/sites/default/files/documents/2017/05/09/Oxford_PlasmaLab_MultipurposeEtche _2_USERMANUAL_v1.pdf.

[16] L H Frandsen, A Harpth, P I Borel, M Kristensen, J S Jensen, and O Sigmund. Broadband photonic crystal waveguide 60 bend obtained utilizing topology optimization. *Optics Express*, 12(24):5916–5921, 2004.

[17] H. Weber G. Arfken and F. Harris. *Mathematical Methods for Physicists: a Comprehensive Guide; 7th edition*. Academic Press, 2013.

[18] Yaoyu Evans Richard A Gu Min Gan, Zongsong Cao. Three-dimensional deep sub-diffraction optical beam lithography with 9nm feature size. *Nature Communications*, 4(3):1, 2013.

[19] Yordan Holmes Justin Gangnaik, Anushka Georgiev. New generation electron beam resists: A review. *Chemistry of Materials*, 29, 2017.

[20] David A Gay. *Explorations in topology : map coloring, surfaces, and knots*. Elsevier, 2014.

[21] Øyvind Grøn. Andre marie ampere, 2018-11-22. https://snl.no/André_Marie_Ampère.

[22] Øyvind Grøn. Magnetisk monopol, 2018-11-22. https://snl.no/magnetisk_monopol.

[23] Øyvind Grøn. Michael faraday, 2018-11-22. https://snl.no/Michael_Faraday.

[24] T R Groves. *Nanolithography*. Woodhead Publishing, 2014.

[25] Ingerid Gjeitnes Hellen. Simulation and fabrication of two-dimensional photonic crystal drop filters for biosensing, 2018.

[26] Lars Grnmark Holmen. Simulation and fabrication of a photonic crystal mach-zehnder interferometer, 2016.

[27] Jens Høvik. Photonic crystal waveguide fabrication, 2012.

[28] L Young Jeff F Sipe J E Hughes, S Ramunno. Extrinsic optical scattering loss in photonic crystal waveguides: role of fabrication disorder and photon group velocity. *Physical review letters*, 94(3), 2005.

[29] NTNU Institute of Mathematics. *Differential Equations, Linear Algebra and Its Applications, Second Edition*. Pearson, 2012.

[30] National Instruments. Labview, 2019-06-09. https://www.ni.com/en-us/shop/labview.html.

[31] John D. Joannopoulos, Steven G. Johnson, Joshua N. Winn, and Robert D. Meade. *Photonic Crystals: Molding the Flow of Light (Second Edition)*. Princeton University Press, 2008.

[32] J Johnson, S Joannopoulos. Block-iterative frequency-domain methods for maxwell's equations in a planewave basis. *Optics express*, 8(3), 2001.

[33] Steven G. Johnson. The mit photonic-band manual, 2018-12-11. http://ab-initio.mit.edu/mpb/doc/mpb.pdf.

[34] Erwin Kreyszig. *Advanced Engineering Mathematics: International Student Version; 10th edition*. John Wiley and Sons, 2011.

[35] C Nava R Trejo-Valdez M Reyes-Esqueda J A la Mora, M B Torres-Torres. Photoluminescent logic gate controlled by the optical kerr effect exhibited by porous silicon. *Optics and Laser Technology*, 59, 2014.

[36] Stefan Landis. *Lithography*. John Wiley & Sons, 2010.

[37] P I Frandsen L H Thorhauge M Harpth A Kristensen-M Niemi T Chong H M H Lavrinenko, A Borel. Comprehensive fdtd modelling of photonic crystal waveguide components. *Opt. Express*, 12:2061, 2004.

[38] S-Y Lin, E Chow, V Hietala, P R Villenueve, and J D Joannopoulos. Experimental demonstration of guiding and bending of electromagnetic waves in a photonic crystal. *Science*, 282(5387):274–276, 1998.

[39] Xiaolong Chakravarty Swapnajit Lee Beom Suk Lai Wei-Cheng Chen Ray T Lin, Che-Yun Wang. Wideband group velocity independent coupling into slow light silicon photonic crystal waveguide. *Applied Physics Letters*, 97(18), 2010.

[40] Yingbai Pun Edward Y B Jin Goufan Lu, Si Yan. Very low-loss fiber-to-waveguide coupling using diffraction optical element mode converter. *SPIE*, 4904, 2002.

[41] V A Mandelshtam and H S Taylor. Harmonic inverion of time signals. *J. Chem. Phys.*, 107(17):6756–6769, 1997.

[42] X.-C Karis Tom Deng Hong Dai Qing Burns-Jana Waltman Robert Marchon, Bruno Guo. Fomblin multidentate lubricants for ultra-low magnetic spacing. *Magnetics, IEEE Transactions on*, 42:2504–2506, 2006.

[43] Peter M. Martin. *Handbook of Deposition Technologies for Films and Coatings : Science, Applications and Technology*. Elsevier Science & Technology Books, 2009.

[44] James Clerk Maxwell. *Treatise on Electricity and Magnetism, Vol. 1*. Dover Publications; 3rd ed. edition (June 1, 1954), 1954.

[45] C McGuinness, R L Byer, E Colby, B M Cowan, R J England, R J Noble, T Plettner, C M Sears, R Siemann, J Spencer, and D Waltz. Woodpile structure fabrication for photonic crystal laser acceleration. *AIP Conference Proceedings*, 1086(1):544–549, 2009.

[46] Nikolaj Vlasov Yurii Mcnab, Sharee Moll. Ultra-low loss photonic integrated circuit with membrane-type photonic crystal waveguides. *Optics Express*, 11(22), 2003.

[47] Takuji Nakagawa Miyamoto, Keisuke Kageyama, Hiroshi Takagi, Yukio Sakabe, Soshu Kirihara, and Yoshinari. Diamond-structure photonic crystals composed of ceramic spheres in resin and their microwave properties. *Japanese Journal of Applied Physics*, 46(105):7117, 2007.

[48] Karthik Narayanan. *Hydrogenated amorphous silicon photonics*. PhD thesis, Rochester Institute of Technology, 2011.

[49] Robert E. Newnham. *Properties of Materials: Anisotropy, Symmetry, Structure; 1st ed*. Oxford, 2005.

[50] NKTPhotonics. Photonic crystal fibers, 2018-12-10. https://www.nktphotonics.com/lasers-fibers/product-category/photonic-crystal-fibers/.

[51] David Ibanescu Mihai Bermel Peter Joannopoulos J D Johnson Steven G Oskooi, Ardavan F Roundy. Meep: A flexible free-software package for electromagnetic simulations by the fdtd method. *Computer Physics Communications*, 181(3):687–702, 2010.

[52] Xiao Pei. The monte carlo simulation of secondary electrons excitation in the resist pmma. *Applied Physics Research*, 6(3):1, 2014.

[53] Michael Quirk and Julian Serda. *Semiconductor Manufacturing Technology*. Pearson, 2001.

[54] K et al. Rauscher. Improved transmission for 60 photonic crystal waveguide bends. *Progress in Electromagnetic Research Symposium*, 2004.

[55] Bahaa E A Saleh and Malvin Carl Teich. *Fundamentals of photonics; 2nd ed.* Wiley, 2007.

[56] Wolfgang Hofmann Holger Hfling Sven Forchel Alfred Semmel, Julia Kaiser. Single mode emitting ridge waveguide quantum cascade lasers coupled to an active ring resonator filter. *Applied Physics Letters*, 93(21), 2008.

[57] Xiankai Henry M David Yariv Amnon Scherer Axel Shearn, Michael Sun. *Semiconductor Technologies*. IntechOpen, 2010.

[58] I I Shishkin, K B Samusev, M V Rybin, M F Limonov, Yu. S Kivshar, A Gaidukeviciute, R V Kiyan, and B N Chichkov. Inverted yablonovite fabricated by the direct laser writing method and its photonic structure. *JETP Letters*, 95(9):457–461, 2012.

[59] Ivan Shishkin, Kirill Samusev, Mikhail Rybin, Mikhail Limonov, Yuri Kivshar, Arune Gaidukeviciute, Roman V. Kiyan, and Boris Chichkov. Inverted yablonovite-like 3d photonic crystals fabricated by laser nanolithography. *Proc SPIE*, 8425:51, 2012.

[60] Jessica Steinlechner, Christoph Krger, Nico Lastzka, Sebastian Steinlechner, Alexander Khalaidovski, and Roman Schnabel. Optical absorption measurements on crystalline silicon test masses at 1550 nm. *Classical and Quantum Gravity*, 30(9), 2013.

[61] Shoko Omoda Emiko Sakakibara Youichi Mori Masahiko Kamei Toshihiro Takei, Ryohei Manako. Sub-1 db/cm submicrometer-scale amorphous silicon waveguide for backend on-chip optical interconnect. *Opt. Express*, 22(4):4779–4788, 2014.

[62] Yoshinori Tanaka, Takashi Asano, and Susumu Noda. Design of photonic crystal nanocavity with q-factor of $\sim 10^9$. *Journal of Lightwave Technology*, 26(11):1532–1539, 2008.

[63] Junfeng Fang Q Yu M B Lo G Q Kwong D L Tao, S H Song. Improving coupling efficiency of fiber-waveguide coupling with a double-tip coupler. *Opt. Express*, 16(25):20803–20808, 2008.

[64] L Vigen. Silicon racetrack resonator., 2014.

[65] L. Vivien and L. Pavesi. *Handbook of silicon photonics*. Tayler & Francis, 2013.

[66] John Wallace. Light-emitting diodes: Photonic-crystal led has high extraction efficiency, 2018-12-10. https://www.laserfocusworld.com/articles/2009/06/light-emitting-diodes-photonic-crystal-led-has-high-extraction-efficiency.html.

[67] Jonathan Wierer. Iii-nitride photonic-crystal light-emitting diodes with high extraction efficiency. *Nature Photonics*, 3(3):163–169, 2009.

[68] Eli Yablonovitch. Inhibited spontaneous emission in solid-state physics and electronics. *Physical Review Letters*, 58(20):2059–2062, 1987.

[69] Amnon Yariv and Pocji Yeh. *Photonics: optical electronics in modern communications; 6th ed.* Oxford Univ., 2006.

[70] Brandon Wang Cheng Shams-Ansari Amirhassan Reimer Christian Zhu Rongrong Kahn Joseph M Lonar Marko Zhang, Mian Buscaino. Broadband electro-optic frequency comb generation in a lithium niobate microring resonator. *Nature*, 568(7752), 2019.

[71] Yong Zhang, Cheng Zeng, Danping Li, Ge Gao, Zengzhi Huang, Jinzhong Yu, and Jinsong Xia. High-quality-factor photonic crystal ring resonator. *OPTICS LETTER*, 39(5), 2014.

Appendix

A   MPB Code For Intrinsic PC

Python code below runs a MPB simulation for a three dimensional slab intrinsic photonic crystal. It calculates the dispersion relation at user defined wavevector k-points. The code below calculates for k-points along the IBZ proximity. It has produced the dispersion relation in Figure 5.8 A.

```python
import math
import meep as mp
from meep import mpb

h = 0.55  # the thickness of the slab
eps = mp.Medium(index=3.45)  # the dielectric constant of the slab
loweps = mp.Medium(index=1.00)  # the dielectric constant of the substrate
s = 2.0
r = 0.3  # the radius of the holes
supercell_h = 4  # height of the supercell

# triangular lattice with y−directional supercell:
geometry_lattice = mp.Lattice(size=mp.Vector3(1, 1, supercell_h),
                              basis1=mp.Vector3(math.sqrt(3) / 2, 0.5),
                              basis2=mp.Vector3(math.sqrt(3) / 2, −0.5))


#setting the geometry
geometry = [
    mp.Block(material=loweps, center=mp.Vector3(z=0.25 * supercell_h),
             size=mp.Vector3(mp.inf, mp.inf, 0.5 * supercell_h)),
    mp.Block(material=eps, size=mp.Vector3(mp.inf, mp.inf, h)),
    mp.Cylinder(r, material=mp.air, height=h)
]

# 1st Brillouin zone of a triangular lattice:
Gamma = mp.Vector3()
M = mp.Vector3(y=0.5)
K = mp.Vector3(1 / −3, 1 / 3)
K_prime = mp.lattice_to_reciprocal(mp.Vector3(x=0.5), geometry_lattice)

only_K = False  # run with only_K=true to only do this k_point
k_interp = 20   # the number of k points to interpolate
if only_K:
    k_points = [K]
else:
    k_points = mp.interpolate(k_interp, [Gamma, K_prime])

```

```
39  #simulation resolution
40  resolution = mp.Vector3(32, 32, 16)
41
42  #number of bands to calculate the dispersion relation for
43  num_bands = 9
44
45
46  #ms gathers all variables defined above and feeds it to mpb.
47  ms = mpb.ModeSolver(
48      geometry_lattice=geometry_lattice,
49      geometry=geometry,
50      resolution=resolution,
51      num_bands=num_bands,
52      k_points=k_points
53  )
54
55  def main():
56      # Run even and odd bands, outputting fields only at the K point:
57      if s == 1.0:
58          # we only have even/odd classification for symmetric structure
59          ms.run_zeven(mpb.output_at_kpoint(K, mpb.output_hfield_z))
60          ms.run_zodd(mpb.output_at_kpoint(K, mpb.output_dfield_z))
61      else:
62          ms.run(mpb.output_at_kpoint(K, mpb.output_hfield_z), mpb.
        display_zparities)
63      ms.display_eigensolver_stats()
64
65  if __name__ == '__main__':
66      main()
```

B   Meep Code for Transmission Simulation

Python code for transmission simulation is offered below. The code includes both two- and three-dimensional simulations. Input can be given in terms of parser arguments to decide for which dimensions to simulate. Parser arguments can also decide if the transmission configuration is to be normal or as a drop-filter configuration.

```
1  import meep as mp
2  import numpy as np
3  from scipy import stats
4  import argparse
5
6  ################# FDTD Designer ##################
7  #################               ##################
8
9  #Lattice Constant, Most decisive variable
10  a = 1 #Everything is normalized to a!
11
12
13  #Parsers
14  parser = argparse.ArgumentParser(description='control meep simulation')
15  parser.add_argument('--res', type=int, default=16, help='resolution of
        simulaton space')
16  parser.add_argument('--fcen', type=float, default=0.260, help='pulse center
        frequency')
```

```python
17  parser.add_argument('-df', type=float, default=0.1, help='pulse frequency
        width')
18  parser.add_argument('-sd', '--struct_decider', type=str, default='ordinary
        ', help='geometric structure to simulate, given as string')
19  parser.add_argument('-dim', '--dimension', type=str, default='2D', help='
        decides whether simulation is 2D or 3D')
20  parser.add_argument('-st', '--simtype', type=str, default='mode', help='
        type of simulation to run, "mode" = resonant mode simulation. "
        transmission" = transmission simulation')
21  parser.add_argument('-twg', '--trans_wg', type=int, default=1, help='sets
        transmission waveguide along desired row')
22  args = parser.parse_args()
23
24  #Constants and Variables
25
26  #Non Parsed
27  dpml = 2*a #thickness of perfectly matched layer
28  hole_r = 3*a/10 #hole radius
29  hole_num = 35 #number of holes added in the x-direction, default 35, 15
        for optimize
30  ring_r = 5*a #radius of ring resonator
31  bufbig = 8*a
32  Si = 0.516*a #should scale to 200nm when a=387.5nm, corresponds to
        midgap_freq:0.25 and source @1550
33  SiO2 = 5.16*a #should scale to 2um when a=387.5nm, corresponds to
        midgap_freq:0.25 and source @1550
34  O2 = 5.16*a ##should scale to 2um when a=387.5nm, corresponds to
        midgap_freq:0.25 and source @1550
35  eps_aSi = 11.8 #permittivity of amorphous silicon
36  eps_SiO2 = 2.085 #permittivity of SiO2 @1550
37
38  #defining computational cell
39  sx = a*hole_num+2*bufbig
40  sy = a*np.sin(3/np.pi)*hole_num+2*bufbig #sin(3/pi) compensating for
        hexagonal structure
41  sz = Si+SiO2+O2+2*bufbig #space should be centered at center Si layer
42
43
44  #Parsed
45  trans_wg = args.trans_wg #sets transmission waveguide along desired row,
        should be given in how any spacing rows desired
46  dimension = args.dimension #sets dimension of simulation
47  simtype = args.simtype #sets simulation type
48
49
50  #this function sets the desired geometric configuration
51  def ordinary():
52      global a #everything should be normalized to the lattice constant a
53      global dpml #thickness of perfectly matched layer
54      global hole_r #hole radius
55      global hole_num #number of holes added in the x-direction
56      global ring_r #radius of ring resonator
57      global bufbig
58      global eps_aSi  #permittivity of amorphous silicon @1550
59      global eps_SiO2 #permittivity of SiO2 @1550
60      global Si #should scale to 200nm when a=387.5nm, corresponds to
        midgap_freq:0.25 and source @1550
```

```python
61          global SiO2 #should scale to 2um when a=387.5nm, corresponds to
            midgap_freq:0.25 and source @1550
62          global O2  ##should scale to 2um when a=387.5nm, corresponds to
            midgap_freq:0.25 and source @1550
63          global simtype
64          global trans_wg
65          #simulation axis
66          global sx
67          global sy #sin(3/pi) compensating for hexagonal structure
68          global sz #space should be centered at center Si layer
69
70          #structure
71          bx = sx-2*bufbig-a
72          by = sy-2*bufbig-a
73          bz_mid = Si
74          bz_low = SiO2
75          bz_high = O2
76          geometry = [mp.Block(size=mp.Vector3(bx, by, bz_mid), center=mp.
            Vector3(), material=mp.Medium(epsilon=eps_aSi))]
77          geometry.append(mp.Block(size=mp.Vector3(bx, by, bz_low), center=mp.
            Vector3(0, 0, -(bz_low+bz_mid)/2), material=mp.Medium(epsilon=eps_SiO2
            )))
78          geometry.append(mp.Block(size=mp.Vector3(bx, by, bz_low), center=mp.
            Vector3(0, 0, (bz_high+bz_mid)/2), material=mp.air))
79          #translation vector
80          if hole_num % 2 == 0:
81              tx = a*hole_num/2 + a/2
82              ty = a*np.sin(3/np.pi)*hole_num/2 + a*np.sin(3/np.pi)/2
83          else:
84              tx = a*(hole_num-1)/2+a/2
85              ty = a*np.sin(3/np.pi)*(hole_num-1)/2
86          #adding holes
87          for iy in range(hole_num):
88            for ix in range(hole_num):
89                if iy % 2 == 0:
90                    geometry.append(mp.Cylinder(material=mp.air, radius=hole_r
            , height=bz_mid, center=mp.Vector3(-tx + a*ix, -ty + iy*a*np.sin(3/np.
            pi), 0)))
91                else:
92                    geometry.append(mp.Cylinder(material=mp.air, radius=hole_r
            , height=bz_mid, center=mp.Vector3(-tx + a*ix + a/2, -ty + iy*a*np.sin
            (3/np.pi), 0)))
93
94          #setting up iteration space for ring resonator
95          range_r = 2*ring_r/a + 1
96          #setting up translation vector for ring resonator
97          if hole_num % 2 == 0: #creates an offset of: a*np.sin(3/np.pi)/2
98              rx = ring_r/2 + a/2
99              ry = ring_r*np.sin(3/np.pi) + a*np.sin(3/np.pi)/2
100         if hole_num % 4 == 0.5 and hole_num % 2 == 0: #due to overlap messup
            between holes
101             rx = rx - a
102         if hole_num % 2 != 0:
103             rx = ring_r/2
104             ry = ring_r*np.sin(3/np.pi)
105         if hole_num % 4 == 0.75 and hole_num % 2 != 0: #due to overlap messup
            between holes
```

```
106        rx = rx + a
107
108     base = ring_r/a + 1
109     #ring resonator
110     for iy in range(int(range_r)):
111         if iy == 0:
112             for ix in range(int(base)):
113                 geometry.append(mp.Cylinder(material=mp.Medium(epsilon=
    eps_aSi), radius=hole_r, height=bz_mid, center=mp.Vector3(-rx+a*ix, -
    ry+a*iy*np.sin(3/np.pi), 0)))
114         elif iy == range_r -1:
115             for ix in range(int(base)):
116                 geometry.append(mp.Cylinder(material=mp.Medium(epsilon=
    eps_aSi), radius=hole_r, height=bz_mid, center=mp.Vector3(-rx+a*ix, -
    ry+a*iy*np.sin(3/np.pi), 0)))
117         elif iy <= ring_r/a and iy != 0:
118             range_temp = base+iy
119             for ix in range(int(range_temp)):
120                 if ix == min(range(int(range_temp))) or ix == max(range(
    int(range_temp))):
121                     geometry.append(mp.Cylinder(material=mp.Medium(epsilon
    =eps_aSi), radius=hole_r, height=bz_mid, center=mp.Vector3(-(rx+a*iy
    /2)+a*ix, -ry+a*iy*np.sin(3/np.pi), 0)))
122         else:
123             range_temp = base+2*(ring_r/a)-iy
124             for ix in range(int(range_temp)):
125                 if ix == min(range(int(range_temp))) or ix == max(range(
    int(range_temp))):
126                     geometry.append(mp.Cylinder(material=mp.Medium(epsilon
    =eps_aSi), radius=hole_r, height=bz_mid, center=mp.Vector3(-(rx+ring_r
    /2)-(ring_r -a*iy)/2+a*ix, -ry+a*iy*np.sin(3/np.pi), 0)))
127
128
129     #Which simulation type is run is parsed from terminal. For
    transmission simulations this if statement becomes active
130     if simtype == 'transmission':
131         sty = -ty+a*np.sin(3/np.pi)*11-a*trans_wg*np.sin(3/np.pi)
132         geometry.append(mp.Block(material=mp.Medium(epsilon=eps_aSi), size
    =mp.Vector3(mp.inf, a*np.sin(3/np.pi), Si), center=mp.Vector3(0, -sty,
     0)))
133
134     #Which simulation type is run is parsed from terminal. For
    transmission simulations with a drop-filter configuration this if
    statement becomes active
135     if simtype == 'drop':
136         sty = -ty+a*np.sin(3/np.pi)*11-a*trans_wg*np.sin(3/np.pi)
137         xdim = sx/2+ring_r
138         geometry.append(mp.Block(material=mp.Medium(epsilon=eps_aSi), size
    =mp.Vector3(xdim, a*np.sin(3/np.pi), Si), center=mp.Vector3(sx/4-a/2,
    -sty, 0)))
139         geometry.append(mp.Block(material=mp.Medium(epsilon=eps_aSi), size
    =mp.Vector3(xdim, a*np.sin(3/np.pi), Si), center=mp.Vector3(-sx/4+a/2,
     sty, 0)))
140
141     return geometry
142
143
```

```
144  #This function sets the geometry for the reference structure (i.e. a
          straight waveguide)
145  def reference():
146      global a #everything should be normalized to the lattice constant a
147      global dpml#thickness of perfectly matched layer
148      global hole_r #hole radius
149      global hole_num #number of holes added in the x-direction
150      global ring_r #radius of ring resonator
151      global bufbig
152      global eps_aSi  #permittivity of amorphous silicon @1550
153      global eps_SiO2 #permittivity of SiO2 @1550
154      global Si #should scale to 200nm when a=387.5nm, corresponds to
          midgap_freq:0.25 and source @1550
155      global SiO2 #should scale to 2um when a=387.5nm, corresponds to
          midgap_freq:0.25 and source @1550
156      global O2  ##should scale to 2um when a=387.5nm, corresponds to
          midgap_freq:0.25 and source @1550
157      global simtype
158      global trans_wg
159      #simulation axis
160      global sx
161      global sy #sin(3/pi) compensating for hexagonal structure
162      global sz #space should be centered at center Si layer
163      #structure
164      bx = sx-2*bufbig-a
165      by = sy-2*bufbig-a
166      bz_mid = Si
167      bz_low = SiO2
168      bz_high = O2
169
170       #translation vector
171      if hole_num % 2 == 0:
172          tx = a*hole_num/2 + a/2
173          ty = a*np.sin(3/np.pi)*hole_num/2 + a*np.sin(3/np.pi)/2
174      else:
175          tx = a*(hole_num-1)/2+a/2
176          ty = a*np.sin(3/np.pi)*(hole_num-1)/2
177
178      sty = -ty+a*np.sin(3/np.pi)*11-a*trans_wg*np.sin(3/np.pi)
179
180      geometry = [mp.Block(size=mp.Vector3(sx, sy, bz_mid), center=mp.
          Vector3(), material=mp.air)] #air around Si wg
181      geometry.append(mp.Block(size=mp.Vector3(sx, a*np.sin(3/np.pi), bz_mid
          ), center=mp.Vector3(0, -sty, 0), material=mp.Medium(epsilon=eps_aSi))
          )
182      geometry.append(mp.Block(size=mp.Vector3(sx, sy, bz_low), center=mp.
          Vector3(0, 0, -(bz_low+bz_mid)/2), material=mp.Medium(epsilon=eps_SiO2
          )))
183      geometry.append(mp.Block(size=mp.Vector3(sx, sy, bz_low), center=mp.
          Vector3(0, 0, (bz_low+bz_mid)/2), material=mp.air))
184
185      return geometry
186
187
188  def main(args):
189      #parameters
190      global a #everything should be normalized to the lattice constant a
```

```python
        res = args.res   #resolution #pixels/um
        fcen = args.fcen   #center frequency
        df = args.df #FWHM
        global dpml   #thickness of perfectly matched layer
        global hole_r   #hole radius
        global hole_num   #number of holes added in the x-direction
        global ring_r   #radius of ring resonator
        global bufbig
        struct_decider = args.struct_decider
        global simtype
        graphics = args.graphics #if yes, graphics of structure will be
         outputted
        global eps_aSi   #permittivity of amorphous silicon
        global Si #should scale to 200nm when a=387.5nm, corresponds to
         midgap_freq:0.25 and source @1550
        global SiO2   #should scale to 2um when a=387.5nm, corresponds to
         midgap_freq:0.25 and source @1550
        global O2   ##should scale to 2um when a=387.5nm, corresponds to
         midgap_freq:0.25 and source @1550
        global trans_wg
        #simulation axis
        global sx
        global sy   #sin(3/pi) compensating for hexagonal structure
        global sz   #space should be centered at center Si layer

        #translation vector
        if hole_num % 2 == 0:
            tx = a*hole_num/2 + a/2
            ty = a*np.sin(3/np.pi)*hole_num/2 + a*np.sin(3/np.pi)/2
        else:
            tx = a*(hole_num-1)/2+a/2
            ty = a*np.sin(3/np.pi)*(hole_num-1)/2

        #simulation space
        cell = mp.Vector3(sx, sy, sz)

        #boundary layers
        boundary = [mp.PML(dpml)]

        #structure is collected from one of the two functions above: ordinary
         or reference
        if struct_decider == 'reference':
            geometries = reference()
        else:
            geometries = ordinary()

        buf = 2*a
        stx = (a*hole_num+2*bufbig)/2 - buf
        sty = -ty+a*np.sin(3/np.pi)*11-a*trans_wg*np.sin(3/np.pi)
        wgw = a*np.sin(3/np.pi)
        #initializing source
        if simtype == 'drop':
            sources = [mp.Source(mp.GaussianSource(fcen, fwidth=df, cutoff=10)
        , component=mp.Ey, center=mp.Vector3(-stx+0.5, sty, 0))]
        else:
            sources = [mp.Source(mp.GaussianSource(fcen, fwidth=df, cutoff=10)
        , component=mp.Ey, center=mp.Vector3(-stx+0.5, -sty, 0))]
```

```
241
242     if dimension == '3D':
243         #symmetries
244         symmetries = [mp.Mirror(mp.Z, phase=+1)]  #NB: only mirror
        symmetry in Z if SiO2 is substituted with O2!!
245
246         #sim gathers all variables defined above and feeds it to Meep.
247         sim = mp.Simulation(resolution=res, cell_size=cell,
        boundary_layers=boundary, geometry=geometries, dimensions=3, sources=
        sources, symmetries=symmetries) #, symmetries=symmetries
248
249         #flux region is defined
250         freg = mp.FluxRegion(center=mp.Vector3(stx-0.5, -sty, 0), size=mp.
        Vector3(0, wgw, 0), direction=mp.X)
251         nfreq = 100000 # number of frequencies at which to compute flux
252
253         #transmitted flux
254         fcen_flux = 0.325
255         df_flux = 0.15
256         trans = sim.add_flux(fcen_flux, df_flux, nfreq, freg)
257
258         ####################                    ########################
259         ################## FDTD Designer ########################
260
261         ################## FDTD Simulator ########################
262         ####################                    ########################
263
264         #simulation is initiated by run statement
265         sim.run(mp.at_beginning(mp.output_epsilon), until_after_sources=mp
        .stop_when_fields_decayed(50, mp.Ey, mp.Vector3(stx-0.5, -sty, 0), 1e
        -7))
266
267         ####################                    ########################
268         ################## FDTD Simulator ########################
269
270         ################## FDTD Analyzer ########################
271         ####################                    ########################
272
273         #print out the flux spectrum
274         sim.display_fluxes(trans)
275
276         ####################                    ########################
277         ################## FDTD Analyzer ########################
278
279     else:
280         #sim gathers all variables defined above and feeds it to Meep.
281         sim = mp.Simulation(resolution=res, cell_size=cell,
        boundary_layers=boundary, geometry=geometries, dimensions=2, sources=
        sources) #, symmetries=symmetries
282
283         #flux region is defined
284         freg = mp.FluxRegion(center=mp.Vector3(stx-0.5, -sty, 0), size=mp.
        Vector3(0, wgw, 0))
285         nfreq = 100000 # number of frequencies at which to compute flux
286
287         #transmitted flux
288         trans = sim.add_flux(fcen, df, nfreq, freg)
```

```
289
290          ####################                   #######################
291          ################### FDTD Designer #######################
292
293          ################### FDTD Simulator #######################
294          ####################                   #######################
295
296          #simulation is initiated by run statement
297          sim.run(mp.at_beginning(mp.output_epsilon), until_after_sources=mp
          .stop_when_fields_decayed(50, mp.Ey, mp.Vector3(stx−0.5, −sty, 0), 1e
          −7))
298
299          ####################                   #######################
300          ################### FDTD Simulator #######################
301
302          ################### FDTD Analyzer #######################
303          ####################                   #######################
304
305          #print out the flux spectrum
306          sim.display_fluxes(trans)
307
308          ####################                   #######################
309          ################### FDTD Analyzer #######################
310
311   if __name__ == '__main__':
312       main(args)
```

C Meep Code for Mode Simulation

Python code for mode simulation is offered below. The code includes both two- and three-dimensional simulations. Input can be given in terms of parser arguments to decide for which dimensions to simulate.

```
1   import meep as mp
2   import numpy as np
3   from scipy import stats
4   import argparse
5
6   ################ FDTD Designer #############
7   #################                   #############
8
9   #Lattice Constant, Most decisive variable
10  a = 1 #Everything is normalized to a!
11
12
13  #Parsers
14  parser = argparse.ArgumentParser(description='control meep simulation')
15  parser.add_argument('−res', type=int, default=16, help='resolution of
        simulaton space')
16  parser.add_argument('−fcen', type=float, default=0.260, help='pulse center
         frequency')
17  parser.add_argument('−df', type=float, default=0.1, help='pulse frequency
        width')
18  parser.add_argument('−sd', '−−struct_decider', type=str, default='ordinary
        ', help='geometric structure to simulate, given as string')
```

```
19  parser.add_argument('-dim', '--dimension', type=str, default='2D', help='
        decides whether simulation is 2D or 3D')
20  parser.add_argument('-st', '--simtype', type=str, default='mode', help='
        type of simulation to run, "mode" = resonant mode simulation. "
        transmission" = transmission simulation')
21  parser.add_argument('-twg', '--trans_wg', type=int, default=1, help='sets
        transmission waveguide along desired row')
22  args = parser.parse_args()
23
24  #Constants and Variables
25
26  #Non Parsed
27  dpml = 2*a #thickness of perfectly matched layer
28  hole_r = 3*a/10 #hole radius
29  hole_num = 35 #number of holes added in the x-direction, default 35, 15
        for optimize
30  ring_r = 5*a #radius of ring resonator
31  bufbig = 8*a
32  Si = 0.516*a #should scale to 200nm when a=387.5nm, corresponds to
        midgap_freq:0.25 and source @1550
33  SiO2 = 5.16*a #should scale to 2um when a=387.5nm, corresponds to
        midgap_freq:0.25 and source @1550
34  O2 = 5.16*a ##should scale to 2um when a=387.5nm, corresponds to
        midgap_freq:0.25 and source @1550
35  eps_aSi = 11.8 #permittivity of amorphous silicon
36  eps_SiO2 = 2.085 #permittivity of SiO2 @1550
37
38  #defining computational cell
39  sx = a*hole_num+2*bufbig
40  sy = a*np.sin(3/np.pi)*hole_num+2*bufbig #sin(3/pi) compensating for
        hexagonal structure
41  sz = Si+SiO2+O2+2*bufbig #space should be centered at center Si layer
42
43
44  #Parsed
45  trans_wg = args.trans_wg #sets transmission waveguide along desired row,
        should be given in how any spacing rows desired
46  dimension = args.dimension #sets dimension of simulation
47  simtype = args.simtype #sets simulation type
48
49
50  #this function sets the desired geometric configuration
51  def ordinary():
52      global a #everything should be normalized to the lattice constant a
53      global dpml #thickness of perfectly matched layer
54      global hole_r #hole radius
55      global hole_num #number of holes added in the x-direction
56      global ring_r #radius of ring resonator
57      global bufbig
58      global eps_aSi  #permittivity of amorphous silicon @1550
59      global eps_SiO2 #permittivity of SiO2 @1550
60      global Si #should scale to 200nm when a=387.5nm, corresponds to
        midgap_freq:0.25 and source @1550
61      global SiO2 #should scale to 2um when a=387.5nm, corresponds to
        midgap_freq:0.25 and source @1550
62      global O2  ##should scale to 2um when a=387.5nm, corresponds to
        midgap_freq:0.25 and source @1550
```

```python
63        global simtype
64        global trans_wg
65        #simulation axis
66        global sx
67        global sy #sin(3/pi) compensating for hexagonal structure
68        global sz #space should be centered at center Si layer
69
70        #structure
71        bx = sx-2*bufbig-a
72        by = sy-2*bufbig-a
73        bz_mid = Si
74        bz_low = SiO2
75        bz_high = O2
76        geometry = [mp.Block(size=mp.Vector3(bx, by, bz_mid), center=mp.
          Vector3(), material=mp.Medium(epsilon=eps_aSi))]
77        geometry.append(mp.Block(size=mp.Vector3(bx, by, bz_low), center=mp.
          Vector3(0, 0, -(bz_low+bz_mid)/2), material=mp.Medium(epsilon=eps_SiO2
          )))
78        geometry.append(mp.Block(size=mp.Vector3(bx, by, bz_low), center=mp.
          Vector3(0, 0, (bz_high+bz_mid)/2), material=mp.air))
79        #translation vector
80        if hole_num % 2 == 0:
81            tx = a*hole_num/2 + a/2
82            ty = a*np.sin(3/np.pi)*hole_num/2 + a*np.sin(3/np.pi)/2
83        else:
84            tx = a*(hole_num-1)/2+a/2
85            ty = a*np.sin(3/np.pi)*(hole_num-1)/2
86        #adding holes
87        for iy in range(hole_num):
88            for ix in range(hole_num):
89                if iy % 2 == 0:
90                    geometry.append(mp.Cylinder(material=mp.air, radius=hole_r
          , height=bz_mid, center=mp.Vector3(-tx + a*ix, -ty + iy*a*np.sin(3/np.
          pi), 0)))
91                else:
92                    geometry.append(mp.Cylinder(material=mp.air, radius=hole_r
          , height=bz_mid, center=mp.Vector3(-tx + a*ix + a/2, -ty + iy*a*np.sin
          (3/np.pi), 0)))
93
94        #setting up iteration space for ring resonator
95        range_r = 2*ring_r/a + 1
96        #setting up translation vector for ring resonator
97        if hole_num % 2 == 0: #creates an offset of: a*np.sin(3/np.pi)/2
98            rx = ring_r/2 + a/2
99            ry = ring_r*np.sin(3/np.pi) + a*np.sin(3/np.pi)/2
100       if hole_num % 4 == 0.5 and hole_num % 2 == 0: #due to overlap messup
          between holes
101           rx = rx - a
102       if hole_num % 2 != 0:
103           rx = ring_r/2
104           ry = ring_r*np.sin(3/np.pi)
105       if hole_num % 4 == 0.75 and hole_num % 2 != 0: #due to overlap messup
          between holes
106           rx = rx + a
107
108       base = ring_r/a + 1
109       #ring resonator
```

```python
110        for iy in range(int(range_r)):
111            if iy == 0:
112                for ix in range(int(base)):
113                    geometry.append(mp.Cylinder(material=mp.Medium(epsilon=
       eps_aSi), radius=hole_r, height=bz_mid, center=mp.Vector3(-rx+a*ix, -
       ry+a*iy*np.sin(3/np.pi), 0)))
114            elif iy == range_r-1:
115                for ix in range(int(base)):
116                    geometry.append(mp.Cylinder(material=mp.Medium(epsilon=
       eps_aSi), radius=hole_r, height=bz_mid, center=mp.Vector3(-rx+a*ix, -
       ry+a*iy*np.sin(3/np.pi), 0)))
117            elif iy <= ring_r/a and iy != 0:
118                range_temp = base+iy
119                for ix in range(int(range_temp)):
120                    if ix == min(range(int(range_temp))) or ix == max(range(
       int(range_temp))):
121                        geometry.append(mp.Cylinder(material=mp.Medium(epsilon
       =eps_aSi), radius=hole_r, height=bz_mid, center=mp.Vector3(-(rx+a*iy
       /2)+a*ix, -ry+a*iy*np.sin(3/np.pi), 0)))
122            else:
123                range_temp = base+2*(ring_r/a)-iy
124                for ix in range(int(range_temp)):
125                    if ix == min(range(int(range_temp))) or ix == max(range(
       int(range_temp))):
126                        geometry.append(mp.Cylinder(material=mp.Medium(epsilon
       =eps_aSi), radius=hole_r, height=bz_mid, center=mp.Vector3(-(rx+ring_r
       /2)-(ring_r-a*iy)/2+a*ix, -ry+a*iy*np.sin(3/np.pi), 0)))
127
128
129    return geometry
130
131
132 def main(args):
133    #parameters
134    global a #everything should be normalized to the lattice constant a
135    res = args.res   #resolution #pixels/um
136    fcen = args.fcen  #center frequency
137    df = args.df #FWHM
138    global dpml  #thickness of perfectly matched layer
139    global hole_r  #hole radius
140    global hole_num  #number of holes added in the x-direction
141    global ring_r  #radius of ring resonator
142    global bufbig
143    struct_decider = args.struct_decider
144    global simtype
145    graphics = args.graphics #if yes, graphics of structure will be
       outputted
146    global eps_aSi  #permittivity of amorphous silicon
147    global Si #should scale to 200nm when a=387.5nm, corresponds to
       midgap_freq:0.25 and source @1550
148    global SiO2  #should scale to 2um when a=387.5nm, corresponds to
       midgap_freq:0.25 and source @1550
149    global O2  ##should scale to 2um when a=387.5nm, corresponds to
       midgap_freq:0.25 and source @1550
150    global trans_wg
151    #simulation axis
152    global sx
```

```python
153      global sy  #sin(3/pi) compensating for hexagonal structure
154      global sz  #space should be centered at center Si layer
155
156      #translation vector
157      if hole_num % 2 == 0:
158          tx = a*hole_num/2 + a/2
159          ty = a*np.sin(3/np.pi)*hole_num/2 + a*np.sin(3/np.pi)/2
160      else:
161          tx = a*(hole_num-1)/2+a/2
162          ty = a*np.sin(3/np.pi)*(hole_num-1)/2
163
164      #simulation space
165      cell = mp.Vector3(sx, sy, sz)
166
167      #boundary layers
168      boundary = [mp.PML(dpml)]
169
170      #structure is collected from one of the two functions above: ordinary
         or reference
171      geometries = ordinary()
172
173
174      if simtype == 'mode':
175          if dimension == '3D':
176              #initializing source
177              sources = [mp.Source(mp.GaussianSource(fcen, fwidth=df),
         component=mp.Hz, center=mp.Vector3(-ring_r, 0, 0))]
178
179              #symmetries (reduces computational time)
180              symmetries = [mp.Mirror(mp.Y, phase=-1)] #NB: only mirror
         symmetry in Z if SiO2 is substituted with O2!!, mp.Mirror(mp.Z, phase
         =+1)   , mp.Mirror(mp.Z, phase=1)
181
182              #simulation
183              sim = mp.Simulation(resolution=res, cell_size=cell,
         boundary_layers=boundary, geometry=geometries, dimensions=3, sources=
         sources, symmetries=symmetries)
184
185              #####################              ##################
186              ##################### FDTD Designer ##################
187              ##################### FDTD Simulator and Analyzer
         #################
188              #####################
         #################
189
190              #simulation is initiated by run statement
191              sim.run(mp.after_sources(mp.Harminv(mp.Hz, mp.Vector3(ring_r,
         0, 0), fcen, df)), until_after_sources=5000)
192
193
194              #####################
         #################
195              ##################### FDTD Simulator and Analyzer
         #################
196          else:
197              #initializing source
```

```
198            sources = [mp.Source(mp.GaussianSource(fcen, fwidth=df),
       component=mp.Hz, center=mp.Vector3(-ring_r, 0, 0))]
199
200            #symmetries (reduces computational time)
201            symmetries = [mp.Mirror(mp.Y, phase=-1)]
202
203            #simulation
204            sim = mp.Simulation(resolution=res, cell_size=cell,
       boundary_layers=boundary, geometry=geometries, dimensions=2, sources=
       sources, symmetries=symmetries)
205
206            #####################           ##################
207            #################### FDTD Designer ##################
208            #################### FDTD Simulator and Analyzer
       #################
209            #####################
       #################
210
211            #simulation is initiated by run statement
212            sim.run(mp.after_sources(mp.Harminv(mp.Hz, mp.Vector3(ring_r,
       0, 0), fcen, df)), until_after_sources=5500)
213
214            #####################
       #################
215            #################### FDTD Simulator and Analyzer
       #################
216
217 if __name__ == '__main__':
218     main(args)
```

D Design Structures
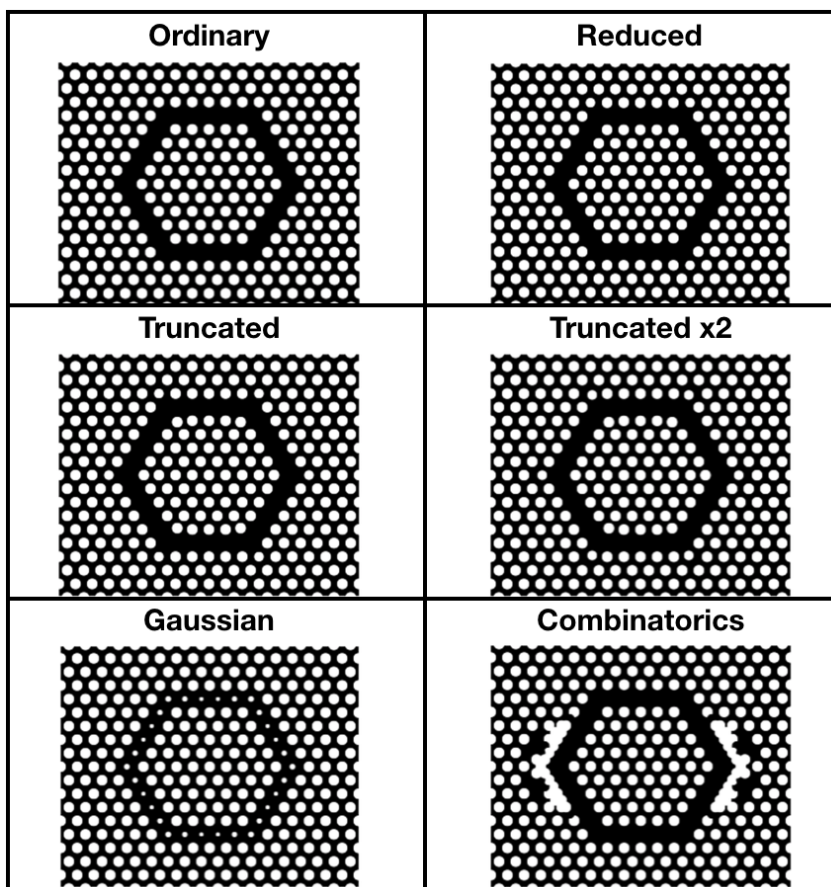
Figure 6.1: Two-dimensional illustration of the different ring resonator designs.

E Transmission Plots

E.1 2D

Transmission plots for two-dimensional structures.
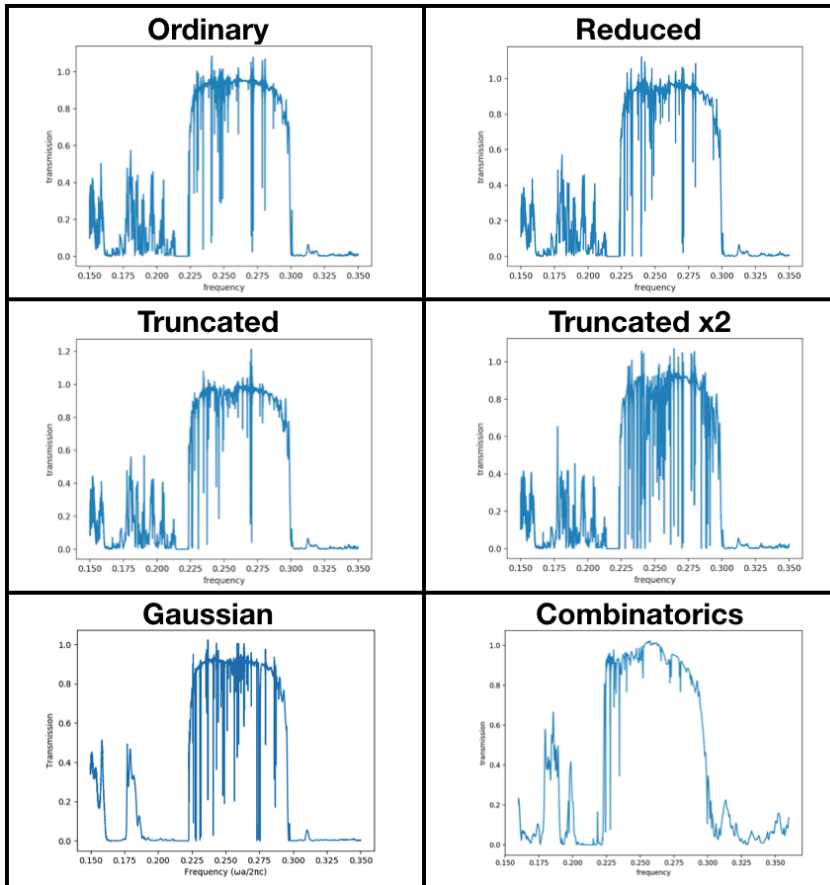
Figure 6.2: Transmission plots for two-dimensional design solutions. The frequency is normalized with respect to the lattice constant a and speed of light c ($\omega a/2\pi c$).

E.2   3D

Transmission plots for three-dimensional structures. The substrate is simulated as air for all design solutions.
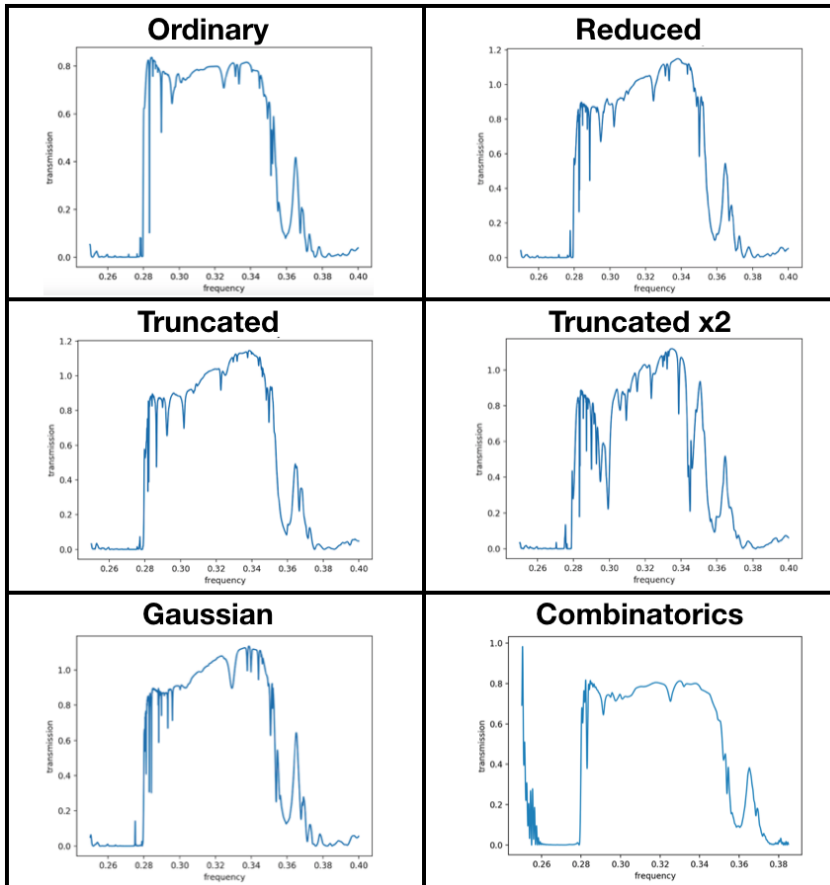
Figure 6.3: Transmission plots for three-dimensional design solutions. The frequency is normalized with respect to the lattice constant a and speed of light c ($\omega a/2\pi c$).

F   Mode Results

Table 6.1 contains all achieved Q-factor values for two-dimensional, three-dimensional with air simulated substrate (denoted 3Ds), and three dimensional with silica simulated substrate simulations.

Design Solution	2D Q-factor	3Ds Q-factor	3D Q-factor
Ordinary	4.8×10^8	17997	3213
Reduced	5.7×10^8	48189	3299
Truncated	8.9×10^7	59871	3787
Truncated x2	8.1×10^7	1729	2390
Gaussian	1.1×10^8	31316	4286
Combinatorics	2.0×10^8	6393	599

Table 6.1: All achieved Q-factors.

G Fabrication Images

SEM-images from fabrication are offered here as a supplement to the images offered in results.

G.1 Etching

Figure 6.4 is a macroscopic view of the images presented in Figure 5.18 in Chapter 5.
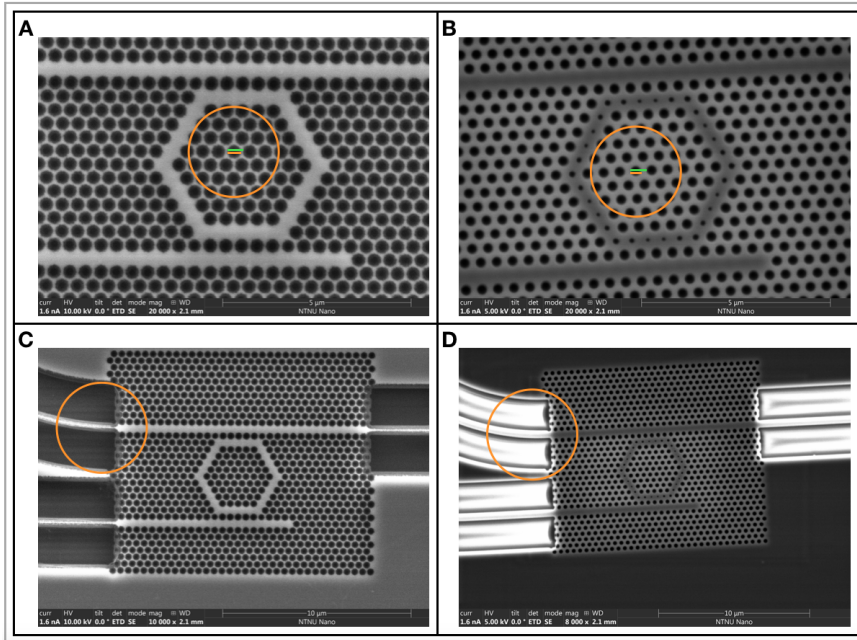
Figure 6.4: Caption

Figure 5.18 illustrates four SEM-images of two different samples. Figures A and C represent a sample etched for 77 s. Figures B and D represent a sample etched for 47 seconds. Yellow circles represent points of interest. The yellow and green lines captures hole diameter and lattice constant, respectively. The green line in Figures A and B are both approximately 420 nm. The yellow line in Figures A and B are approximately 335 and 250 nm, respectively. With the measured diameters and lattice constants an etch duration of 77 s has produced an air-hole radius of 0.40a. Air-hole radius of 0.30a is the result of an etch duration of 47 s.

H Tunable Laser Datasheet

Figure 6.5 illustrates the TLK-L1550M lasers power spectrum.
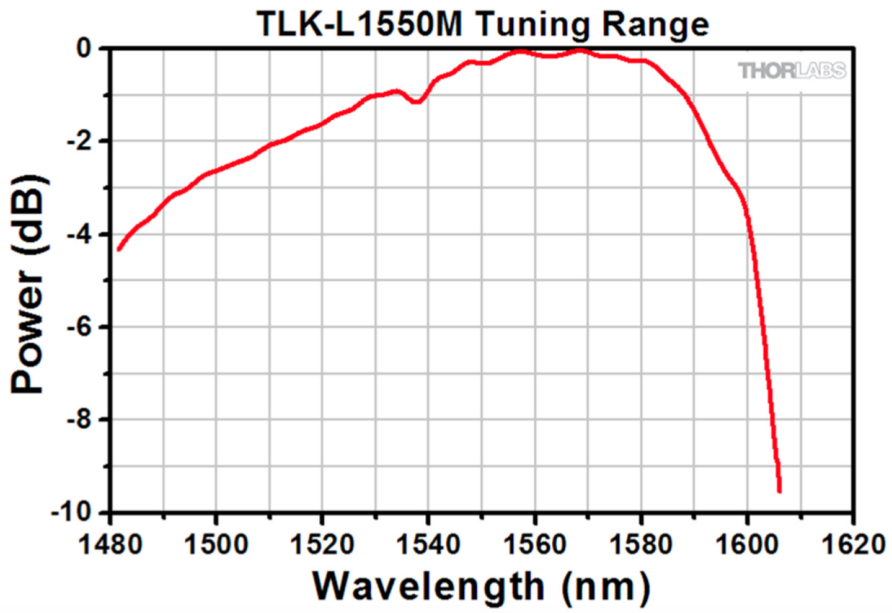
Figure 6.5: Power spectrum of the TLK-L1550M from Thor Labs.

I Transmission Measurements

Figure 6.6 illustrate the measured transmission for design solutions ordinary, reduced, and truncated over the wavelength range 1500-1550 nm.
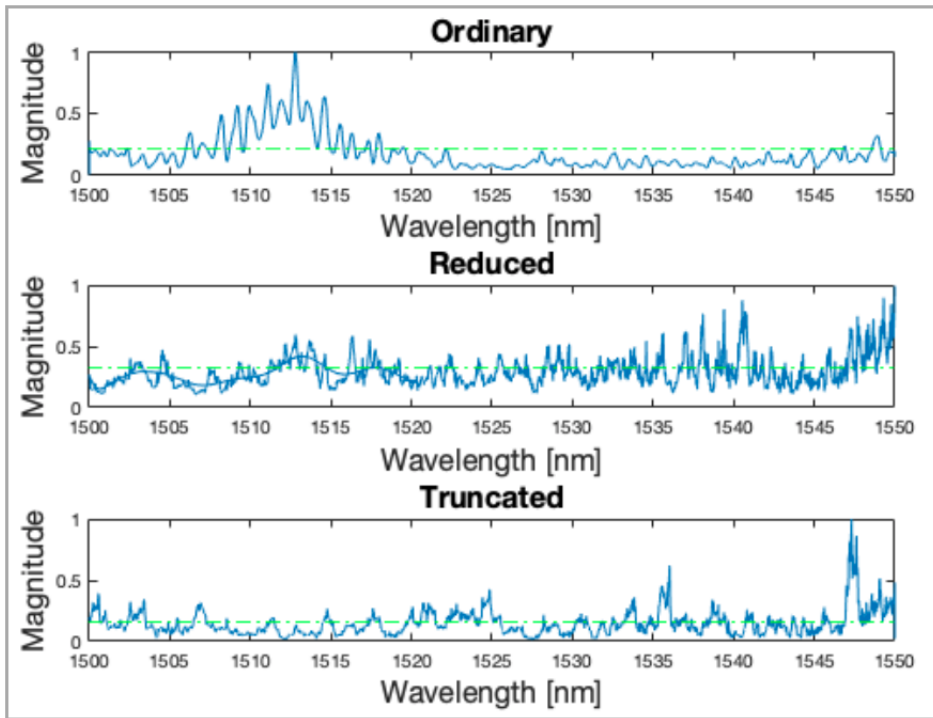
Figure 6.6: Transmission measurements for PCRR designs ordinary, reduced, and truncated over the wavelength range 1500-1550 nm. The green dashed line indicates the mean spectral value. All designs are produced in c-Si layer. Spectra are normalized to unity.

Figure 6.7 illustrate the measured transmission for design solutions truncated x2, gaussian, and combinatorics over the wavelength range 1500-1550 nm.
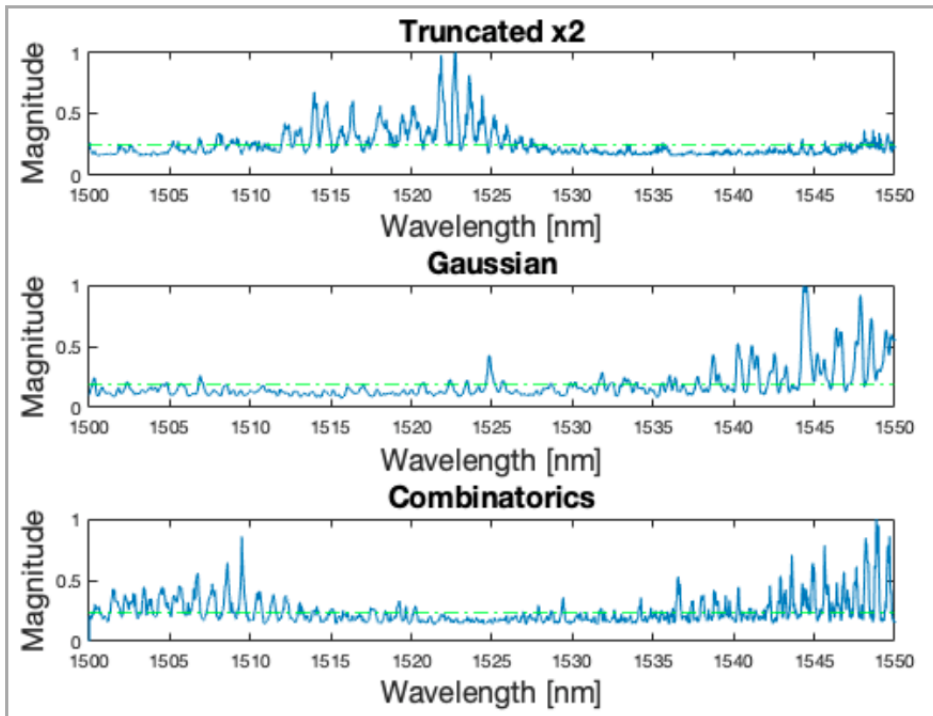
Figure 6.7: Transmission measurements for PCRR designs truncated x2, gaussian, and combinatorics over the wavelength range 1500-1550 nm. The green dashed line indicates the mean spectral value. All designs are produced in c-Si layer. Spectra are normalized to unity.